Technische Universität München
TUM School of Natural Sciences

# A multi-qubit quantum network node assembled with optical tweezers in an optical cavity

Lukas Julian Hartung

Vollständiger Abdruck der von der TUM School of Natural Sciences der Technischen Universität München zur Erlangung eines

**Doktors der Naturwissenschaften (Dr. rer. nat)**

genehmigten Dissertation.

Vorsitz:                Prof. Dr. Nora Brambilla

Prüfende der Dissertation:

       1. Hon.-Prof. Dr. Gerhard Rempe
       2. Prof. Dr. Stefan Filipp

Die Dissertation wurde am 04.11.2024 bei der Technischen Universität München eingereicht und durch die TUM School of Natural Sciences am 11.12.2024 angenommen.

# Abstract

This thesis reports on the implementation of a multi-qubit network register consisting of rubidium atoms trapped at the center of an optical cavity. It is based on the combination of a single atom addressing and positioning system, which was built in the course of this thesis, with the previously existing setup. The new system enables the generation of optical tweezers to trap and position atoms and to address individual atoms to generate atom-photon entanglement. In this thesis, the tweezers are used to create atomic arrays of up to six atoms in one and two dimensions. This tweezer-based preparation of atomic arrays increases the array preparation efficiency by orders of magnitude compared to the previously used probabilistic atom preparation method. Using the individual atom addressing, the atoms are then sequentially addressed to generate entangled atom-photon pairs. By using a multiplexing protocol, we increase the entanglement generation-to-detection efficiency to $\sim 90\,\%$ and to an in-fiber efficiency of $97.4(6)\,\%$.

# List of Publications

- A quantum-logic gate between distant quantum-network modules.
  S. Daiss*, S. Langenfeld*, S. Welte, E. Distante, P. Thomas, L. Hartung, O. Morin, and G. Rempe
  *Science* **371**, 614-617 (2021).

- Quantum Teleportation between Remote Qubit Memories with Only a Single Photon as a Resource.
  S. Langenfeld*, S. Welte*, L. Hartung, S. Daiss, P. Thomas, O. Morin, E. Distante, and G. Rempe
  *Physical Review Letters* **126**, 130502 (2021)

- Detecting an itinerant optical photon twice without destroying it.
  E. Distante, S. Daiss, S. Langenfeld, L. Hartung, P. Thomas, O. Morin, G. Rempe, and S. Welte
  *Physical Review Letters* **126**, 253603 (2021).

- A nondestructive Bell-state measurement on two distant atomic qubits.
  S. Welte, P. Thomas, L. Hartung, S. Daiss, S. Langenfeld, O. Morin, G. Rempe and E. Distante
  *Nature Photonics* **15**, 504-509 (2021).

- A quantum-network register assembled with optical tweezers in an optical cavity.
  L. Hartung, M. Seubert, S. Welte, E. Distante, and G. Rempe
  *Science* **385** 179-183 (2024)

# Contents

# Introduction

It was suggested for the first time by Manin in 1980 [1] and Feynman in 1982 [2] that quantum mechanical systems and specific quantum algorithms could be simulated more efficiently on a quantum computer than on classical computers. This suggestion led to the development of the first quantum algorithms in the following years, e.g., the Deutsch-Jozsa algorithm [3], Shor's algorithm [4], and Grover's algorithm [5]. At the same time, experimental groups started to investigate the first quantum mechanical systems that could be used as potential platforms for the physical implementation of quantum computers. As a result, the first elementary quantum algorithms [6, 7] and controlled NOT gates (CNOT) [8–10], which form together with single-qubit operations a set of universal quantum logic gates for quantum computing [11, 12], were demonstrated.

However, as for classical computers, error correction [13–19] is required for quantum algorithms to be executed reliably on quantum computers. All quantum algorithms are composed of elementary operations and each of these elementary operations has a specific error probability. If the error probabilities of the individual operations are too high, error correction is not possible. However, if the error probabilities are below a certain threshold, the errors can be corrected using error correction protocols. Error correction is based on the idea to encode the quantum information of one logical qubit over many physical qubits, rendering the information highly redundant. As a result, in practice, robust, fault-tolerant quantum computers will need thousands or millions of qubits [19, 20], which poses a big experimental challenge. Even though first quantum error correction protocols have already been shown on different platforms [21–28], the realization of a physical system with a sufficient number of qubits for fault-tolerant quantum computing in a useful scenario has still to be implemented.

One way to circumvent this big experimental challenge - the implementation of a single fault-tolerant quantum computer with a very large number of qubits - is distributed quantum computing [29–31], where the quantum computer is integrated into a quantum network [32, 33]. In this case, each network node represents a computing module and contains a large register of stationary qubits for storing and processing quantum information. The individual computing modules are connected via quantum channels. This allows the modules to interact via the exchange of photonic qubits. In such a distributed quantum computer, the different computing modules then perform quantum computations together and make up the entire quantum computer. Such networks would not only allow for distributed quantum

computing, but also potentially allow different quantum network applications, such as clock synchronization [34, 35], secure communication [36] and precision sensing [37]. First small, elementary quantum networks consisting of two or three nodes [38–43] as well as elementary quantum gates between different modules have already been experimentally demonstrated [44, 45].

The basis for most of the quantum networking applications is the efficient generation and distribution of entanglement between network nodes. Experimentally, entanglement between light and matter [46, 47], as well as between matter qubits [41, 42, 48–50] has already been demonstrated over large distances. In a typical protocol for entanglement distribution between matter qubits, one first entangles the stationary qubits of the register at a network node with the optical photons. These entangled photons are then sent across the network and used to create entanglement between stationary qubits at the different network nodes. However, the efficient generation of entanglement between photons and matter qubits requires that the matter qubits are placed in a high-finesse cavity. Therefore, much effort has been put in the past years into coupling different quantum mechanical emitters to an optical resonator. As a result of this effort, entanglement generation between stationary qubits in optical resonators and photons has already been demonstrated for different experimental platforms, such as ions [46, 51, 52], neutral atoms [53], Rydberg superatoms [54], semiconductor spins [55, 56], rare-earth ions [57], and SiV in diamond [58]. However, the number of qubits in these registers was limited to a maximum of three. The implementation of large network registers in an optical resonator is still an outstanding challenge.

In parallel to the developments in the fields of quantum computing and quantum information processing, atom trapping techniques based on optical tweezers have been developed. Optical tweezers are highly focused laser beams that are used to capture, move, and precisely position tiny, micrometer-sized objects [59–61]. For the first time, a single atom was trapped in optical tweezers by the group of Philippe Grangier [62] in 2001. It became soon obvious that this method of trapping neutral atoms has big potential in the fields of quantum computing and quantum networks, as it allows for the creation of defect-free atomic arrays. Already in 2016, three different experimental groups successfully created arrays of tens of atoms, which were arranged in arbitrary one- and two-dimensional configurations [63–65]. To prepare these arrays, atoms were stochastically loaded from a magneto-optical trap into arrays of optical tweezers and subsequently rearranged within the tweezers until the desired defect-free configuration was realized. Ever since these first experiments, the number of atoms in such tweezer arrays has been dramatically increased, and arrays of more than hundreds [66, 67] or even thousands of atoms have been created[68].

These results suggest that optical tweezers combined with resonators could be used to create quantum network nodes consisting of large atomic arrays. In that case, the individual atoms could be efficiently entangled with photons and subsequently entangled to different network nodes. The main experimental challenges in combining optical tweezers with optical resonators are the limited optical access due to the

mirrors of the optical resonator and the realization of a high cooperativity for each individual atom. Several groups have already managed to merge optical tweezers and optical resonators and created arrays of about ten atoms [69–71], but they have not yet proven the control over the individual atoms. However, the control over individual atoms is mandatory for the envisioned applications in quantum networks [72]. In the present work, we demonstrate this missing feature: We create one- and two-dimensional atomic arrays at the center of a resonator and control the individual atomic qubits with a single atom addressing and positioning system, which was built during this thesis. We demonstrate the control over the individual atoms by entangling the individual atoms of the array with optical photons generated in a vacuum-stimulated Raman adiabatic passage (vSTIRAP). Using a multiplexing scheme, we increase the generation-to-detection efficiency of the atom-photon entanglement generation process to about 90 % and to more than 97 % in fiber. These values suggest that we approach the deterministic generation of atom-photon entanglement, which would allow to overcome the fundamental limits on communication rates in quantum networks which are given by intrinsic optical losses and the length of the communication channels [73].

**The thesis is structured as follows:** In Chapter 1, I describe the experimental setup and the basic experimental techniques that were required in the course of the thesis. Chapter 2 describes the single-atom addressing system and how it can be used to load atomic arrays. Finally, in Chapter 3, I will discuss the individual control over the qubits of the atomic arrays by generating atom-photon entanglement and the scalability of our system.

# Chapter 1

# A single quantum network node

## 1.1 Vacuum chamber and cavity system

This section gives a brief summary of the experimental setup. A more detailed description of the setup can be found in previously published PhD theses [74–77]. The core of the experimental setup is the optical cavity within vacuum chamber. It is shown in Fig. 1.1. The $^{87}$Rb dispenser is indicated by the circled white A. The dispenser provides the $^{87}$Rb that we use for the experiment. It is controlled by an external current which heats up the dispenser. This leads to the evaporation and the release of $^{87}$Rb into the vacuum chamber. The dispenser is constantly kept on during the operation of the experiment and floods the chamber with rubidium to ensure a sufficiently high $^{87}$Rb background pressure for reliable atom preparation. The rubidium atoms are then initially trapped and cooled with a magneto-optical trap, which is located at a distance of 14 mm from the cavity center. After the MOT-phase, the atoms are transferred with a running wave dipole trap (transfer trap) to the cavity center and transferred in a two-dimensional optical lattice (see section 2.3). The cavity (zoomed in, top right, represented by the orange cone) consists of two mirrors with transmissivities of $T$=3(1) ppm and $T$=92(3) ppm. As one of the mirrors has a higher transmissivity, photons within the cavity predominantly exit the cavity through the mirror with the higher transmission, referred to as outcoupling mirror. The light-matter interaction in a cavity is characterized by three important rates, namely the cavity field decay rate $\kappa$, the atomic polarization decay rate $\gamma$ and the light-matter coupling strength $g$. The total field decay rate $\kappa$ is the sum of the decay rate through the outcoupling mirror $\kappa_{out} = 2\pi \times 2.3$ MHz and the decay rate due to round-trip losses or photons leaving the cavity through the low transmissivity one $\kappa_{loss} = 2\pi \times 0.2$ MHz, i.e., $\kappa = \kappa_{out} + \kappa_{loss} = 2\pi \times 2.5$ MHz. $\gamma = 2\pi \times 3$ MHz is the atomic polarization decay rate. The atom-cavity coupling rate is given by $g$, which is as $g = \sqrt{\frac{d^2\omega}{2\epsilon_0 \hbar V}}$, where $d$ is the transition dipole matrix element of the relevant transition, $\omega$ is the corresponding transition frequency, $\epsilon_0$ is the vacuum permittivity and $V$ is the cavity mode volume The radius of curvature of the mirrors is 50 mm, giving a waist of $w_0 = 29$ μm ($1/e^2$ radius of the intensity) for the fundamental TEM00 mode. For this mode, the Rayleigh range is $z_R = 3.386$ mm. As the distance of the mirrors $L$ is 485(1) μm, which is negligibly small compared to the Rayleigh range, the waist can be assumed to be constant

over the entire length of the cavity. Using this assumption, the mode volume of the electric field mode can be calculated as $V = \pi w_0^2/4L = 3.203 \times 10^{-13}\,\mathrm{m}^3$. This gives a theoretical maximum atom-cavity coupling of $g = 2\pi \times 8.1\,\mathrm{MHz}$ for the $|5^2S_{1/2}, F{=}2, m_F{=}2\rangle \to |5^2P_{3/2}, F{=}3, m_F{=}3\rangle$ transition and a maximum value of $g = 2\pi \times 5.2\,\mathrm{MHz}$ for the $|5^2S_{1/2}, F{=}1, m_F{=}-1\rangle \to |5^2P_{3/2}, F{=}1, m_F{=}0\rangle$ transition. For the transition $|5^2S_{1/2}, F{=}2, m_F{=}2\rangle \to |5^2P_{3/2}, F{=}3, m_F{=}3\rangle$ transition, we measure a coupling constant of $g = 2\pi \times 7.8(2)\,\mathrm{MHz}$, which is only approximately $4\,\%$ below the theoretical maximum. The slightly lower value can be partially explained by the spatial distribution of the atomic wave function[1], which leads to an averaging of the $g$ value. For the atom-photon entanglement generation, we measure a value of $2\pi \times 4.9(7)\,\mathrm{MHz}$ (see section 1.6). The three rates $\kappa, \gamma$ and $g$ can be combined in a single expression, the cooperativity $C := \frac{g^2}{2\kappa\gamma}$. If the dominating rate is the light-matter coupling strength, i.e., $g > (\kappa, \gamma)$, the system is in the so-called strong coupling regime. In this regime, a normal mode splitting can be observed [78]. Additionally, a high cooperativity $C$ is advantageous for many applications in quantum information processing, e.g., the efficient atom-photon entanglement generation (see section 3.1.3) or the implementation of a controlled phase gate [79]. The cavity is mounted in a length-tunable piezo tube, which is used to actively stabilize the cavity length using a PID locking scheme. The same light that we use to stabilize the cavity length is used as a blue-detuned intracavity trap. Depending on the used cavity configuration (see section 1.3), the wavelength of the intracavity trap is either $388.869\,593\,\mathrm{THz}$ (emission) or $388.863\,250\,\mathrm{THz}$ (gate). The wavelength of the intracavity trap is chosen such that the atoms are positioned at a position of maximum coupling at the center of the cavity (see Fig. 3.12). The free spectral range $\Delta_{FSR}$ can be determined using the length $L$ of the cavity and the speed of light $c$ by $\Delta_{FSR} = \frac{c}{2L} = 309\,\mathrm{GHz}$ at $780\,\mathrm{nm}$, giving a finesse of $\mathcal{F} = 61\,000(2000)$. The most important cavity parameters and rates are summarized in Table 1.1. The cavity holder is designed to ensure optical access from all sides. A summary of the beam configuration is given in section 1.3.

---

[1]for the motional ground state, the standard deviation of the atomic position is $20\,\mathrm{nm} \leq \sigma_x \leq 25\,\mathrm{nm}$, depending on the trap frequency
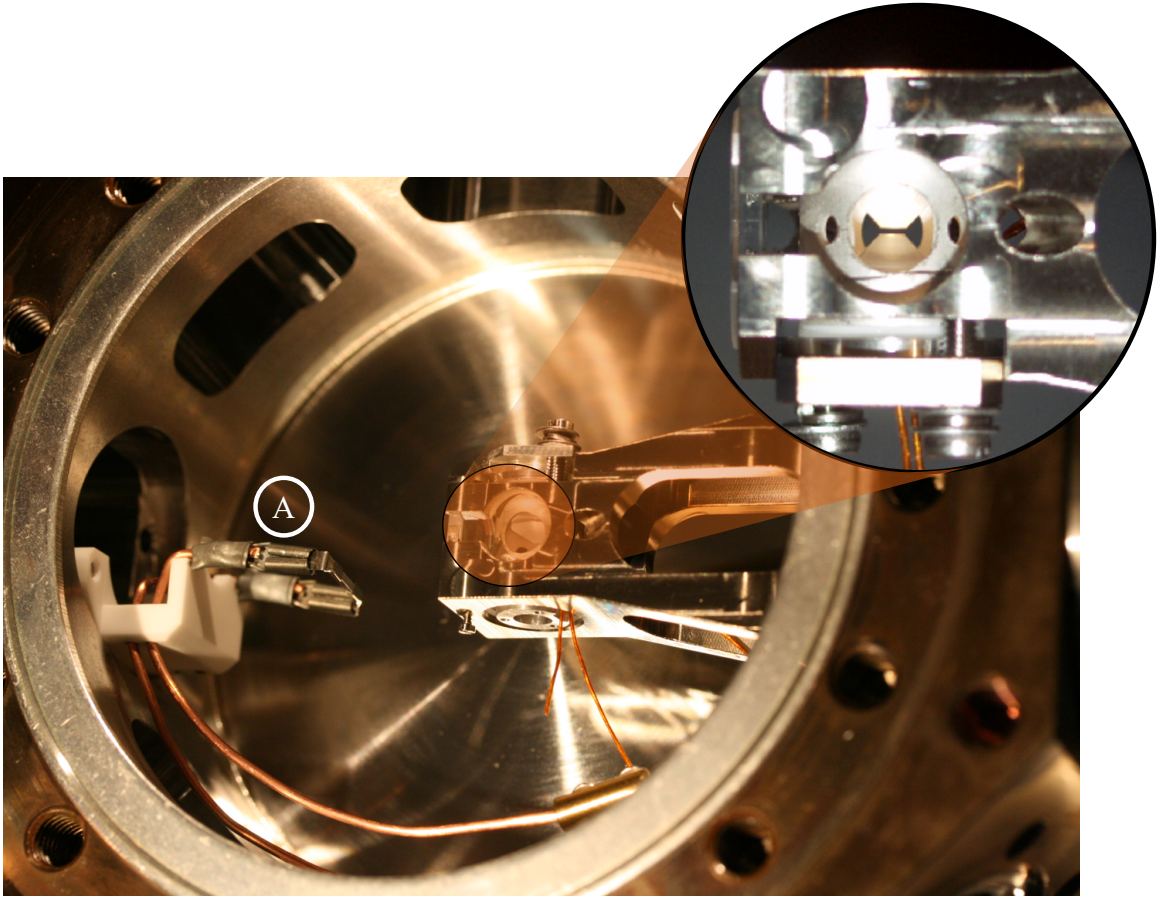
Figure 1.1: **Photography of the vacuum chamber and the optical cavity with the dispenser**. The atoms are released into the chamber from the current driven dispenser (indicated by circled white A), which is externally controlled and constantly kept on during experimental operation . The released atoms are then trapped in a magneto-optical trap and subsequently transferred to the center of the optical cavity (top right corner, zoomed in), as described in 2.3. The cavity is mounted in a piezo tube, which is used to control the length and, consequently, the resonance frequency of the optical cavity. The parameters of the cavity are listed in Table 1.1. The cavity holder is designed such that optical access from all sides is possible, see Fig. 1.5.The photography was taken from [80, 81] and modified.

Table 1.1: **Cavity parameters and relevant decay rates for our system.**

| cavity parameters | |
|---|---|
| cavity length $L$ | $485(1)\,\mu m$ |
| free spectral range (at $780\,nm$) | $309\,GHz$ |
| Finesse $\mathcal{F}$ | $61\,000(2000)$ |
| mirror Transmission $T_1$ & $T_2$ | $92(3)\,ppm$ & $3(1)\,ppm$ |
| round trip loss | $102(3)\,ppm$ |
| mode waist (TEM00 mode) | $29\,\mu m$ |
| **rates & cooperativity** | |
| total cavity field decay rate $\kappa$ | $2\pi \times 2.5\,MHz$ |
| decay rate outcoupling mirror $\kappa_{out}$ | $2\pi \times 2.3\,MHz$ |
| atomic polarization decay rate $\gamma$ | $2\pi \times 3\,MHz$ |
| theoretical atom-cavity coupling $g$ for | |
| $\quad |F{=}2, m_F{=}2\rangle \to |F'{=}3, m_F{=}3\rangle$ | $2\pi \times 8.1\,MHz$ |
| $\quad |F{=}1, m_F{=}\pm\rangle \to |F'{=}1, m_F{=}0\rangle$ | $2\pi \times 5.2\,MHz$ |

## 1.2 Level scheme of $^{87}$Rb and qubit

The experiments in this thesis were performed with $^{87}$Rb atoms. $^{87}$Rb is part of the group of alkali metals and possesses only one valence electron, which lies in the $5s$ orbital. From this $5s$ ground state, the electron can be excited to the $5^2P_{1/2}$ state and the $5^2P_{3/2}$ excited states, which are dipole-allowed optical transitions. These transitions, which are the $5^2S_{1/2} \to 5^2P_{1/2}$ $D_1$ line at $794.978\,nm$ and $5^2S_{1/2} \to 5^2P_{3/2}$ $D_2$ line at $780.241\,nm$, form together the D-line fine structure doublet. The values used here and in the following of this section are taken from [82]. In $^{87}$Rb, there are many more optical transitions, but in this thesis, we only perform experiments using the D-line fine structure doublet. The nuclear angular momentum of $^{87}$Rb is $I = 3/2$. Therefore, the ground state $5^2S_{1/2}$ is split into two hyperfine states $|F{=}1\rangle$ and $|F{=}2\rangle$. The excited states $5^2P_{1/2}$ and $5^2P_{3/2}$ are split into two ($|F{=}1\rangle$ and $|F{=}2\rangle$) and four ($|F{=}0\rangle$, $|F{=}1\rangle$, $|F{=}2\rangle$ and $|F{=}3\rangle$) hyperfine states.[2] The hyperfine states themselves are split into $2F + 1$ magnetic sublevels (ranging from $m_F{=}-F, \ldots, m_F{=}0, \ldots, m_F{=}F$) and, for the bare atom, the sublevels are degenerate in energy. However, the trapping potentials induce a light shift and lift the degeneracy for some of the sublevels and, therefore, these are non-degenerate [83]. The overall structure of these levels, including the light shifts, is in Fig. 1.2,

---

[2]In this thesis, if the exact fine structure level is not indicated, we will indicate the excited states with a prime, e.g., $|F'{=}2\rangle$ refers to a hyperfine state of one of the excited states, whereas $|F{=}2\rangle$ refers to the hyperfine ground states. If it is not clear from the context which excited fine structure level is being referred to, the exact fine structure level is specified.

where we give the light shifts of the individual magnetic sublevels with respect to the hyperfine levels and the hyperfine energy shift with respect to the fine structure levels. The number in MHz on top of each magnetic level indicates the induced light shift. These numbers are partly obtained by spectroscopic measurements and partly by calculations. During the experimental sequence, we apply a magnetic guiding field along the cavity axis ($y$-axis), which induces an (anomalous) Zeeman shift given by $\Delta E(F, m_F) = \mu_B g_F m_F B$, where $\mu_B$ is the Bohr magneton, $g_F$ the Landé g-factor, $m_F$ the magnetic sublevel and $B$ the magnitude of the magnetic field. The energy shifts on the ground states induced by the Zeeman effect are shown in Fig. 1.3. As the Landé g-factor has opposite signs for $|F{=}1\rangle$ and $|F{=}2\rangle$ for the ground state $5^2S_{1/2}$ in $^{87}$Rb, the energy shifts of the hyperfine levels have an opposite sign. The atomic qubit that we use for the generation of the atom-photon entanglement in chapter 3 is circled in red. The qubit states are $|F{=}1, m_F{=}1\rangle \coloneqq |\uparrow\rangle$ and $|F{=}1, m_F{=}-1\rangle \coloneqq |\downarrow\rangle$ of the $5^2S_{1/2}$ ground state. For the experiments in this thesis, we use a magnetic guiding field which induces a single Zeeman splitting of $2\pi \times 100\,\text{kHz}$, which leads to a frequency splitting of the qubit of $2\pi \times 200\,\text{kHz}$.
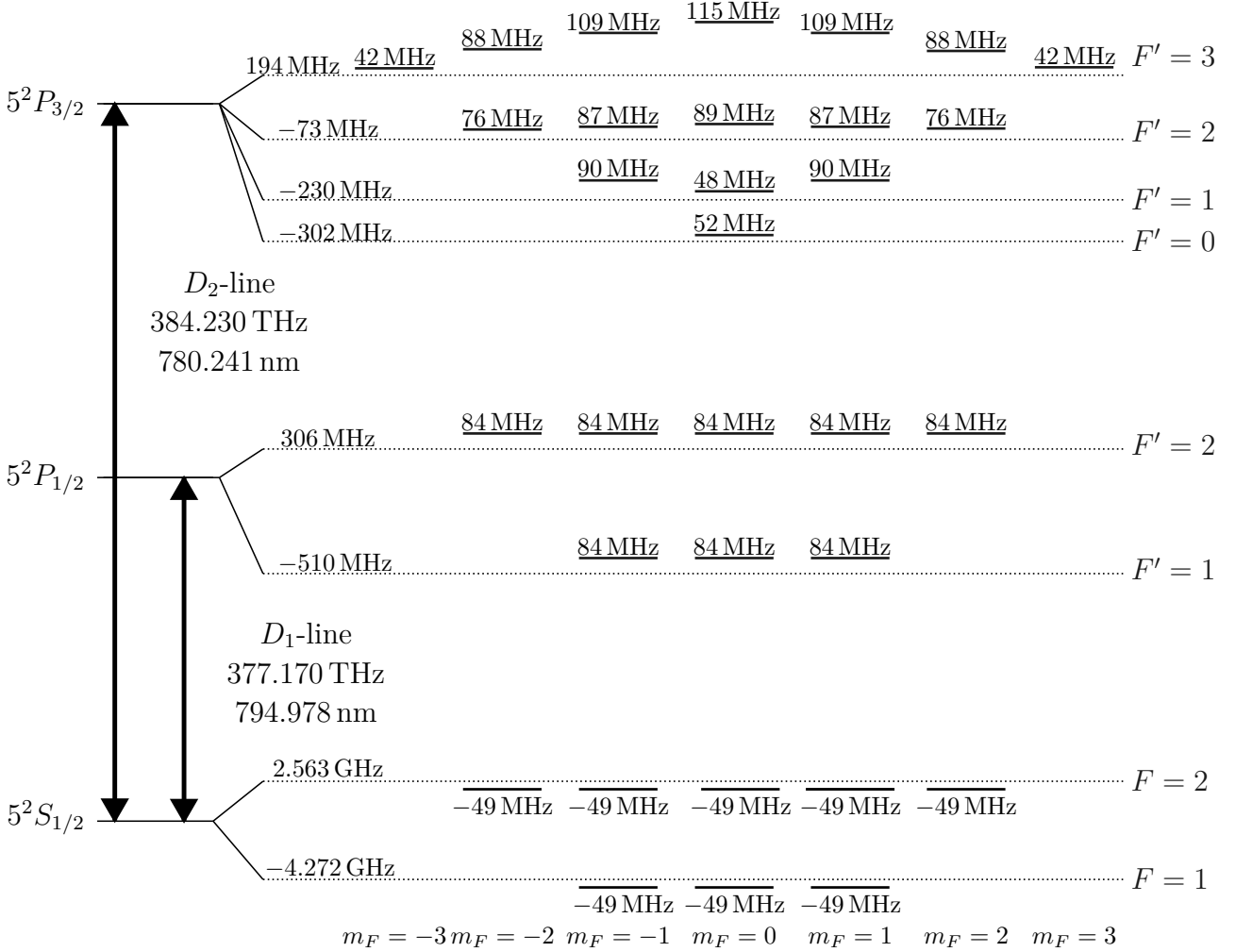
Figure 1.2: **Level scheme of the ground state $5^2S_{1/2}$ and the excited states $5^2P_{3/2}$ and $5^2P_{1/2}$ of $^{87}$Rb, including the light shifts for our experimental parameters**. The atoms are trapped in a two-dimensional optical lattice with one 1064 nm and one 770 nm standing wave trap. However, the 1064 nm trap is mostly responsable for the induced light shifts of the individual levels. The induced light shift for each individual Zeeman sublevel with respect to the bare atomic levels is indicated by the numbers on top of each level in MHz. As expected, the red-detuned trap shifts the excited states towards higher and the ground states towards lower energies. The values given here are for a beam waist of 13 µm and a power of 1 W of the 1064 nm trap. The numbers for the bare atomic levels and the transition frequencies are taken from [82].
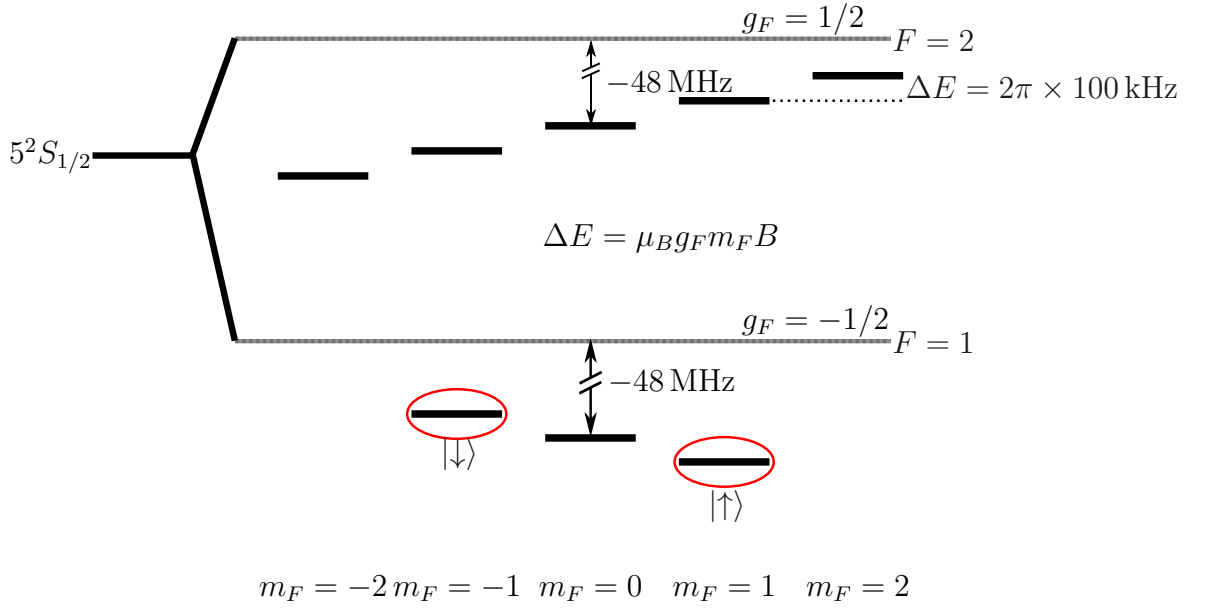
Figure 1.3: **Zeeman shift of the ground states of** [87]Rb. On top of the light shift induced by the lattice, the applied magnetic guiding field induces a Zeeman shift, that depends on the specific magnetic sublevel. The energy shift of the individual sublevels is given by $\Delta E = \mu_B g_F m_F B = \pm 0.7\,\frac{\mathrm{MHz}}{\mathrm{G}} m_F B$ [82], where the positive and negative sign account for the different Landé g-factors $g_F = \pm 1/2$ of the $|F{=}1\rangle$ and $|F{=}2\rangle$ hyperfine ground states. By choosing the magnetic guiding field appropriately, we set a single Zeeman splitting of $2\pi \times 100\,\mathrm{kHz}$. The qubit used in chapter 3 for atom-photon entanglement is circled in red. The qubit states are $|F{=}1, m_F{=}1\rangle \coloneqq |\uparrow\rangle$ and $|F{=}1, m_F{=}-1\rangle \coloneqq |\downarrow\rangle$.

## 1.3 Two configurations for the cavity

The experiments that were performed in the QIP group of the quantum dynamics division in the past few years are based on two key operations: The generation of an optical photon using a so-called vSTIRAP (see section 1.6) and a controlled phase gate between an atom and a photon [77]. The experiments based on the controlled phase gate [75, 84–86] were mainly performed on the QGate experiment and the experiments based on the photon generation were mainly performed with the sister-experiment, the Pistol experiment, which has a very similar design [53, 87, 88]. However, both experiments, QGate and Pistol, can be used in both experimental configurations, i.e., to either generate photons with the vSTIRAP or implement an atom-photon phase gate. For example, in a combined experiment between both setups [45], both experiments were used in the "gate" configuration. For each of the two configurations, the optical cavity must be stabilized at a different resonance frequency. Fig. 1.4 shows both frequency configurations in a level scheme. To perform the controlled phase gate between an atom and a photon, the cavity is on resonance with the transition $|5^2S_{1/2}, F{=}2, m_F{=}2\rangle \to |5^2P_{3/2}, F{=}3, m_F{=}3\rangle$. This transition is selected because it comes with many advantages, as, for example, a high coupling to the cavity and an effective state initialization and readout. Therefore, for some of the experiments in this thesis, where, for example, an efficient state readout was needed, we used this gate configuration. In Fig. 1.4, this transition is indicated by the blue arrow and the frequency $\omega_{gate}$. For the photon generation, called "emission" configuration, many different configurations were used in the past years. For the experiment described in chapter 3, we used the same configuration as in [88]. In this configuration, the cavity is not on resonance with a specific transition, but detuned by $2\pi \times 200\,\mathrm{MHz}$ with respect to the transition $|5^2S_{1/2}, F{=}1\rangle \to |5^2P_{3/2}, F{=}1, m_F{=}1\rangle$, see Fig. 1.4, indicated by the red arrow $\omega_{emission}$. Unless explicitly state, the cavity is in this emission configuration throughout the whole thesis.
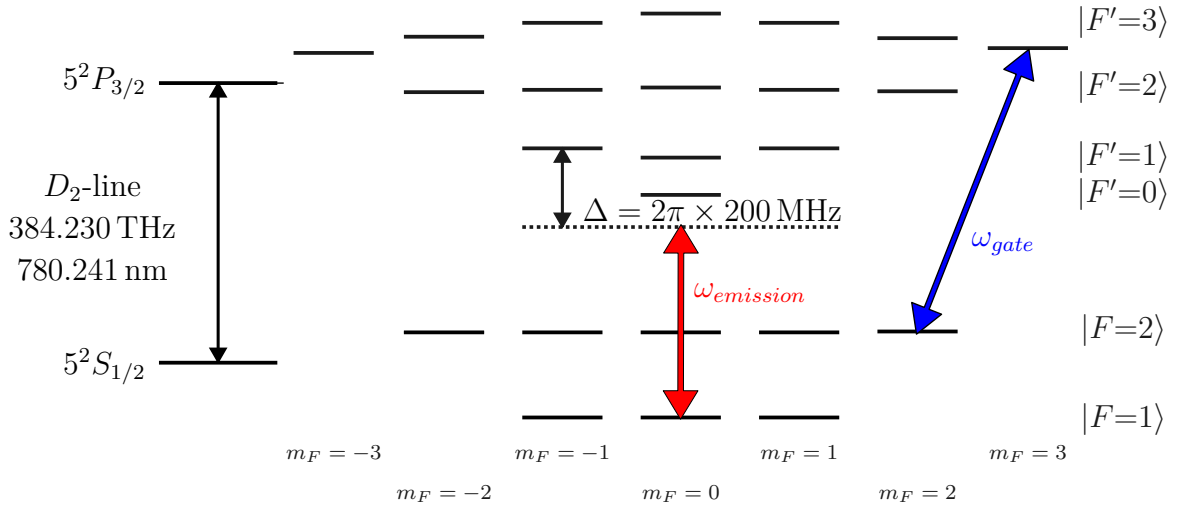
Figure 1.4: **Resonance frequency of cavity for photon emission and atom-photon phase gate.** The setup is used in two different cavity configurations, which we call "gate" configuration and "emission" configuration. In the gate configuration, the cavity is on resonance with the $|F{=}2, m_F{=}2\rangle \to |F'{=}3, m_F{=}3\rangle$ transition and the setup can be used to implement a controlled atom-photon phase gate [77]. In the emission configuration, the cavity is detuned by $2\pi \times 200\,\text{MHz}$ from the $|F{=}1, m_F{=}0\rangle \to |F'{=}1, m_F{=} \pm 1\rangle$ transition and can be used for the vSTIRAP to generate atom-photon entanglement, see section 1.6.

## 1.4 Trap configuration and beam arrangement

In this section we discuss the configuration of the traps as well as the spatial arrangement of all the incident beams that serve different purposes, like cooling, state initialization or single qubit rotations. The overall beam configuration is shown in Fig. 1.5. For trapping the atoms, we use a two-dimensional optical lattice. The lattice consists of a red-detuned, linearly polarized, retro-reflected standing wave trap, which runs orthogonal to the cavity axis, along the $x$-axis, at 1064 nm. We employ roughly 1 W of power, giving a trap frequency of several hundred kHz at a beam waist of $w_0 = 13\,\mu\text{m}$. Additionally, we use a blue-detuned standing wave trap that runs along the cavity axis ($y$-axis) at 770 nm, which forms together with the 1064 nm standing wave trap the two-dimensional optical lattice. The beam waist of the 770 nm is the same as the waist of the cavity TEM00 mode and is therefore 29 µm. The blue-detuned intracavity trap is used to stabilize the cavity length (see section 1.1) as well as to spatially confine the atoms to positions of maximum coupling (see 3.1.3). In former experiments, there was an additional blue-detuned, retro-reflected standing wave trap along the $z$-axis. However, this trap had to be removed, as it would have made it impossible to add the addressing systems due to space constraints. For the cooling of the atoms, we use a pair of linearly polarized, counterpropagating beams in a lin⊥lin configuration for polarization gradient cooling (including the necessary repumper to bring the population back from $|F{=}1\rangle$ to $|F{=}2\rangle$ via the excited state $|5^2S_{3/2}, F{=}2\rangle$). The cooling beams impinge from

opposite directions under 45°in the $x-y-$plane. In this configuration, we observe typically a storage time of approximately 60 s for a single atom. Single qubit rotations are implemented with a pair of Raman beams that run parallel to the 1064 nm standing wave axis. The beam waist of the Raman beams is $w_0 = 82\,\mu$m [89]. The $\pi$-polarized pump beam that we use to initialize the atom in $|F{=}2, m_F{=}0\rangle$ as well as the global vSTIRAP beam also run along this axis, but from the opposite direction. Both the state initialization and the global vSTIRAP beam have a waist of about 35 µm. The $\sigma^+$-polarized pump light to initialize the atoms in $|F{=}2, m_F{=}2\rangle$ is sent along the quantization axis (resonator axis) and coupled into the cavity through the highly reflective cavity mirror. The light used for the state detection in the gate configuration runs parallel to the cooling light and the repumper under $45°$ in the $x - y$-plane. It is $\sigma^+ + \sigma^-$-polarized and drives the cycling transition $|F{=}2, m_F{=}2\rangle \rightarrow |F{=}3, m_F{=}3\rangle$ (see section 1.7). Light from the addressing setup is sent through the objective and is incident along the $z$-axis. The beam waist of the addressing beam is 1.40(5) µm and therefore allows the addressing of individual atoms at 780 nm (see section 2.2.3). An overview about the beam waists of the individual beams is given in Table 1.2.

Table 1.2: **Overview of the different beam waists.** All the waists are indicated as $1/e^2$ intensity radius.

| beam | waist $w_0$ (µm) |
|---|---|
| TEM00 mode of cavity | 29 |
| global Raman | 82 |
| cooling light | 35 |
| state detection | 35 |
| repumper | 35 |
| addressing | 1.40(5) |
| state initialization in $|F{=}2, m_F{=}0\rangle$ | 35 |
| global vSTIRAP | 35 |
| 1064 nm standing wave trap | 13 |
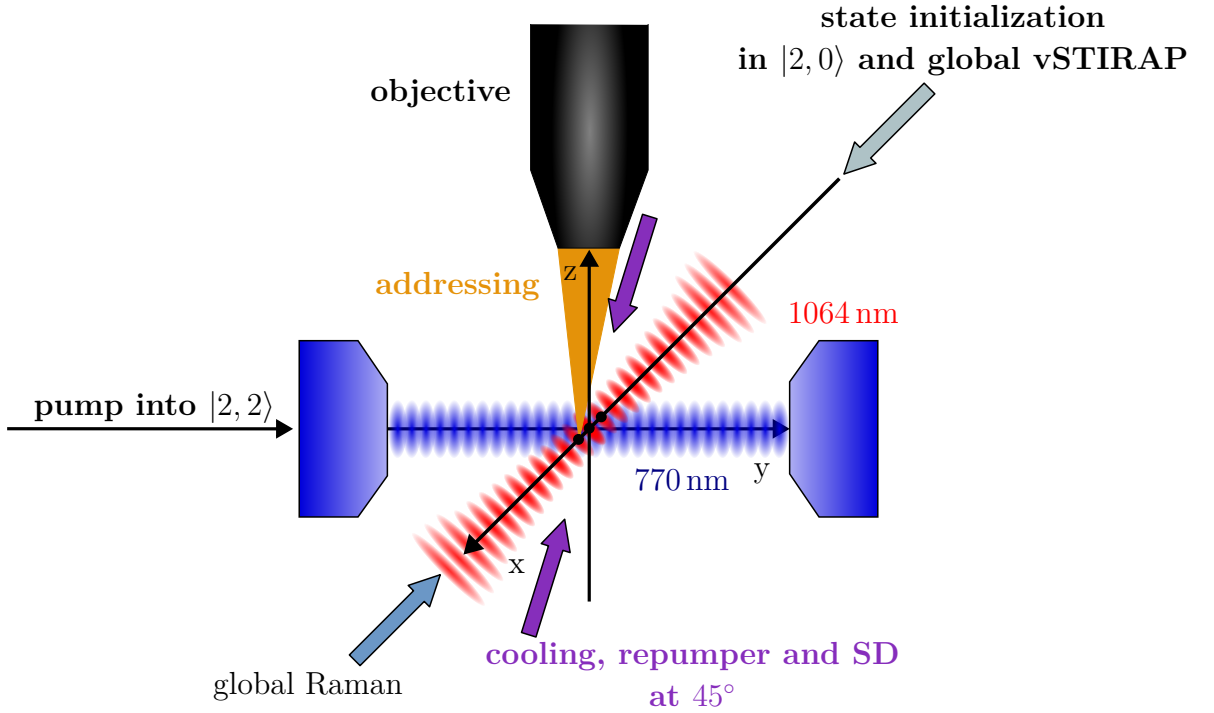
Figure 1.5: **Spatial configuration of the incident beams**. The $1064\,\text{nm}$ and $770\,\text{nm}$ standing wave traps for trapping run along the $x$-axis (orthogonal to the cavity axis) and the $y$-axis, respectively. The beams for cooling, the repumper and the state detection beams for the gate configuration (see section 1.3) impinge under $45°$ in the $x-y-$plane. The global Raman, the global vSTIRAP and the $\pi$-polarized beam for the optical pumping in $|F{=}2, m_F{=}0\rangle$ are all propagating along the same axis as the $1064\,\text{nm}$ standing wave trap axis ($x$-axis). To address individual atoms, the light is sent through the objective along the $z$-axis. Since pure $\sigma^+$-polarized light can only be incident along the quantization axis, the light to initialize the atoms in $|F{=}2, m_F{=}2\rangle$ is coupled into the resonator along the cavity axis.

## 1.5 Single qubit rotations

The basics of the single qubit rotations are discussed in this section. Details can be found in [89, 90]. Fig. 1.6 shows the working principle of the single qubit rotations. It is based on a stimulated Raman transition between the ground states $|F{=}1, m_F{=}1\rangle$ and $|F{=}2, m_F{=}2\rangle$ of $^{87}$Rb. Two light fields, called probe and control, couple the two ground states $|F{=}1, m_F{=}1\rangle$ and $|F{=}2, m_F{=}2\rangle$ via an excited state. The probe and control field are both detuned by the same amount $\Delta$, the so-called single-photon detuning, from the excited state and the two-photon detuning is selected so that $\delta = 0$, i.e. the states $|F{=}1, m_F{=}1\rangle$ and $|F{=}2, m_F{=}2\rangle$ are in two-photon resonance with the two-photon resonance frequency $\omega_{|F{=}1,m_F{=}1\rangle \rightarrow |F{=}2,m_F{=}2\rangle}$. If the single-photon detuning $\Delta$ is large, i.e. $|\Delta| \gg |\delta|, |\Omega_c|, |\Omega_p|$, the excited state is not populated during the transfer and the level scheme is reduced to an effective two-level system, allowing for a coherent population transfer between the ground states [91]. This way of implementing single qubit rotations was already used in Manuel Uphoff's thesis [90] as well as in previous experiments performed on this setup in the past. However, in these experiments, a maximum of two atoms was used, whereas in the present work up to six atoms are used. This changes the experimental requirements and we have therefore decided to build a new version of the Raman setup. The first change is that the Raman does not impinge anymore under 45° in the $x-y-$plane. Instead, it runs parallel to the 1064 nm standing wave trap. The waist of the Raman beams in the new setup is about 82 µm ($1/e^2$ radius of intensity). This way, we ensure a homogeneous intensity distribution of the Raman beams in the area of the atoms. In addition, the wavelength of the Raman laser is changed to 788.24 nm, giving a single photon detuning $\Delta$ that minimizes the differential light shift induced by the Raman lasers. The combination of the homogeneous intensity distribution across all atoms and the minimal differential light shift ensures that we do not have to track the phases of the individual atoms and correct for any phase differences between the atoms. In the previous version of the setup, the induced differential light shift was typically on the order of a few kHz, which made it necessary to track the phase evolution of the individual atoms. Tracking the phase evolution of each atom would be very challenging for multiple atoms or even impossible with the current setup. To reduce the phase noise, the light for the probe and the control beam both stem from the same laser. The ground state splitting in $^{87}$Rb is 6.8 GHz. To generate this frequency difference between probe and control, we use an electro-optic modulator (EOM) and combine it with acousto-optic modulators (AOM). The polarization of the probe is set to $\pi$ and the polarization of the control is set to $\sigma^+ + \sigma^-$. This allows for Raman transitions between magnetic sublevels of the ground states with $\Delta m_F{=} \pm 1$ are possible. However, in this configuration transitions between several Zeeman levels of the $^{87}$Rb ground states can be driven simultaneously. Therefore, we apply a magnetic guiding field along the cavity axis, which induces a Zeeman splitting (see section 1.2) and leads to a frequency selectivity of the transitions. This means that one can drive individual transitions only when setting the two-photon frequency $\omega$ correctly. Fig. 1.7 shows a measurement of Rabi oscillations on the transition $|F{=}1, m_F{=}1\rangle \rightarrow |F{=}2, m_F{=}2\rangle$ for the two-photon frequency $\omega_{|F{=}1,m_F{=}1\rangle \rightarrow |F{=}2,m_F{=}2\rangle}$. More details about the new
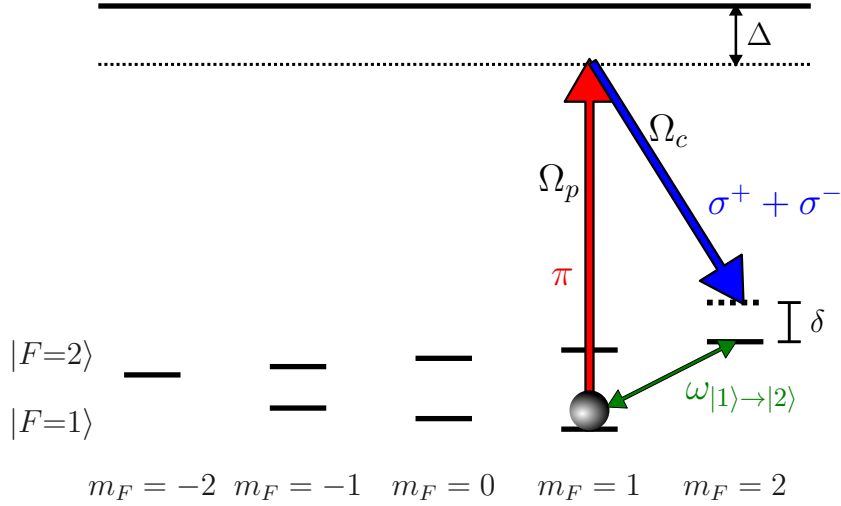
Figure 1.6: **Working principle of single qubit rotations using stimulated Raman transitions.** Here, we illustrate the transition $|F{=}1, m_F{=}1\rangle \to |F{=}2, m_F{=}2\rangle$. The polarization configuration of the probe ($\pi$-polarized) and the coupling ($\sigma^+ + \sigma^-$) beams allows for transitions with $\Delta m_F = \pm 1$. However, due to the Zeeman shift induced by the magnetic guiding field, the degeneracy of the magnetic sublevels are is lifted and transitions between individual magnetic sublevels can be driven by setting the two-photon detuning $\delta$ appropriately. If the single-photon detuning $\Delta$ is sufficiently large(($|\Delta| \gg |\delta|, |\Omega_c|, |\Omega_p|$)), the $\lambda$-scheme is effectively reduced to a two-level system, allowing for the coherent transfer between individual magnetic sublevels.[91].

Raman setup can be found in [89].
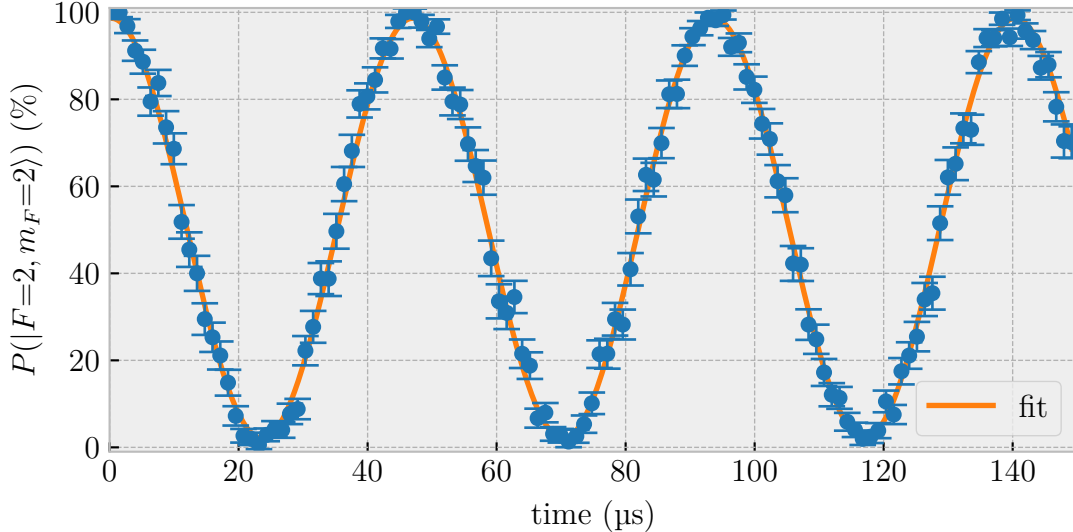
Figure 1.7: **Example of Rabi oscillations between** $|F{=}2, m_F{=}2\rangle \rightarrow |F{=}1, m_F{=}1\rangle$**.** The atoms are initialized in the state $|F{=}2, m_F{=}2\rangle$. Afterwards, coherent oscillations between the states $|F{=}2, m_F{=}2\rangle$ and $|F{=}1, m_F{=}1\rangle$ are driven using stimulated Raman transitions. In this example, the period of the Rabi oscillations is $T = 46.70(7)\,\mu s$. For the selected magnetic sublevels, the coherence time is typically on the order of several hundreds of µs.

## 1.6 Photon & Entanglement generation

In this section, the principle of photon generation is explained. It is based on a process called vacuum stimulated Raman adiabatic passage (vSTIRAP) [92, 93]. The same principle can also be used to generate atom-photon entanglement (APE) or even photon-photon entanglement [53]. The underlying principle is illustrated in Fig. 1.8A. The required level scheme to implement the vSTIRAP is a lambda system with two ground states $|g_1\rangle$ and $|g_2\rangle$ and one excited state $|e\rangle$. One of the ground states, in our case $|g_1\rangle$, is coupled to the excited state $|e\rangle$ via a control field with Rabi frequency $\Omega$. The same excited state is coupled to the second ground state $|g_2\rangle$ via the cavity with the atom-cavity coupling $g$. The frequency of the cavity and the frequency of the control light field are both detuned by the value $\Delta$ with respect to the excited state $|e\rangle$ and the two-photon detuning is $\delta = 0$, i.e., the transition $|g_1\rangle \rightarrow |g_2\rangle$ is in two-photon resonance. After initializing the system $|g_1\rangle$, the population can be coherently transferred from $|g_1\rangle$ to $|g_2\rangle$ using the two light fields and the coherent emission of a photon into the cavity mode is stimulated. The same process can be used to entangle the polarization of the generated photon to the internal atomic states of the atom: If the excited state couples to two atomic ground states with coupling constants $g_{\sigma+}$ and $g_{\sigma-}$, but different polarizations, i.e. $\sigma^+$ and $\sigma^-$, the polarization of the generated photon is entangled to the internal atomic state after the photon emission. In part B of Fig. 1.8, we show how this process can be implemented using the level structure of $^{87}$Rb. At first, the atom is initialized in $|F{=}2, m_F{=}0\rangle := |0\rangle$ and transferred into the states $|F{=}1, m_F{=}1\rangle := |\uparrow\rangle$ and $|F{=}1, m_F{=}{-}1\rangle := |\downarrow\rangle$ after the stimulated emission of the photon. If $g_{\sigma+} = g_{\sigma-}$
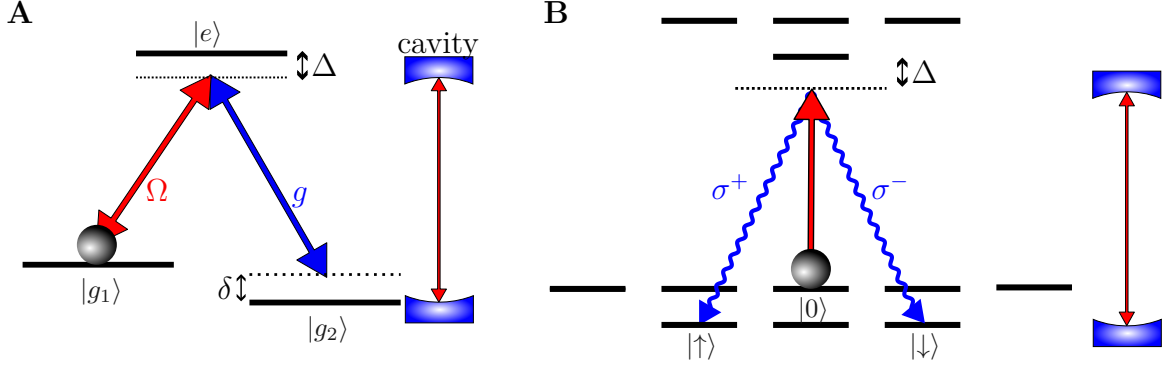
Figure 1.8: **Photon and entanglement generation**. **A** Photon generation scheme. The two ground states, $|g_1\rangle$ and $|g_2\rangle$, of a $\lambda$-scheme are coupled to the excited state $|e\rangle$ via a control field and the cavity mode, respectively. The transition $|g_1\rangle \rightarrow |g_2\rangle$ is on two-photon resonance, i.e., $\delta = 0$. The resonance frequency of the cavity and the frequency of the control light field are both detuned by the same value $\Delta$ from the excited state, the single-photon detuning. As the population is coherently transferred from $|g_1\rangle$ to $|g_2\rangle$ in a vSTIRAP process, the emission of a photon into the cavity mode is stimulated. **B** The level scheme is extended to multiple levels. If the initial state $|0\rangle$ is coupled equally to the two states $|\uparrow\rangle$ and $|\downarrow\rangle$, i.e. $g_{\sigma^+} = g_{\sigma^-}$, the final state is $|\Psi_{final}\rangle = \frac{1}{\sqrt{2}} (|\sigma^+,\uparrow\rangle + |\sigma^-,\downarrow\rangle)$. This is the maximally entangled Bell state with the polarization of the generated photon entangled to the internal atomic state of the atom.

(as it is the case for our cavity), the atom ends up with equal probabilities in either $|\uparrow\rangle$ or $|\downarrow\rangle$ and the generated entangled state is

$$\Psi_{final} = 1/\sqrt{2} \left( |\uparrow,\sigma^+\rangle + \exp(i\phi) |\downarrow,\sigma^-\rangle \right). \tag{1.1}$$

The phase $\phi$ depends on the phase of the control field and the chosen geometry. If the phase is $\exp(i\phi) = 1$, the generated state is the maximally entangled Bell state $|\Psi^+\rangle$. We employ a single-photon detuning $\Delta$ of $2\pi \times 200\,\text{MHz}$, see section 3.1.2. This presented scheme corresponds to the protocol that we use in chapter 3 to generate APE.

## 1.7 State detection in the gate configuration

In the gate configuration (see section 1.3), the atomic qubit is stored in the states $|F{=}1, m_F{=}1\rangle$ and $|F{=}2, m_F{=}2\rangle$ and a state detection scheme needs to be able to differentiate between these two states. As both states are separated in frequency by the ground state splitting of roughly $6.8\,\text{GHz}$, we can use a fluorescence state detection scheme. In such a scheme, we collect the fluorescence from the atom when sending light resonant with the cavity frequency $\omega_{|F=2,m_F=2\rangle \rightarrow |F'=3,m_F=3\rangle}$. This light excites population from the $|F{=}2\rangle$ hyperfine state, but population in $|F{=}1\rangle$ is not excited. Purcell enhancement leads to a rate of $\gamma_c = g^2/\kappa$ (when atom and cavity are on resonance) at which photons are emitted into the cavity, giving an enhancement of $\gamma_c = 2C\gamma$ [94, 95]. The transition $|F{=}2, m_F{=}2\rangle \rightarrow |F'{=}3, m_F{=}3\rangle$ is a cycling
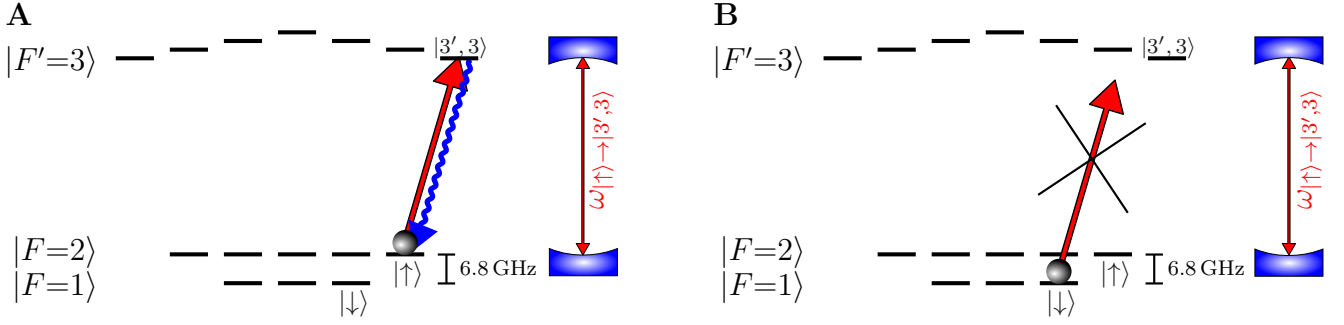
Figure 1.9: **State detection in gate settings**. The state detection protocol is based on a fluorescence detection scheme. The cavity and the state detection light are on resonance with the transition $|\uparrow\rangle \rightarrow |F'=3, m_F=3\rangle$. **A** If the atom is in the state $|\uparrow\rangle$, the state detection light excites the atom, and subsequently fluorescence is emitted from the atom and collected through the cavity **B** If the atom is in $|\downarrow\rangle$, the atom is not excited and no fluorescence is emitted, i.e. the atom remains dark.

transition and, therefore, the atom can be excited many times before decaying into the $|F=1\rangle$ hyperfine state, where it remains dark. The state detection light is sent onto the atoms from both sides, i.e., in a counter-propagating way, to reduce heating or even atom loss due to radiation pressure [94], see Fig. 1.5. The number of detected clicks while the state detection light is on, allows to distinguish between the states $|F=1, m_F=1\rangle$ and $|F=2, m_F=2\rangle$. Overall, this state detection scheme allows for a fast state readout on the order of a couple of µs and we achieve a state detection fidelity higher than 99.5 % if the atom is trapped in the two dimensional lattice (1064 nm and 770 nm standing wave traps) and we use the global state detection beam with a beam waist of 30 µm. However, if the state detection light is injected onto the atoms using the addressing setup, the state detection fidelity is lower. The main reason for that is the jumping of the atoms in the lattice, which happens on a time scale faster than our imaging rate ( one picture in 300 ms), see section 3.2.2. This means that the addressing is not always aiming at the position of the atom and therefore the average number of photons detected during the state detection interval drops when the atom is in the state $|F=2, m_F=2\rangle$ compared to the global state detection beam. This means that it is not always possible to differentiate between the two hyperfine ground states, since the average number of detected photons in the state detection $|F=1, m_F=1\rangle$ is similar to the one in the state $|F=2, m_F=2\rangle$. However, in this thesis, we work with the atom in the emission configuration most of the time and, therefore, we have not further investigated the reason for this heating mechanism and the reduction of the fidelity.

# Chapter 2

# Addressing setup, optical tweezers & generation of atomic arrays

A big part of this thesis was the extension of the existing QGate experiment with a so-called single atom addressing and positioning setup. This new addressing and positioning setup is supposed to enable two things:

- **The creation of optical tweezers.** Optical tweezers are highly focused laser beams that can be used to trap and move individual atoms. Such optical tweezers allow for the creation of arrays of atoms in the cavity and to overcome the limitations of the previously implemented, probabilistic loading scheme.

- **The individual addressing of single atoms**. By using highly focused laser beams, individual atoms can be addressed without any crosstalk between neighboring atoms in atomic arrays. This ability allows to to perform certain operations in an array of atoms only on a single atom instead of on the entire array globally. These possible operations are, for example, the generation of atom-photon entanglement, controlling the coupling of individual atoms to the resonator or gates on individual qubits, e.g., the controlled atom-photon phase gate or qubit rotations. In the previously existing version of the setup, there was no such strongly focused laser beam and it was only possible to perform these operations globally, i.e., on all atoms simultaneously.

However, the new setup had to be integrated into the existing setup without affecting the experimental possibilities already implemented [74–77]. The resulting design of the new addressing system is described in this chapter of the thesis. Additionally, the main features of the optical tweezers and the addressing and positioning system are described and characterized, and we explain how we use them to load atomic arrays into the resonator.

## 2.1 Addressing and positioning setup

The final design of the setup can be seen in Fig. 2.1. The pre-existing part is circled with the blue dashed line. We built the new setup on a breadboard which we placed on top of the existing setup. This was necessary due to the limited spaced.

At the heart of the new addressing setup are the two two-dimensional acousto-optic deflectors (2D AOD) (model DTSXY-400 from AA OPTO-ELECTRONIC). Each two-dimensional AOD consists of two one-dimensional AODs mounted orthogonally. AODs are based on the acousto-optic effect [96] and are used to deflect light beams at a desired angle $\theta$, depending on the frequency of the applied acoustic wave. By changing the frequency inputs of each one of the two AODs, the 2D AOD can scan a two-dimensional grid. The model we use is able to scan angles of several 10 mrad for wavelengths in the range of 770 nm to 810 nm. The two 2D AODs in our setup serve different purposes: One of the two generates the static tweezers for the initial atom loading, called static tweezers. The other one generates movable tweezers for the rearrangement of the atoms (see section 2.3). The 2D AOD of the movable tweezers is also used to address the individual atoms. It is possible to generate a single atom addressing beam in the wavelength range of 770 nm to 810 nm with the movable tweezers, as the input to this optical path comes from a combination setup in which light of different wavelengths can be combined. In contrast, the 2D AOD of the static tweezers is only used at the wavelength of the tweezers. The deflected output beams of the two 2D AODs are then centered for all output angles of the AODs on the back aperture of the imaging and addressing objective ($NA = 0.42$) using a $4f$ system. The angle of incidence on the objective $\theta_{obj}$ is given by the deflection angle $\theta_{AOD}$ of the AOD divided by the magnification $M$, i.e., $\theta_{obj} = \frac{\theta_{AOD}}{M}$, where the magnification $M$ is defined as the ratio between the focal lengths of the lenses in the $4f$ system. Hence, the angle of incidence on the objective $\theta_{obj}$ is controlled by changing the input frequency of the AODs. This change in angle then translates into a movement of the tweezers in the plane of the atoms. In our setup, there are two $4f$ systems for the two 2D AODs, because of to the different optical paths that we use to generate the tweezers. In the path of the movable tweezers, the focal length of the first lens of the $4f$ system is $f_{1,mov} = 125$ mm. In the path of the static tweezers, the focal length of the first lens is $f_{1,static} = 100$ mm. The lenses have different focal lengths, as there is not enough space in the path of the static tweezers on the breadboard to use a lens with a longer focal length. Both tweezer beams are superimposed after the first lens in each path using a PBS and then share their optical path from the PBS to the objective. Therefore, both optical paths share the second lens of the $4f$ system. This lens has a focal length of $f_2 = 1000$ mm. Because of the difference in focal length of the first lens in both optical paths, both paths have a different magnification. The path of the static beam has a magnification of $M_{static} = 10$ and the movable beam has a magnification of $M_{movable} = 8$. Therefore, this results in different beam waists for the two beams on the back of the objective and therefore also slightly different beam waists in the focus of the addressing objective, which corresponds to the plane of the atoms. The objective was specially designed for our setup and is described in more detail in [97]. The waists of the tweezers are discussed in more detail in section 2.2.3. After the second lens, there is a dichroic mirror (custom-made by SCHOTT) to separate the fluorescence from the atoms and the incoming addressing beam or tweezers. The Schott mirror fulfills some special requirements, such as an angle of incidence of 30° and a
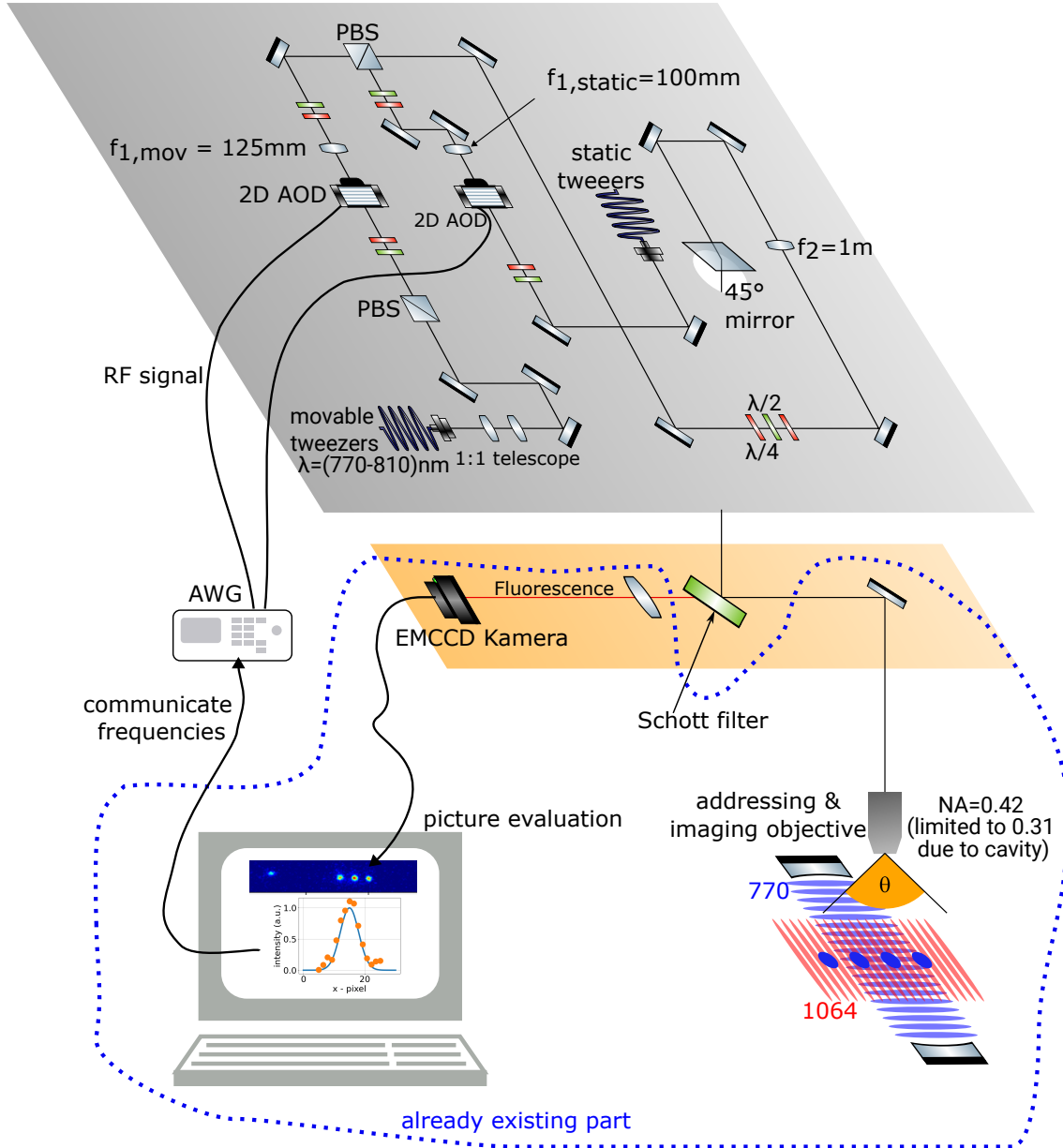
Figure 2.1: **Sketch of addressing and positioning system and setup**. The system is built on top of the previously existing setup (circled in blue) . It used to generate optical tweezers and address individual atoms. We use two different, two-dimensional acousto-optic deflectors (AODs) to generate static and movable tweezers. The movable tweezers and single atom addressing beam are generated with one AOD and the other AOD is used to generate the static tweezers array. An AOD deflects an input beam, depending on the applied RF frequency using the acousto-optic effect. A $4f$ system together with the imaging and addressing objective then converts this deflection into a movement of the beam in the plane of the atoms. A dichroic mirror, called Schott mirror, reflects the incident light of the addressing and positioning setup, but transmits the fluorescence of the atom. The transmitted fluorescence is used to image the atoms with an electron-multiplying charged coupled device (EMCCD) camera. The images are analyzed with computer software . This way, we determine the positions of the atoms, which are then converted into a frequency and communicated to the AWG which outputs the corresponding RF signals for individual addressing or array preparation.
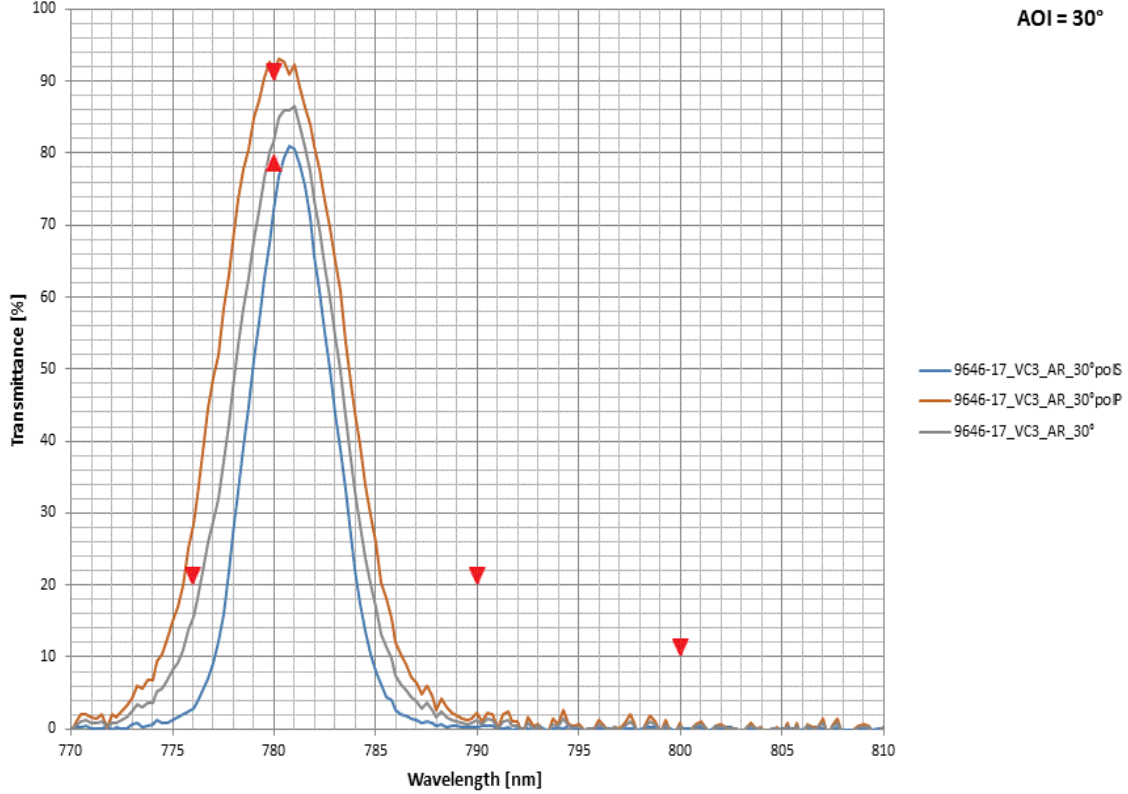
Figure 2.2: **Spectrum of the dichroic mirror (Schott mirror)**. We use a dichroic mirror, to spectrally separate the collected fluorescence of the atom and the light of the addressing system. As the angle of incidence of the beam from the addressing and positioning setup is 30°, we had the mirror manufactured externally by the company Schott. The most important requirements were a transmission of approximately 90 % at 780 nm, a high reflection in the wavelength range 770 nm to 810 nm, and a surface flatness better than $\frac{L}{10}$ on the reflective side to ensure good beam quality in reflection. The plot shows the transmission curves for p, s and unpolarized light.

surface roughness on the reflective side below $\lambda/10$ to ensure a good beam quality in reflection. The spectral properties of the dichroic mirror can be seen in Fig. 2.2. It acts as a dichroic mirror that transmits the fluorescence of the atoms at 780 nm and reflects light at wavelengths in the range of the optical tweezers. The Schott mirror reflects light below 780 nm as well, which allows, for example, to address the transitions $|5P_{3/2}\rangle \rightarrow |5D_{3/2}\rangle$ and $|5P_{3/2}\rangle \rightarrow |5D_{5/2}\rangle$. The fluorescence from cooling the atoms is collected through the imaging objective and subsequently transmitted through the dichroic mirror. Afterwards, it is focused with a lens onto the chip of an electron-multiplying charge-coupled device (EMCCD) camera, which is connected to a computer. This way, we generate images of the atoms, which are analyzed with self-written LabVIEW software, that we use to determine the position of the atoms. By trapping an atom in the optical tweezers and moving it precisely to different positions in the resonator (see section 2.2.4), we can assign to each pixel of the images a certain input frequency of the AOD. This allows to obtain a frequency-to-pixel conversion and allows toprecisely address individual atoms. The frequency input

**A**



**B**



**C**
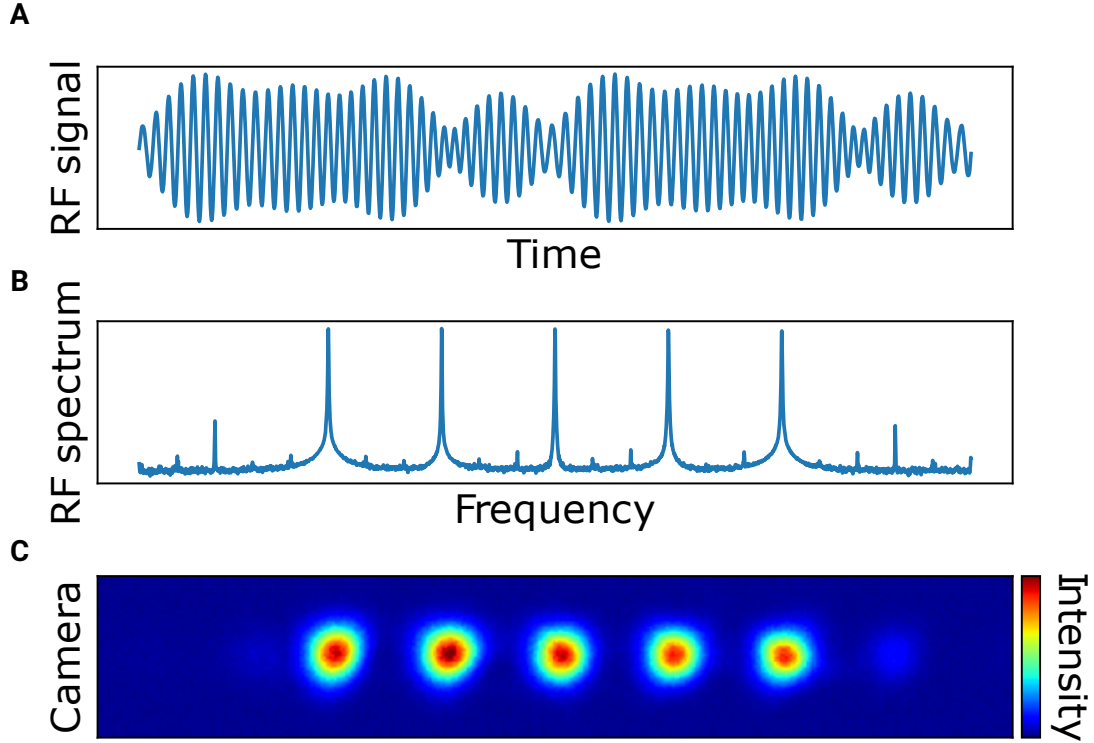


Figure 2.3: **One-dimensional tweezer array generated with an arbitrary waveform generator (AWG, M3202A from Keysight)**. **A** Multi-tone RF signal. To avoid too high RF power, the phases of the individual frequency components are selected as in [98]. **B** Frequency spectrum of the RF signal from part A. **C** Image taken with a CCD camera of the five optical tweezers generated with the RF signal in A.

to the AODs is generated by an arbitrary waveform generator (Keysight M3202A). To address an individual atom at a certain position in the atomic plane, we transmit the calculated frequency corresponding to the pixel to the arbitrary waveform generator, which then outputs the corresponding RF signal. As the atoms move in the between different lattice sites, it is necessary to follow the movement of the atoms. Therefore, we continuously take images of the atoms every 300 ms, evaluate the position of the atoms and adjust the frequencies to follow the movement of the atoms. For the creation of arrays of optical tweezers, we drive the static AOD with multiple radio-frequency tones. The phases of the individual frequency components are selected as in [98] to avoid damaging the AOD because of too high RF power. This is shown in Fig. 2.3. In part A, we show the multi-tone RF signal. In part B, there is the corresponding RF spectrum, and in C, an image taken with a CCD camera showing the generated five optical tweezers.

## 2.2 Characterizing the addressing and positioning setup & the optical tweezers

In this section, we characterize the most important properties of the optical tweezers and the addressing and positioning system. These properties are the trapping times and frequencies, the beam shape and the precision with which we can position atoms using the optical tweezers. The measurements are all taken with the movable tweezers (see 2.3). The static tweezers were only added to the setup after these measurements were taken. Since the optical components used to generate the static tweezers are very similar, the static tweezers have similar properties and, therefore, we decided not to characterize them.

### 2.2.1 Beam shape

To determine the shape of the addressing beam, we load a single atom into the two-dimensional standing wave lattice and address the atom through the addressing system using state detection light (see section 1.7). By scanning the input RF signal of one AOD, we scan the position of the addressing beam along one axis of the two-dimensional grid spanned by the AODs in the atomic plane with axes $x_f$ and $y_f$, which is rotated by an angle $\alpha$ with respect to the horizontal, see Fig. 2.4. The beam shape of the addressing beam can then be determined by collecting the emitted fluorescence of the atom in the cavity mode while the beam position is scanned over the atom. Fig. 2.4 shows a typical beam profile for scans along the $x_f$ (A) and $y_f$ (B) axes of the two-dimensional AOD. Along both axes, the beam shape is a Gaussian beam. Fitting the data with a Gaussian shape gives a waist of $w_{x_{AOD}} = 1.48(10)\,\mu m$ and $w_{y_{AOD}} = 1.77(12)\,\mu m$ along the $x_{\mathrm{AOD}}$ and $y_{\mathrm{AOD}}$, respectively, which is a slightly asymmetric beam. As the atoms are moving within the standing wave traps, the data were post-selected to use only data in which the atom did not move. These measurements were made at an early stage of the work presented in this thesis. The waist was further decreased and the alignment optimized during this thesis. The final beam waists are $w_{0,||} = 1.40(5)\,\mu m$ and $w_{0,\perp}\,1.38(3)\,\mu m$, see section 2.2.3.

### 2.2.2 Trapping times

To determine the trapping time of the atoms, we trap the atoms in the optical tweezers and cool the atoms until they are lost. We check if the atoms are lost by taking a picture every $300\,\mathrm{ms}$ with our imaging system and our self-written image evaluation software. The trapping time depends on many different parameters, e.g., the tweezer power or the cooling parameters. Fig. 2.5 shows a typical scan of the trapping time versus tweezer power for a tweezer wavelength of $800.12\,\mathrm{nm}$. The trapping time peaks at about $3.65\,\mathrm{mW}$ and decreases again for higher powers. This decrease is unexpected, as an increase in trapping power should not reduce the storage time. During this thesis, we have continuously changed the optical setup, e.g., we changed the wavelength of the light for the optical tweezers, realigned the optical tweezers, or changed the lens configurations of the $4f$ system. These changes
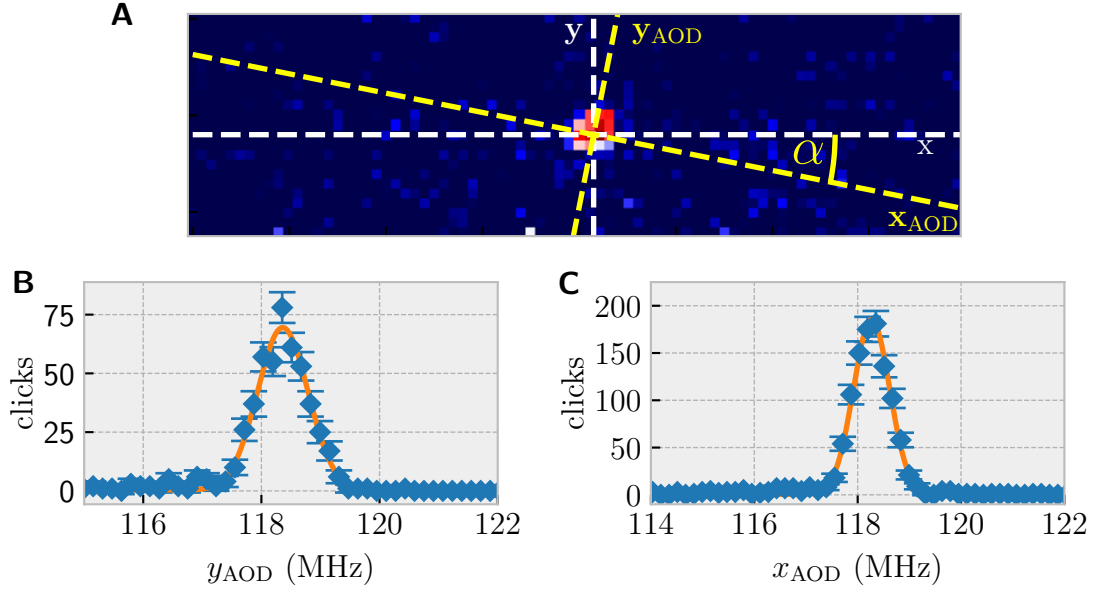
Figure 2.4: **Rotation of addressing system in the atomic plane and beam shape of addressing beam**. **A** The axes along which the beams of the addressing system move in the plane of the atoms are rotated by an angle $\alpha$ with respect to the horizontal. If the the input RF frequency of one of the AODs is scanned, the addressing beam moves along the $x_{\mathrm{AOD}}$ or $y_{\mathrm{AOD}}$ axis. By injecting state detection light into the addressing system and collecting the fluorescence through the cavity while scanning the input RF frequencies, the beam shapes along the $y_{\mathrm{AOD}}$ axis **B** and $y_{\mathrm{AOD}}$ **C** can be measured. From the data, we determine the beam waists to be $w_{x_{AOD}} = 1.48(10)\,\mu\mathrm{m}$ and $w_{y_{AOD}} = 1.77(12)\,\mu\mathrm{m}$ along the $x_{\mathrm{AOD}}$ and $y_{\mathrm{AOD}}$, respectively, which is a slightly asymmetric beam. During this thesis, the alignment was optimized and the lens configuration was changed, giving a smaller beam waist in the end, see section 2.2.3.
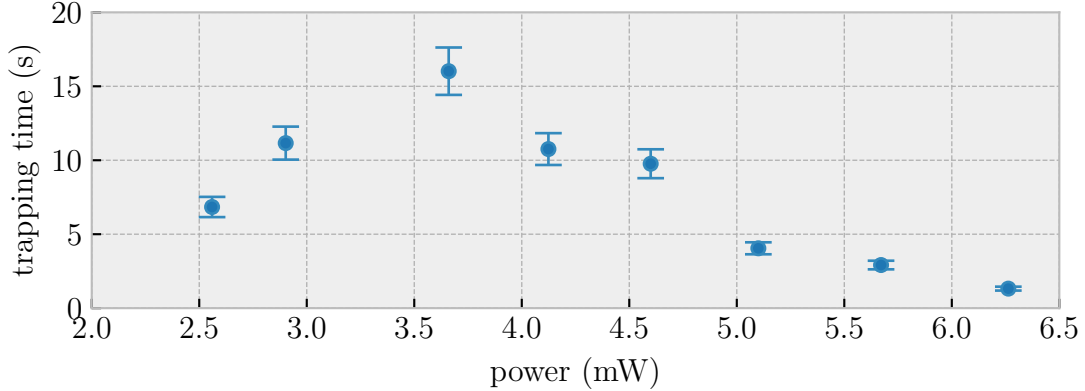
Figure 2.5:   **Trapping times in movable tweezers versus optical power**.
Changing the optical power of the tweezers changes the trap depth of the tweezers
and therefore results in different trapping times. The trapping time peaks at about
3.5 mW and decreases for higher optical powers. This decrease is unexpected, as
increasing the trap depth should not reduce the storage time. The storage time
is influenced by many different parameters, e.g., the lens configuration of the $4f$-
system, the alignment, or the cooling parameters. During this thesis, we tested a
lot of different settings and observed storage times in the range of 15 s to 30 s. This
measurement was taken for a tweezer wavelength of 800.12 nm.

all influenced the trapping time. However, for all the settings tested, the trapping
time was in the range of 15 s to 30 s.

### 2.2.3   Trap frequencies, waist & trap depth

In this section, we describe the measurement of the trap frequency of the movable
optical tweezers. The measurements were taken with a wavelength of $\lambda = 800.12$ nm.
In order to be able to assign a trap frequency to the tweezers, the tweezer potential
is approximated as a harmonic oscillator. This approximation is valid, as long as
the stays at the bottom of the tweezer potential, which is ideally the case. With this
approximation and assuming a Gaussian beam shape for the tweezers, the parallel
trap frequency $\nu_{||}$ (along the propagation direction of the tweezers) is given by

$$\nu_{||} = \frac{1}{2\pi}\sqrt{\frac{2U}{mz_R^2}}, \tag{2.1}$$

and the perpendicular trap frequency $\nu_\perp$ (perpendicular to the propagation direction
of the tweezers) by

$$\nu_\perp = \frac{1}{2\pi}\sqrt{\frac{4U}{mw_0^2}}. \tag{2.2}$$

Here, $U$ is the trap depth, $m$ is the atomic mass, $w_0$ is the beam waist, and $z_R$ is
the Rayleigh range. To then measure the trap frequency, we modulate the tweezer
potential sinusoidally at a frequency $\nu$. If the modulation frequency $\nu$ corresponds
to twice the parallel or perpendicular trap frequency, i.e., $\nu = 2\nu_{||}$ or $\nu = 2\nu_\perp$, the
atom is ejected from the tweezers because of parametric heating. Therefore, we

scan the modulation frequency $\nu$ while measuring the probability for the atom to not be ejected from the trap, i.e., the survival probability. The survival probability for different modulation frequencies is measured in three steps. First, we check if an atom is trapped in the tweezers with an initial fluorescence detection $SD1$ (see section 1.7). Then we modulate the potential. Afterwards, we check if the atom is still in the optical tweezers with a second fluorescence detection $SD2$. From this, we determine the survival probability $P(SD2|SD1)$ of the atom in the tweezers at the corresponding modulation frequency, i.e., the probability of detecting an atom in $SD2$ after the modulation given that an atom was detected in $SD1$ before the modulation. This experimental sequence for measuring the trap frequencies is shown in Fig. 2.6 A. The results of the measurement are shown in Fig. 2.6 B and C. We see the expected drop of the survival probability and we measure trap frequencies of $\nu_\perp = 137.5(4)\,\text{kHz}$ and $\nu_\parallel = 17.7(4)\,\text{kHz}$ for a power of $4.2\,\text{mW}$.

From the perpendicular (parallel) trap frequency $\nu_\perp$ ($\nu_\parallel$), the beam waist $w_0$ (the Rayleigh range $z_R$) and the trap depth can be determined. By measuring the trap frequency for different powers $P_{trap}$, one can use the following relationship to fit the result and determine the beam waist $w_0$ (Rayleigh range)[99]

$$w_0 = \left( \frac{\hbar\Gamma}{m\nu^2} \frac{P_{trap}}{\pi I_{sat}} \left( \frac{\Gamma}{3\delta_1} + \frac{2\Gamma}{3\delta_2} \right) \right)^{1/4} . \tag{2.3}$$

Here, $I_{sat}$ is the saturation intensity of the $D_2$ line, $\nu$ is the trap frequency, $\gamma$ is the linewidth of the $D_2$ line and $\delta_1$ and $\delta_2$ are the detuning between the wavelength of the optical tweezers and the $D_1$ and $D_2$ lines. We determine the parallel and perpendicular trap frequency for different powers and obtain from the fit a waist of $w_{0,\perp}1.384(3)\,\text{µm}$ using the perpendicular trap frequency and a Rayleigh range of $z_{R,\parallel} = 7.634(5)\,\text{µm}$ (corresponding to a waist of $1.394(5)\,\text{µm}$) using the parallel trap frequency $\nu_\parallel$, see Fig. 2.6 D and E. The fit includes measurement uncertainties in both the power $P$ and the measured trap frequencies $\nu_\perp$ and $\nu_\parallel$. From $w_{0,\perp}$ and $z_{R,\parallel}$, we are able to calculate the parameter $M^2 = 1.015(9)$, which indicates that the beam is highly Gaussian. Using $0.42\lambda/NA$ [97], we calculate the diffraction limited waist of the objective, which is $1.08\,\text{µm}$[1]. However, we use an input beam with a waist ($w_0 = 4\,\text{mm}$) that is smaller than the maximum and therefore we expect a beam waist of $1.26(23)\,\text{µm}$. The measured waist is within the error range of the expected value. As we know the trap frequency and the beam waist, we can determine the trap depth. It is approximately $1\,\text{mK}$ for a power of $4.2\,\text{mW}$ at a wavelength of $800.12\,\text{nm}$. However, as we use an array of optical tweezers to load the array of atoms, the number of individual tweezers is which we can generate is limited at this wavelength due to the power required per tweezer. To overcome this limitation, we use a wavelength of $797\,\text{nm}$ instead. At this wavelength, we only need $1\,\text{mW}$ to $2\,\text{mW}$ per tweezer to achieve a comparable trap depth.

---

[1]Note that here we use $NA = 0.31$ instead of $NA = 0.42$ as given in 2.1, as the cavity reduces the NA in one direction
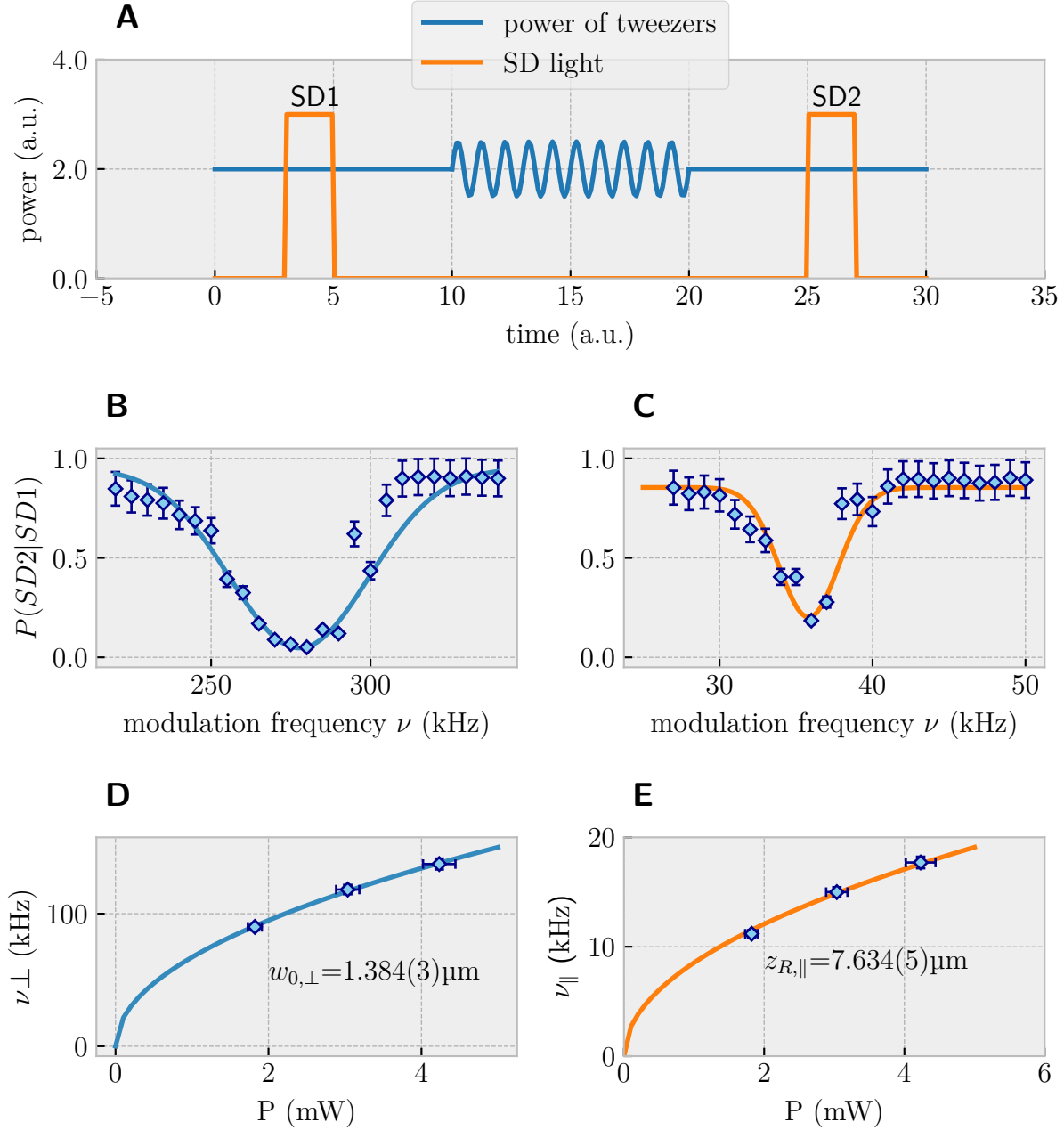
Figure 2.6: **Measurement of the trap frequency and the waist for the movable tweezers A** Experimental sequence. At the beginning, we check if an atom is trapped in the tweezers with a fluorescence detection ($SD1$) (see section 1.7). Then, we modulate the power of the tweezers and check if the atom survived the modulation with another fluorescence detection ($SD2$). The probability that the atom survived, given that it was present in $SD1$, i.e., $P(SD2|SD1)$, is measured for different modulation frequencies $\nu$ of the tweezer power. If $\nu = 2\nu_\perp$ or $\nu = 2\nu_\parallel$, the atom is ejected from the trap due to parametric heating. In **B** is the measurement for the perpendicular trap frequency, in **C** for the parallel trap frequency, giving $\nu_\perp = 137.5(4)\,\text{kHz}$ and $\nu_\parallel = 17.7(4)\,\text{kHz}$ at $4.2\,\text{mW}$ of optical power. From the perpendicular **D** and parallel trap **E** frequency for different optical powers, we determine the beam waist using equation (2.3). The fit gives a waist of $w_{0,\parallel} = 1.40(5)\,\mu\text{m}$ and a Rayleigh range of $z_{R,\parallel} = 7.634(5)\,\mu\text{m}$ (corresponding to a waist of $1.394(5)\,\mu\text{m}$), which indicates a highly Gaussian beam with $M^2 = 1.015(9)$.

## 2.2.4 Positioning

When loading multiple atoms without optical tweezers, i.e. with the previous probabilistic loading method, the distance between neighboring atoms cannot be controlled. However, controlling this distance is necessary to generate ordered atomic arrays. Optical tweezers allow for the precise positioning of atoms in the cavity. This capability is what we demonstrate in this section.

To move the atoms precisely to any desired position in the cavity, we first have to perform a frequency-to-pixel calibration, for which we use our EMCCD camera. From this calibration, we obtain a map $\phi$ that assigns to each pixel $(p_x, p_y)$ a RF input frequency pair for the AOD $(f_x, f_y)$, i.e., $\phi(p_x, p_y) = (f_x, f_y)$. To obtain this map, we measure for several pairs of pixels $(p_x, p_y)$ the corresponding frequency pairs $(f_x, f_y)$. To obtain a reliable frequency-to-pixel conversion, it is necessary that the pairs of pixels are distributed over the entire cavity area. To measure the frequencies that correspond to the pairs of pixels. we trap an atom in the tweezers and move it to a specific position by applying a specific frequency pair to the AOD and record the corresponding atomic position in pixels. We repeat this for each frequency pair a couple of hundred times. This is shown in Fig. 2.7. In this Fig., we show the recorded positions for twelve different frequency pairs. The conversion from pixel to position is obtained by using a conversion factor of $0.464(4)\,\mu\text{m/pixel}$ from a previous measurement of the pixel size. In part B of Fig. 2.7, we show a zoomed in version (circled in red in part A of the figure) of the measured positions for one frequency pair. Using this data set, we compute the full map $\phi$, which also includes the rotation angle $\alpha$ between the grid spanned by the 2D AOD and the horizontal. We obtain $\alpha = 14.60(5)°$. Additionally, we calculate the standard deviation (indicated by the blue circle) of the measured positions with respect to the center. We obtain $\sigma_x = 47(5)\,\text{nm}$ and $\sigma_y = 46(6)\,\text{nm}$. These standard deviations give us the positional deviation when repeatedly moving an atom to the same position. We attribute the uncertainty mostly to the error of the fit of the atomic position and therefore the obtained value is an upper bound of the positioning error. We can use this capability to precisely position the atom inside the cavity to resolve the beating pattern of the cavity mode, which we demonstrate in the following section.

When placing an atom inside a cavity, the transmission coefficient of the electric field through the cavity is given by [100] [101]

$$t(y) = \frac{2\sqrt{\kappa_l \kappa_r}(i\Delta_a + \gamma)}{(i\Delta_c + \kappa)(i\Delta_a + \gamma) + g^2(y)}. \tag{2.4}$$

Here, $\kappa, \kappa_l$ and $\kappa_r$ are the total cavity field decay rate and the decay rates through the left and right mirrors, $\gamma$ is the polarization decay rate, $\Delta_a = \omega_a - \omega$ is the detuning of the resonance of the atom $\omega_a$ with respect to the frequency of the driving laser $\omega$, $\Delta_c = \omega_c - \omega$ is the detuning of the resonance of the cavity $\omega_c$ with respect to the frequency of the driving laser $\omega$ and $g$ is the coupling of the atom to the resonator. As the electric field mode of the cavity is a standing wave, the coupling $g$ between cavity and atom oscillates along the cavity axis. Therefore, the intensity transmission $T(y) = |t(y)|^2$ of the cavity is position-dependent. For that reason, the
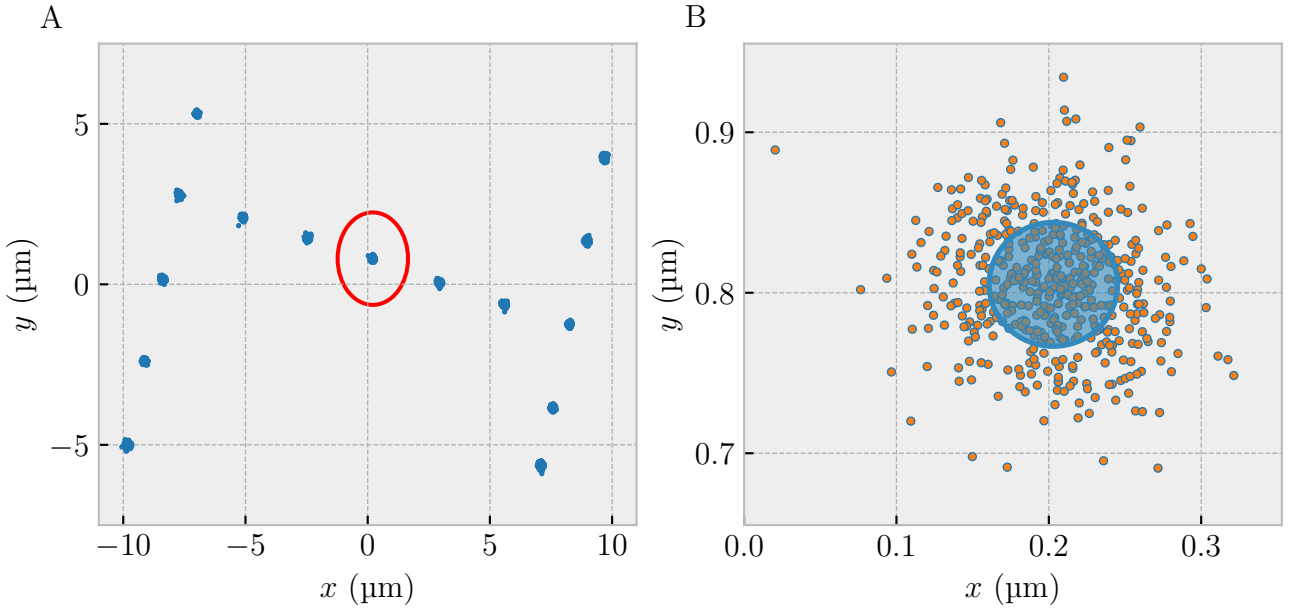
Figure 2.7: **Frequency-to-position conversion**. To be able to precisely position the atom in the cavity, we have to measure a map $\phi$, that assigns to each pair of pixels $(p_x, p_y)$ a frequency pair $(f_x, f_y)$ , i.e. $\phi(p_x, p_y) = (f_x, f_y)$, and vice versa. We find this map by repeatedly moving the atoms to different positions in the cavity, as we apply different input frequency pairs to the 2D AOD and record the position of the atoms by fitting the fluorescence images, see **A**. In **B**, there is a zoom (circled in red in part A) into the position measurements for one frequency pair. From this, we calculate a standard deviation (indicated by the blue circle) of $\sigma_x = 47(5)\,\text{nm}$ and $\sigma_y = 46(6)\,\text{nm}$ when repeatedly moving one atom to the same position. The positioning uncertainty results from the uncertainty of the fit of the atomic position and gives, therefore, an upper bound on the position uncertainty. From the fit, we obtain an angle of $14.60(5)°$ for the rotation between the grid spanned by the 2D AOD and the horizontal.

transmission of the cavity can be modulated by trapping an atom inside the optical tweezers and moving the atom along the cavity axis.

In the following, we use this modulation to demonstrate a positioning resolution with our optical tweezers better than $\lambda/2$. We show this by moving an atom along the cavity axis while we record the transmission through the cavity for different positions along the cavity axis during a probe light interval. To probe the cavity, we use $|\sigma^+\rangle$-polarized and both the cavity and the probe beam are set to resonance with the transition $|F{=}2, m_F{=}2\rangle \to |F'{=}3, m_F{=}3\rangle$, i.e. we work in the gate configuration (gate configuration, see section 1.3). At the beginning of each cavity probe interval, the atomic population is randomly distributed in the ground states. If the atom is located at an intensity maximum of the cavity field along the cavity axis, the $\sigma^+$-polarized cavity probe beam and a repumper from $|F{=}1\rangle$ to $|F{=}2\rangle$ optically pump the atom to $|F{=}2, m_F{=}2\rangle$, because the scattering of a probe photon increases, on average, the magnetic sublevel. As the coupling $g$ increases towards the end of the probe interval at positions of maximum intensity of the cavity field, the cavity transmission reduces, see Fig. 2.8 A. In Fig. 2.8 B, we plot the ratio between the number of clicks in the last $5\,\mu s$ $c_2$ and the first $5\,\mu s$ $c_1$ of the pumping interval, i.e., $c_2/c_1$, versus the position of the atom in the cavity. On the $x$-axis of the plot is the distance $y_{AOD}$, over which we move the atom with the optical tweezers. We determine this distance with the previously measured frequency-to-position conversion. If the atom is moved along the cavity axis, we expect to see a modulation period of the ratio $c_2/c_1$ of $\lambda_c/2 = 780\,\text{nm}/2 = 390\,\text{nm}$. However, from the fit we obtain a modulation period of $404(2)\,\text{nm}$. This difference can be explained by the rotation of the coordinate system of the 2D AOD with respect to the cavity axis. By fitting the data from Fig. 2.8 B using the model of equation (2.4), we find a rotation angle of $15(1)^\circ$, which is in good agreement with the angle of $14.60(5)^\circ$ obtained from the calibration measurement. The blue shaded curve indicates the error on the atomic position of $\sigma_x = 47(5)\,\text{nm}$. In this measurement, we show that we are able to resolve the positions of maximum and minimum coupling between the atom and the cavity and that we can position the atom within nodes and antinodes of the intracavity trap, i.e., with a higher resolution than $\lambda/2$. This resolution is only possible when the atoms are trapped in the optical tweezers. When we transfer the atoms back into the two-dimensional lattice for the entanglement generation, the atoms move at most by $328\,\text{nm}$, which is the maximum distance to the closest antinode of the two-dimensional lattice.

## 2.2.5 Extraordinary polarization components of the tweezers

The results presented so far were all satisfying and made us hope that we could perform experiments with the atoms trapped in the optical tweezers. However, the atoms have to be strongly confined in the cavity to a position of maximum coupling. Hence, it is necessary to focus the optical tweezers strongly. If a linearly polarized beam is focused to a waist size of the order of the wavelength, the beam diverges strongly near the focus and longitudinal polarization components arise [102,

A



B
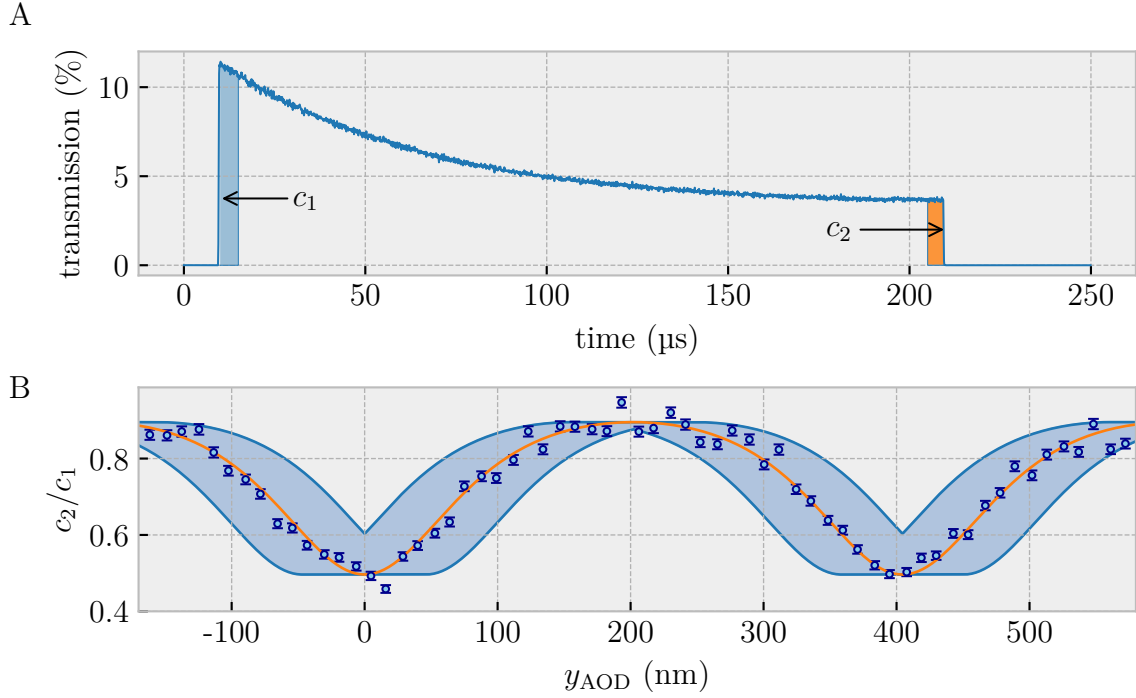
Figure 2.8: **Transmission $T$ through the cavity during optical pumping and modulation of the transmission ratio $c_2/c_1$ along the cavity axis**. **A** By sending $\sigma^+$ light along the cavity axis, the atomic population is optically pumped to the state $|F{=}2, m_F{=}2\rangle$, when the atom is located at a position of maximum cavity field intensity. Therefore, the coupling $g$ increases during the pumping interval and consequently the transmission $T$ through the cavity decreases (see equation (2.4)). The click ratio $c_2/c_1$ is defined as the ratio between the number of detected clicks at the end of the pumping interval $c_2$ (indicated by the orange shaded area) and the number of detected clicks at the beginning of the pumping interval $c_1$ (indicated by the blue shaded area), i. e., $c_2/c_1$. **B** The click ratio $c_2/c_1$ versus the distance $y_{AOD}$. The transmission through the cavity is position- dependent and therefore the pumping ratio is modulated as the atom is moved with the tweezers over the distance $y_{AOD}$. As the optical tweezers do not move parallel to the cavity axis, the periodicity of the modulation of the click ratio is $404(2)\,\text{nm}$ instead of $\lambda_C/2 = 390\,\text{nm}$, as expected. This difference stems from the rotation of the coordinate system of the 2D AOD with respect to the cavity axis. From the fit, we obtain for the rotation an angle of $15(1)°$, which is in good agreement with the $14.60(5)°$ obtained from the frequency-to-position conversion (see Fig. 2.7). For the positioning of the atom with the tweezers we use an error of $\sigma_x = 47(5)\,\text{nm}$ from the frequency-to-position conversion (blue shaded area).

103], resulting in an elliptical polarization. This is problematic as these near-focus extraordinary polarization components induce large virtual magnetic fields, which strongly influence the coherence properties of the qubit. Therefore, many of the groups that are working with optical tweezers, encode their qubit in clock transitions which are insensitive to virtual magnetic fields [104–106]. Unfortunately, this is not possible for the protocol used in chapter 3 to generate the atom-photon entanglement, as we have to use the magnetic field sensitive $|F=1, m_F = \pm 1\rangle$ and $|F=2, m_F = \pm 2\rangle$-states. For that reason, we decided to use the tweezers only for the preparation of the atomic arrays and to then transfer the atoms during the experimental sequence into the 2D optical lattice, as in the 2D lattice the extra-ordinary polarization components are suppressed because of the larger beam waist.

To show the influence of the extra-ordinary polarization components in the tweezers and the suppression of these in the lattice, we measure Raman spectra with the atom in the optical tweezers and in the optical lattice. To measure a Raman spectrum, we initialize the atom in the ground state $|F = 1\rangle$. Then, we switch on the Raman lasers, which transfers the population from $|F = 1\rangle$ to $|F = 2\rangle$ if the two-photon detuning is set correctly. The polarization of the Raman lasers is set such that only transitions from $|F = 1, m_{F_0}\rangle$ to $|F = 2, m_F = m_{F_0} \pm 1\rangle$, i.e. $\Delta m_F = \pm 1$, are allowed. After the Raman transfer to $|F = 2\rangle$, the population in $|F = 2\rangle$ is read out. The probability $P(|F = 2\rangle)$. which is the probability to have transferred the atom to $|F = 2\rangle$ with the Raman, is measured. As we apply a magnetic guiding field, a Zeeman splitting is induced. This splits up the resonance frequencies for transitions between different $m_F$ states from $|F = 1\rangle$ to $|F = 2\rangle$. By scanning the two-photon frequency $\delta$ of the Raman transition and reading out the population in $|F = 2\rangle$, we resolve the different Raman transitions. As the polarization is set such that only $\Delta m_F = \pm 1$ transitions are possible, a spectrum with four peaks is expected, which correspond to the four possible transition frequencies between the individual $m_F$ states [77]. Such a Raman spectrum can be seen in Fig. 2.9 for an atom in the optical lattice in A and for an atom in the optical tweezers in B. The linewidth of the individual transitions is much larger in the optical tweezers. In addition, a fifth peak appears in the spectrum of the atom in the optical tweezers, which is created by driving the transition $|F = 1, m_F = 0\rangle$ to $|F = 2, m_F = 0\rangle$. This transition should not be possible in this polarization configuration of the Raman lasers, but, due to the extraordinary near-focus polarization components of the optical tweezers the effective magnetic field is rotated and therefore additional transition can be driven. The data shown here were measured during Franz von Silva-Tarouca's master's thesis and a more detailed discussion of the topic can be found in [89]. The drastic difference between these two spectra clearly shows the advantages of the optical lattice for experiments with magnetic field sensitive states. For this reason, we decided to transfer the atoms into the optical lattice after the preparation of the atoms.
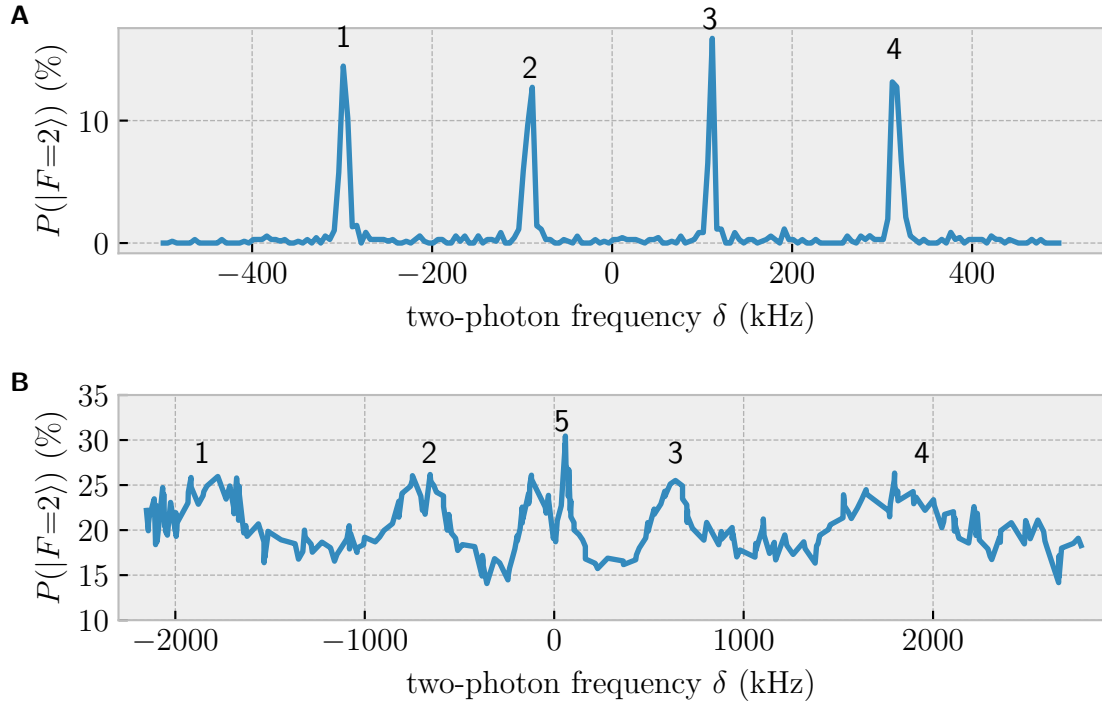
Figure 2.9: **Raman spectra measured with the atom trapped in the two-dimensional optical lattice and in the optical tweezers. A** Spectrum with atom trapped in the optical lattice. In this case, only the expected four transitions are driven by the Raman lasers. **B** Spectrum with atom trapped in optical tweezers. The extraordinary near-focus polarization components in the optical tweezers correspond to a rotation of the effective magnetic field and a fifth transition between $|F = 1, m_F = 0\rangle$ and $|F = 2, m_F = 0\rangle$ (labeled with 5 in the plot) can be driven. The linewidth of the individual transitions is also much larger in the optical tweezers than in the optical lattice, in which the unwanted polarization components are suppressed. The data shown were measured during Franz von Silva-Tarouca's master's thesis [89].

## 2.3 Creating one- and two-dimensional atomic arrays

Before the implementation of the addressing and positioning setup, loading arrays of atoms was a probabilistic process. Even though it was possible to load a large number of atoms into the cavity, the number of atoms and the distance between the atoms was random. For this reason, only experiments with at most two atoms were possible, as the probability to prepare arrays with more than three atoms was already lower than $0.5\,\%$. Fig. 2.10 shows the loading probability for the probabilistic loading scheme without optical tweezers. However, future quantum network nodes, require large arrays of atoms. One of the reasons for building the addressing and positioning setup was that it is supposed to enable the loading of larger arrays.

We tried two approaches to achieve the intended increase in loading efficiency. The first approach was to use the tweezers to move the atoms over the 1064 nm standing wave trap and sort them into the desired arrays shape. However, with this approach, we did not obtain the desired results. We were not able to prepare arrays with more than five atoms because of a too low success probability. The reason for this is that the atoms heat up as they are moved over the 1064 with the tweezers, which leads to atom loss. However, we did not find out the reason for the atom heating. We therefore tried a second approach for the array preparation. In this approach, we load the atoms directly from the MOT into an array of optical tweezers and then sort them within this array into the desired shape. This approach gave us the desired results and allowed us to load up to seven atoms simultaneously. In the following sections, we will describe this loading process. First, we describe the stochastic loading of the optical tweezers and, afterwards, the rearrangement of the atoms within the array. Both steps are shown in Fig. 2.11.

### 2.3.1 Stochastic loading of the static tweezer array

This section describes the first part of the preparation protocol for the atomic arrays, the stochastic loading of the static tweezer array. It is illustrated in Fig. 2.11. The stochastic loading starts with the trapping and cooling of the atoms in a magneto-optical trap (MOT). Details of our MOT can be found in [107]. In a typical cold atom tweezer experiment without a small mode-volume optical cavity, the atoms are loaded into the tweezers directly from the MOT [**liu2023**, 64, 65]. However, in our setup, the cavity together with the piezo-tube in which the cavity is mounted severely restrict the optical access. Therefore, it is impossible to load a MOT directly at the cavity center, where the tweezers are located. For this reason, the MOT is created 14 mm away from the center of the resonator. After the MOT phase, the atoms are transported into the resonator using a running wave dipole trap at 1064 nm. For this purpose, the transport trap is focused exactly between the center of the resonator and the position of the MOT. This focused beam generates a Gaussian potential in which the atoms oscillate. After running through the potential exactly once, the atoms reach the cavity center after 70 ms. In the previously used loading scheme,
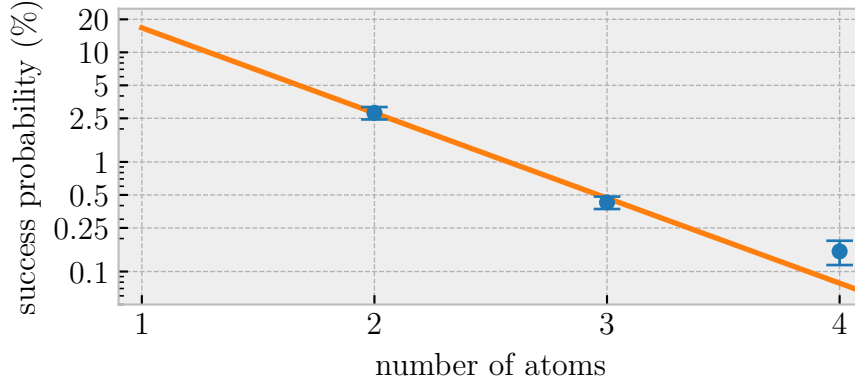
Figure 2.10: **Loading probability for the previously used stochastic loading.** In the stochastic loading scheme, the success probability decays exponentially. For two atoms, the success probability is approximately 2.5 %, and for three atoms, it is already lower than 0.5 %. Due to the low probability to successfully load more than two atoms, experiments with the stochastic loading were limited to at most two atoms.

the atoms were then directly transferred from the transfer trap into the 1064 nm trap. In this case, there is no possibility to control the relative positioning of the atoms. However, in our new tweezer-based loading scheme, the atoms move over the static tweezer array at the cavity center and are trapped stochastically in the individual tweezer using our cooling light, which is switched on during the entire array preparation. Each individual optical tweezer has a trap depth of approximately 1 mK. The trap depth of the individual tweezers varies, because the diffraction efficiency of the AOD is not constant for all deflection angles. The beam waist of the transfer trap at the center of the resonator is approximately $w_0 = 72\,\mu$m [107], within which the atoms can be located. Since this waist is large compared to the spatial extent of the one- or two-dimensional tweezer array (10 μm to 15 μm), the probability of loading atoms directly from the transport trap into the tweezers is rather low. To increase the loading probability of the atoms in static array, we switch on the standing wave trap at 1064 nm for a short amount of time during the transport, in which we keep the atoms trapped during the experimental sequence. This trap has a waist of $\sim 12\,\mu$m. For that reason, the spatial expansion of the atoms is reduced compared to the the expansion in the transport trap, which leads to a significantly higher loading probability of the tweezers. Another important factor for increasing the loading probability is the alignment of the tweezer array with respect to the transfer trap. To increase the loading probability, it is important that one axis of the two-dimensional array is overlapped with the transfer trap. For this reason, we mounted the static tweezers array AOD on a rotation mount and aligned it such that one axis of the static tweezers array and the transfer trap are overlapped, see Fig. 2.12. This way, the static tweezers are loaded stochastically. In Fig. 2.13 we show a typical loading distribution of the number of atoms for a two-dimensional static array.

The average number of atoms loaded is $\overline{n} = 6.4(6)$. This number depends on the number of tweezers in the array and is not constant, but fluctuates over time (time
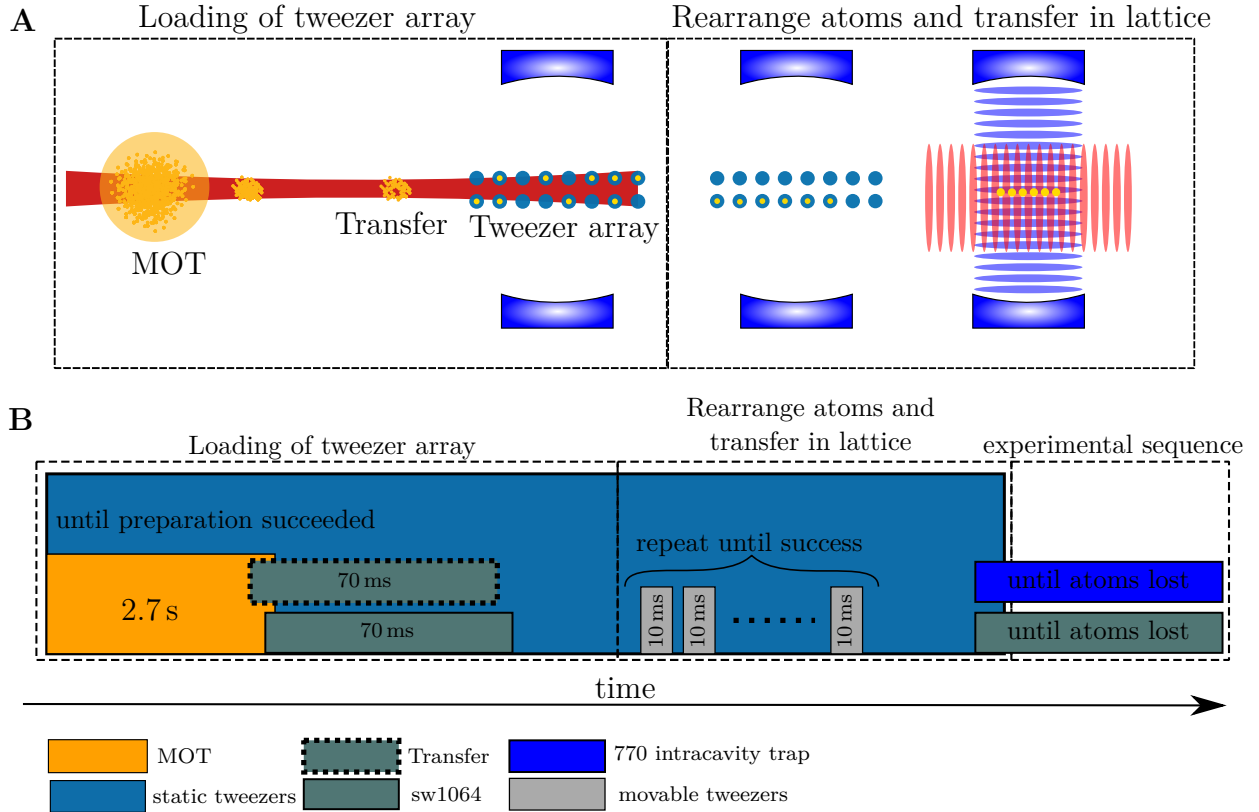
Figure 2.11: **Loading scheme with tweezers including the timing**. **A** Spatial configuration of the MOT, the transfer trap and the optical resonator. The MOT is prepared outside of the cavity and the atoms are transferred into the resonator using a running wave dipole trap at 1064 nm. There, the atoms are moving over the tweezers and are cooled into the static array of the individual tweezers. This way, the static tweezers are stochastically loaded. Based on image evaluation, the initially stochastically loaded atoms are sorted into the desired array configuration in the static tweezers. For the sorting, we use the movable tweezers. If the arrangement is successful, the atoms are transferred into the two-dimensional lattice. The two-dimensional lattice consists of two standing wave traps at 770 nm (along the cavity axis) and 1064 nm (orthogonal to the cavity axis). **B** Timing of the sequence. The entire sequence is divided into three major steps: the loading of the static tweezer array, the rearrangement of the atoms and the transfer of the atoms into the two-dimensional lattice. The actual experimental science sequence is described in more detail in chapter 3.
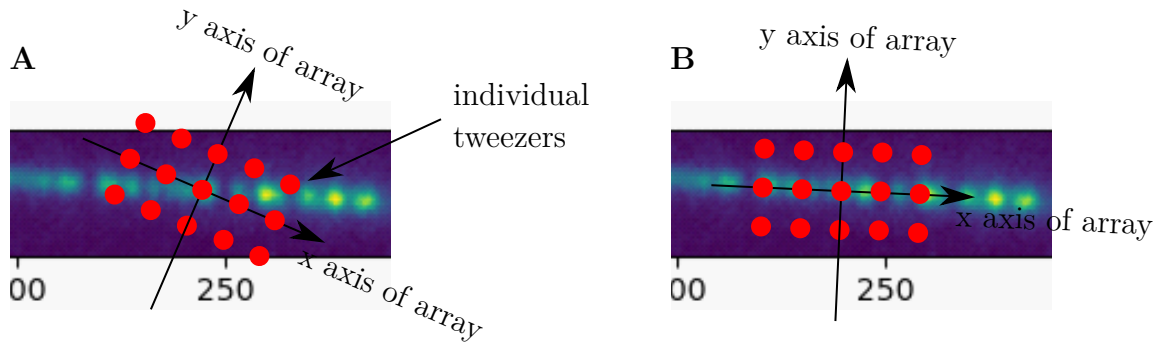
Figure 2.12: **Rotation of static tweezers Array vs. transfer trap**. **A** Tweezer array is rotated relative to the transfer trap, which leads to a reduced average number of loaded atoms. To increase this loading average , the spatial overlap of the static tweezer array with the transfer trap (indicated by the yellow line consisting of atoms) has to be maximized. **B** Transfer trap and the tweezer array overlap. Therefore, the loading probability is increased.
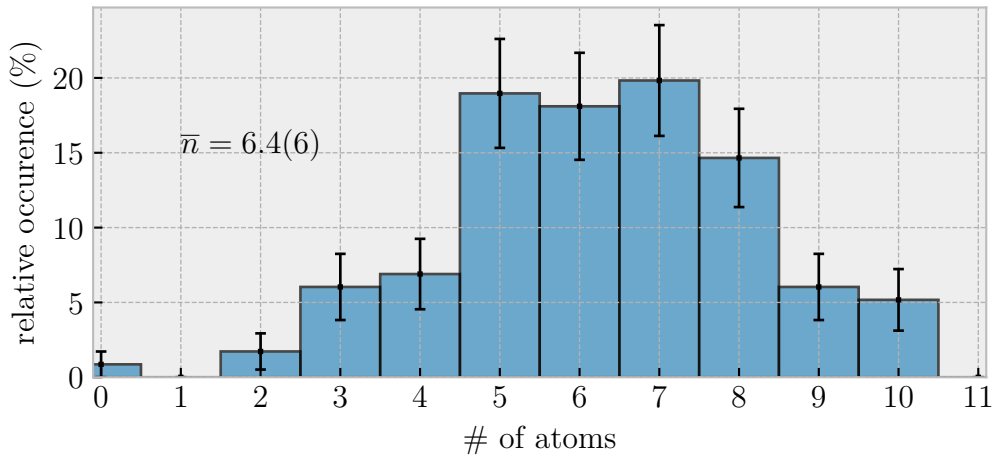


Figure 2.13: **Loading statistics for a two-dimensional tweezer array.** The loading into the static tweezers from the transfer trap is a stochastic process, which is described by a Poissonian distribution for the number of atoms. In the shown example, the average number of loaded atoms is $\overline{n} = 6.4(6)$.
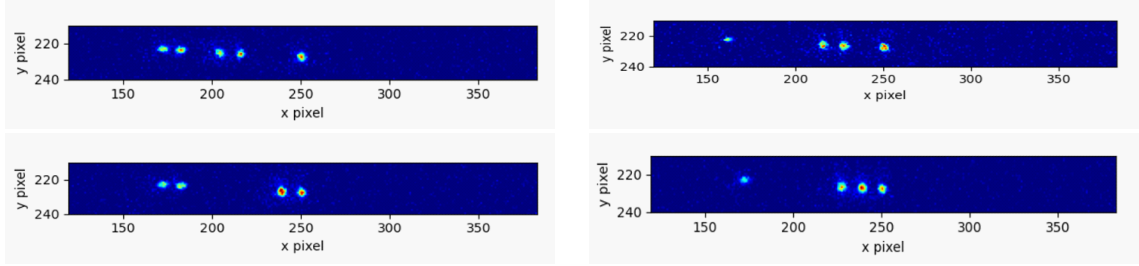
Figure 2.14: **Images of stochastically loaded one-dimensional tweezer arrays**. After the MOT phase, the atoms are transported to the center of the cavity in the running wave transfer trap. There, they move over the static tweezer array and are trapped in the tweezers using our cooling light. Since this is a stochastic loading process, the number of atoms that are trapped as well as which tweezers are filled is different for each loading process, as shown in the different images.

scale of days to weeks), because of several reasons, e.g., the drift in the spatial overlap between the transfer trap and the MOT. The result shown in 2.13 is therefore only an example, but typically we achieve loading numbers $\overline{n} > 5.5$. The distance between neighboring tweezers in the static tweezers array is in the range of 5 µm to 10 µm. At smaller distances, the neighboring tweezers start to interfere with each other and the average number of loaded atoms decreases. At the same time, the number of tweezers that can be generated, when the distance between neighboring tweezers is large, is much lower. This is because the efficiency of the AOD is maximum at the center frequency and drops for frequencies that are further away from the center frequency. When using small distances between neighboring optical tweezers, many tweezers are generated in a frequency range close to the center frequency. However, when using larger distances between neighboring tweezers, many tweezers are generated at frequencies with a small efficiency and the number of tweezers is therefore limited by the optical laser power. In Fig. 2.14 we show typical arrangements after loading atoms in the individual tweezers for a one-dimensional static array. The number and the positions of the atoms change for every loading attempt. To create one- and two-dimensional ordered arrays with a precise number of atoms, we implemented an atom sorting procedure, which we describe in the next section.

## 2.3.2 Rearranging the atoms

Rearranging the atoms is the second step in the whole process of the array preparation, shown in Fig. 2.11. To rearrange the atoms, we use both two-dimensional AODs of our setup (see section 2.1). We use the static AOD to create the array in which the atoms are initially trapped after the loading and we use second AOD to create the movable optical tweezers. The movable tweezers are used to move atoms between the individual optical tweezers of the static array. This principle is illustrated in Fig. 2.15. The rearrangement of the atoms starts after the stochastic loading of the static tweezers. First, an image is taken to analyze which tweezers are filled and which atoms need to be moved to achieve the desired array configuration. To move an atom, we superimpose the movable tweezers with the single static

tweezers from which we want to remove the atom. We then linearly ramp up the power of the movable tweezers within 10 ms, such that $U_{mov} \approx 3U_{static}$, and cool the atom in the movable tweezers. Then, the atoms are moved to the target tweezers at a speed of $v_{mov} \approx 5 \frac{\mu m}{ms}$ along the shortest possible way, but in a manner that they never move over the other static tweezers. The atoms are then reloaded back into the target tweezer. To do this, the two tweezers are again superimposed and the potential of the static tweezers is linearly ramped down to $U_{mov} = 0$. Multiple atoms can be moved within the time that we need to take one picture (300 ms). The next picture is then used to check if the movement attempt was successful. If a movement attempt failed, but there are still enough atoms trapped in the static tweezers array, the rearrangement process is repeated. The arrangement of the atoms takes 1 s to 2 s, because the atoms are arranged sequentially. The rearrangement protocol is optimized such that the distance over which the atoms are moved and the number of movements are minimized. However, moving the atoms does not work perfectly. The probability with which the movement of an atom works depends on several factors, like the moving speed $v_{mov}$, the trap depth of the movable tweezers $U_{mov}$, the the cooling parameters, the timing of reloading between static and movable tweezers and the distance over which the atom must be moved. We have scanned these parameters and maximized the movement success probability to be approximately 90 % per atom per move, depending on the distance. In Fig. 2.16, we show our final results for sorting the atoms. In both A and B, we show histograms of the loading statistics before and after the rearrangement of the atoms. A shows the statistics for a target array consisting of $n = 2$ and B the statistics for $n = 3$ atoms. In both cases the final distributions have a large peak at the target number of atoms and a success probability of over 80 % is achieved. This means that we successfully generate the desired atom array in the static tweezers in more than 80 % of the loading processes, i.e., per MOT. The statistics shown do not yet include the transfer of the atoms into the 1064 nm standing wave trap from the tweezers, but the probability of this transfer is close to 100 %.

### 2.3.3 Results of the array preparation

Fig. 2.17 A shows the success probability for the different methods we investigated. The success probability $P_{\mathrm{T}}$ with the optical tweezers beats the old probabilistic method $P_T$ by several orders of magnitude. With the old, probabilistic method we were limited to experiments with at most two atoms, but now protocols with up to seven atoms are possible. The maximum number of atoms is mostly limited by the initial number of atoms loaded into the static array. It is usually about $\overline{n} \approx 6$, see Fig. 2.13. This means that there are only a few events where the number of initially loaded atoms is high enough to start the rearrangement process at all. In addition, the storage time $T$ of 15 s to 30 s, which scales for $n$ atoms as $\sim \frac{T}{n}$, limits the number of movement attempts that we can perform. Besides the array preparation with the tweezers, we added the success probability $P_{\mathrm{over1064}}$ for moving the atoms over the 1064 nm. This method already works better than probabilistic loading, but is much worse than preparing the arrays using only the optical tweezers. Nevertheless, both methods significantly increase the rate at which atomic arrays
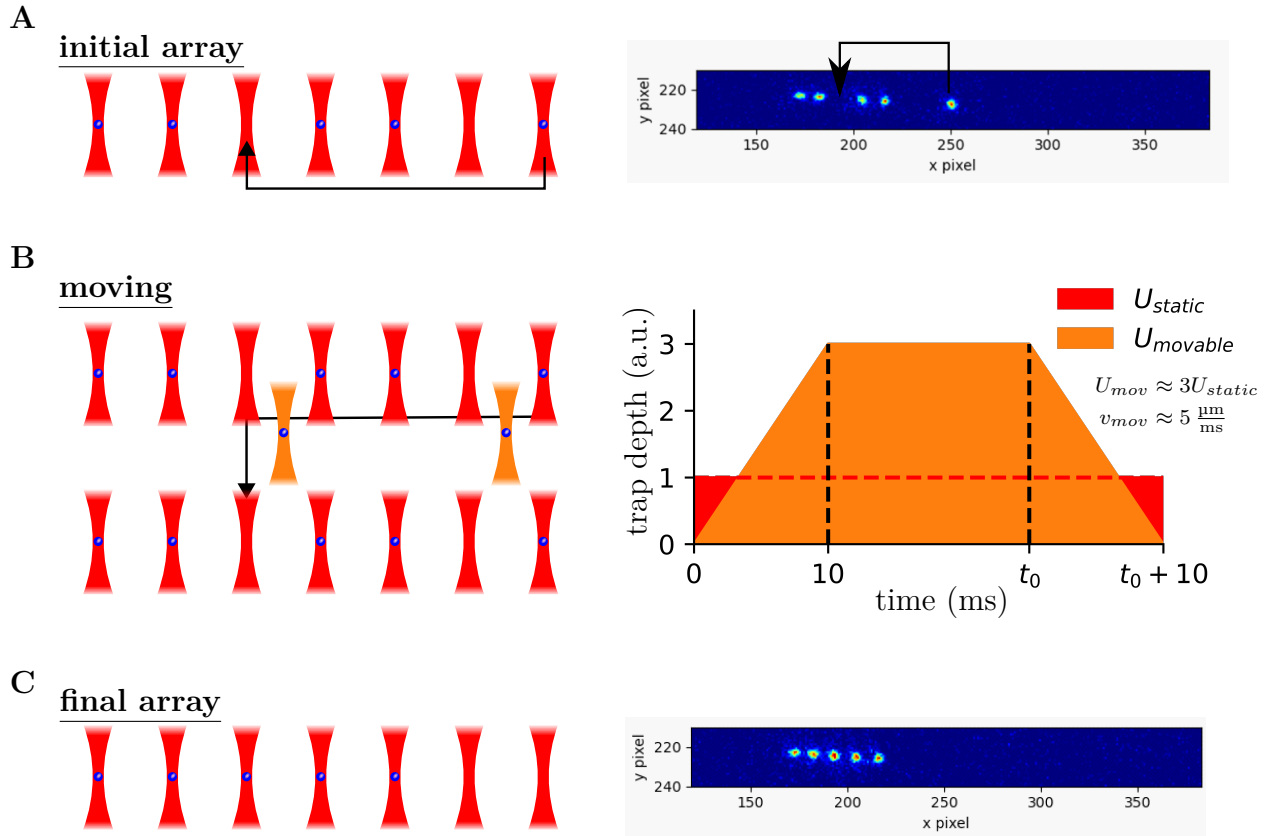
Figure 2.15: **Rearrangement protocol. A** Stochastically loaded array after MOT transfer. The image is analyzed with the self-written LabView software and the necessary steps for the rearrangement of the atoms are calculated. **B** Rearrangement of the atoms. The movable tweezer is used to rearrange the atoms into the desired configuration. For the transfer from the static to the movable tweezers, the trap depth of the movable tweezers is ramped up linearly to about three times the depth of the static tweezers. The moving speed $v_{mov}$ is about $5\,\frac{\mu m}{ms}$. Steps A and B are repeated until the desired configuration is reached, see **C**.
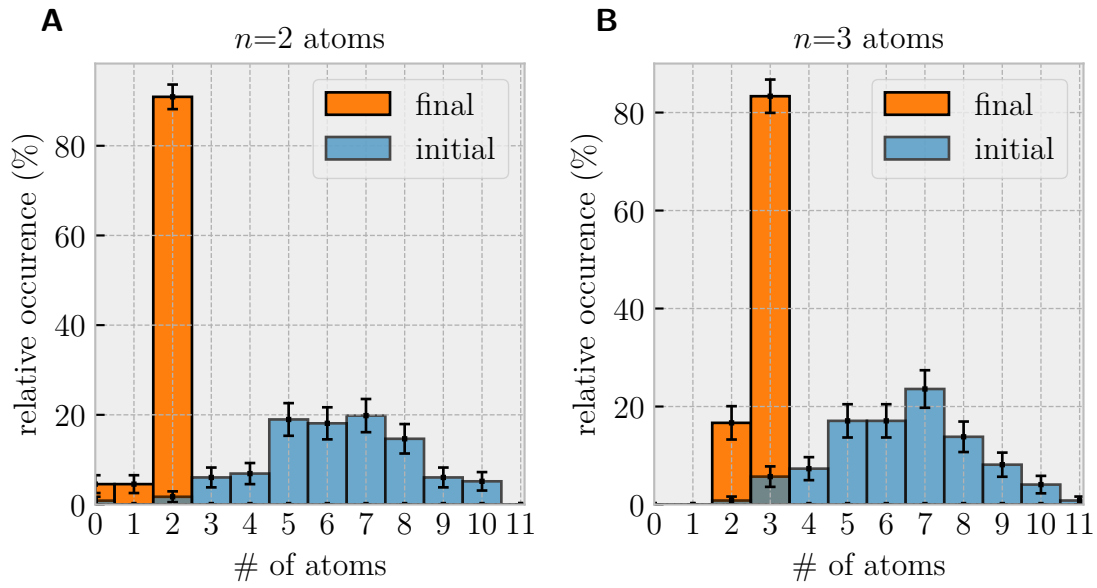
Figure 2.16: **Comparison of the atom number distributions before and after the rearrangement with the movable tweezers.** The initial and final atom number distributions are shown for a target array size of $n = 2$ (**A**) and of $n = 3$ (**B**) atoms. The initial, Poissonian distributions have an average atom number of approximately $\bar{n} = 6$ atoms and are then transformed into a distribution with a clear peak at the desired atom number. In both cases, the maximum probability is higher than $80\,\%$. The atoms are rearranged into the desired shape within the static tweezers by moving the atoms with the movable tweezers and removing unneeded atoms, if necessary.

can be prepared. This is shown in part B of Fig. 2.17, where we plot the ratios $P_T/P_P$ and $P_{\text{over1064}}/P_P$ of the success probabilities for different numbers of atoms for the different methods. To get an estimate of the success probabilities for arrays with more than five atoms, we extrapolated the success probabilities using the fitting parameters obtained from the fits for up to four and five atoms. We extrapolate an increase in the ratio $P_{\text{over1064}}/P_P$ by a factor of $1 \times 10^2$ when moving the atoms over the 1064 nm trap. For the preparation with the tweezers, we extrapolate a factor larger than $1 \times 10^4$ for the ratio $P_T/P_P$. This increase in the success probability by four orders of magnitudes suggests that the preparation of larger arrays is likely in the future, especially, since the maximum number of atoms is mostly limited by the average number of atoms initially loaded in the stochastic array and the movement of the atoms, both of which can still be improved.
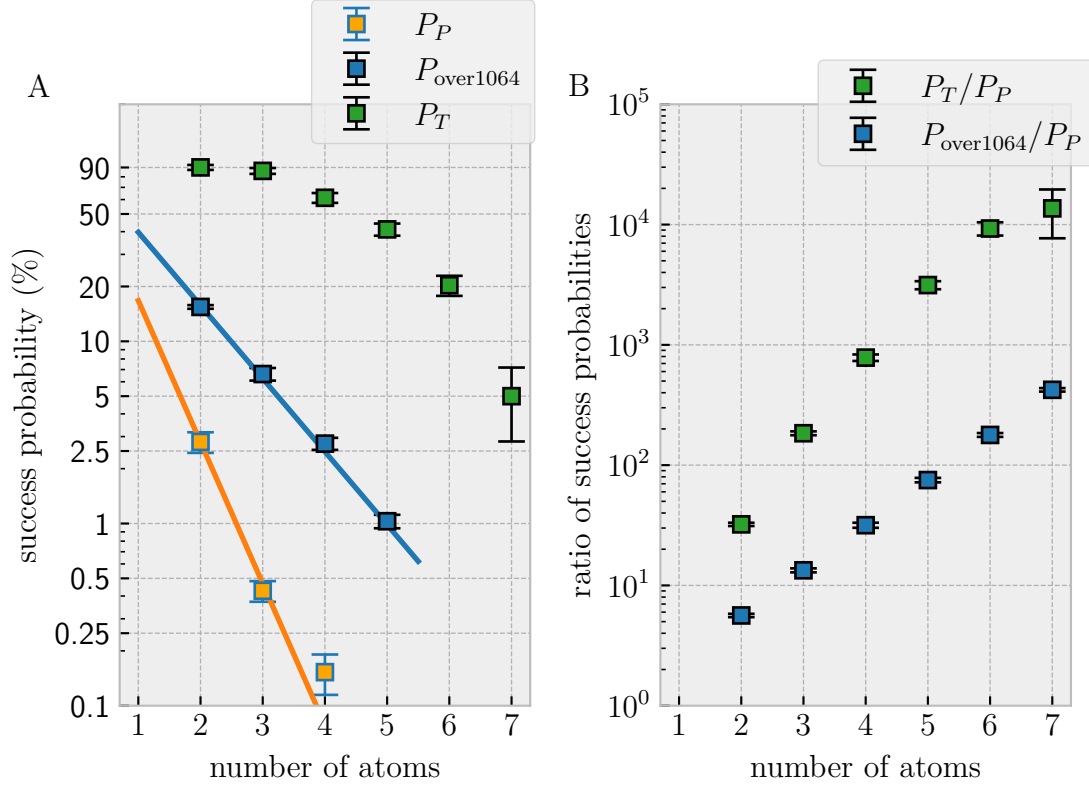
Figure 2.17: **Success probabilities for different loading schemes and ratio of loading rates versus number of atoms**. **A** Success probability of array preparation versus number of atoms for different preparation schemes. The previously used probabilistic loading scheme (orange markers) gives the worst results and at most two atoms can be prepared. Moving the atoms with the tweezers over the 1064 nm trap (blue markers) increases the maximum number of atoms to five. However, the success probabilities are still lower than for the preparation with the tweezer arrays (green markers). The tweezer arrays allow to prepare up to seven atoms with a probability of more than 10 %, which is higher than the probability for two atoms in the probabilistic case. **B** Ratio of the success probabilities for the different loading methods. $P_{\text{over1064}}/P_P$ and $P_T/P_P$ show the effect of the tweezers on the success probabilities of the array preparation. The rates are increased by a factor of $1 \times 10^2$ ($P_{\text{over1064}}/P_P$) and $1 \times 10^4$ ($P_T/P_P$). The factors are estimated by extrapolating the success probabilities $P_{\text{over1064}}$ and $P_P$.

# Chapter 3

# A multi-qubit register

In this chapter, I describe the experimental implementation of a quantum network register. I start by describing how we entangle the internal atomic state of a single atom from an atomic array with the polarization of a photon. We start by explaining the basic steps of the entanglement generation process with the experimental protocol for a single atom (see Section 3.1). Then, in section 3.2, we extend the protocol to multiple atoms in one and two dimensional arrays and show how multiplexing can increase the efficiency and rate of atom-photon entanglement (APE) generation. Afterwards, I discuss the experimental imperfections in section 3.3 and give a short outlook on the necessary improvements required to scale up the register to larger qubit numbers, see section 3.4. The results presented in this chapter are published in [108].

## 3.1 Atom-Photon Entanglement with a single atom

In this section, I describe the protocol to entangle the internal state of a single atom and the polarization of the generated photon. The resulting entangled state will be the Bell state $|\Psi^+\rangle$. The experimental sequence used to generate this entangled state is displayed in Fig. 3.1. Each step of the sequence is explained in detail in the following individual subsections. The most important steps are the atom initialization in the state $|F{=}2, m_F{=}0\rangle$ through optical pumping (part A in Fig. 3.1, see subsection 3.1.1), the atom-photon entanglement generation using a vSTIRAP (part B, see subsection 3.1.2) and the photonic and atomic state readout (see subsection 3.1.4). The atomic and photonic state readout is a multi-step process (parts C-F). We use two metrics, the efficiency $\eta$ and the fidelity $\mathcal{F}$, to evaluate the generated entangled state. Therefore, I also discuss the photon generation efficiency and its limiting factors (see section 3.1.3) as well as at how to determine the fidelity between the generated state $\rho$ and the state $|\Psi^+\rangle$ (see subsection 3.1.5).

### 3.1.1 Optical pumping into $|F{=}2, m_F{=}0\rangle$

At the beginning of the sequence, the atom is initialized in the state $|F{=}2, m_F{=}0\rangle :=
|0\rangle$, as shown in part A of Fig 3.1. To do this, we use $\pi$-polarized light resonant with the $|5^2S_{1/2}, F{=}2\rangle \rightarrow |5^2P_{1/2}, F{=}2\rangle$ transition and a repumper resonant
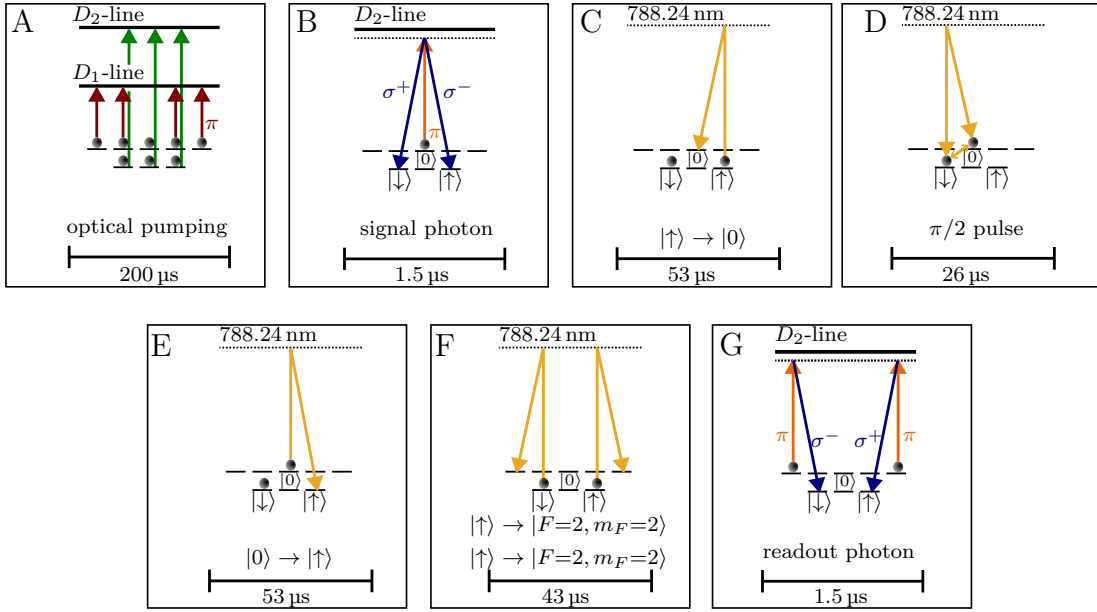
Figure 3.1: **Experimental sequence for the generation and characterization of atom-photon entanglement (APE) with a single atom**. The atom is initialized in $|F{=}2, m_F{=}0\rangle$ with optical pumping at the beginning of the sequence (part A). Afterwards, a vSTIRAP is used to generate APE between the polarization of the emitted photon and the internal atomic state (part B). To determine the fidelity, we then read out the internal atomic state in a multi-step process. In this process, the atomic state is mapped to a readout photon by single qubit rotations (parts C-E ), an atomic state transfer (part F) and a second vSTIRAP (part G).

with the transition $|5^2S_{1/2}, F{=}1\rangle \rightarrow |5^2P_{3/2}, F{=}2\rangle$. Both beams propagate along the same axis as the 1064 nm standing wave trap (see Fig. 1.5). The underlying idea for the optical pumping is to use that the transition $|5^2S_{1/2}, F{=}2, m_F{=}0\rangle \rightarrow |5^2P_{1/2}, F{=}2, m_F{=}0\rangle$ is dipole-forbidden. Therefore, the population in the state $|0\rangle$ is not excited when using $\pi$-light. However, the population in all other magnetic sublevels of $|F{=}2\rangle$ of the hyperfine ground state can be excited by the $\pi$-light. If the atom is excited with $\pi$ light, the $m_F$ state does not change during the excitation. However, in the subsequent decay, the $m_F$ state can change. This leads to the accumulation of the population in the $|F{=}2, m_F{=}0\rangle$ state during the pumping process. If during the pumping process the atomic state decays to $|F{=}1\rangle$, the repumper brings the population back into $|F{=}2\rangle$ via the excitation to the $|F'{=}2\rangle$ level. For the pumping, the $D_1$ line is used, as the splitting between the hyperfine states $|F{=}1\rangle$ and $|F{=}2\rangle$ of the $|5^2P_{1/2}\rangle$ fine structure state is larger (816 MHz) than the hyperfine splittings of the $|5^2P_{3/2}\rangle$ fine structure state (267 MHz between $|F'{=}2\rangle$ and $|F'{=}3\rangle$ and 157 MHz between $|F'{=}2\rangle$ and $|F'{=}1\rangle$), which suppresses unwanted scattering. At the end of the pumping process, we switch off the repumper for a short amount of time, typically 3 µs to 5 µs, and keep only the $\pi$-polarized pump light on. This empties all the magnetic sublevels $|F = 2, m_F \neq 0\rangle$ and therefore no photon is emitted during the subsequent vSTIRAP pulse. Switching off the repumper only reduces the efficiency of the generation process, but not the fidelity. This way, we can initialize the atom in the desired state. To determine the pumping efficiency, we compare the two efficiencies $P_{|F=2\rangle}$ and $P_{|F=2,m_F=0\rangle}$ of the photon generation process. $P_{|F=2\rangle}$ is the efficiency to generate a photon after initializing the atom in $|F{=}2\rangle$ when we only use the repumper. $P_{|F=2,m_F=0\rangle}$ is the efficiency to generate a photon after pumping into $|F{=}2, m_F{=}0\rangle$. The ratio $P_{|F=2,m_F=0\rangle}/P_{|F=2\rangle}$ gives the efficiency of the pumping process. In our case, the efficiency of the entire pumping process is 80(5) %. The limit for the efficiency of this pumping process is, unfortunately, not known. A lower limit for the pumping fidelity can be obtained by looking at the correlations in $ZZ$ detection basis (see section 3.1.5) and is 98 %. With our beam configuration (see section 1.3), multiple atoms can be initialized simultaneously, as the beams for the optical pumping have a beam waist of approximately 35 µm and therefore all atoms in the cavity are homogeneously illuminated.

## 3.1.2  vSTIRAP & Atom-photon Entanglement

The basic principle to generate atom-photon entanglement has already been explained in section 1.6. The level structure with the relevant levels and detunings is displayed again in Fig. 3.3. After the initial optical pumping into $|F{=}2, m_F{=}0\rangle$ (see section 3.1.1), we address the atom with $\pi$-polarized light with the addressing system and generate a photon using a vSTIRAP pulse. This process transfers the atom into one of the two states $|F{=}1, m_F{=} \pm 1\rangle$. The polarization of the generated photon, called the signal photon, depends on the state in which the atom is after the photon emission. If the atom is in the state $|\downarrow\rangle := |F{=}1, m_F{=}{-}1\rangle$, the photon is $\sigma^+$-polarized and if the atom ends up in the state $|\uparrow\rangle := |F{=}1, m_F{=}1\rangle$, the photon
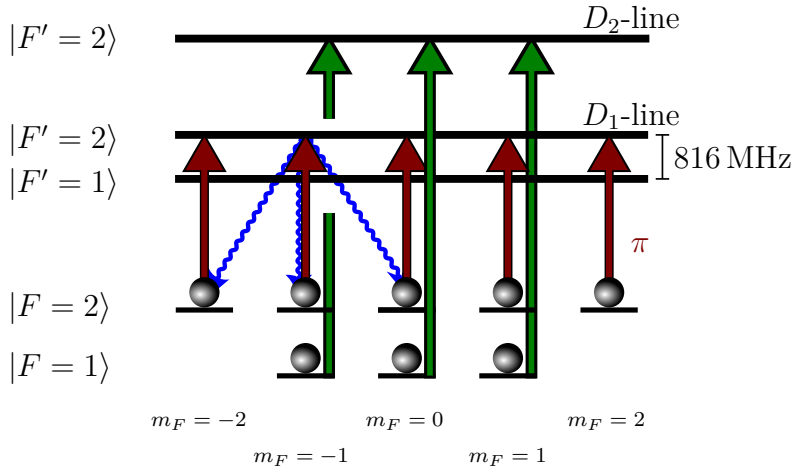
Figure 3.2: **Optical pumping into** $|F=2, m_F=0\rangle := |0\rangle$. To initialize the atom in $|0\rangle$, we send $\pi$-polarized light that is resonant with the transition $|F=2\rangle \rightarrow$ $|5^2P_{1/2}, F=2\rangle$ and a repumper resonant with $|F=2\rangle \rightarrow |5^2P_{3/2}, F'=2\rangle$ transition. Due to angular momentum selection rules, the excitation from $|F=2, m_F=0\rangle$ with $\pi$-polarized light is forbidden. However, population from all the other magnetic sublevels of $|F=2\rangle$ can be excited. The excitation with $\pi$-light does not change the $m_F$ state, but during the subsequent decay the magnetic sublevel can change (indicated by the blue wavy lines). This way, the population accumulates in $|0\rangle$ during the optical pumping interval. If the population decays to $|F=1\rangle$, the repumper transfers the population back from $|F=1\rangle$ to $|F=2\rangle$ by excitation to the $|F'=2\rangle$ state. At the end of the pumping sequence, the repumper is switched off. This removes the remaining population in $|F=2\rangle$ and only reduces the efficiency of the photon generation process, but not the fidelity.

is $\sigma^-$-polarized. Hence, we generate the state

$$|\Psi^+\rangle = \frac{1}{\sqrt{2}} \left( |\sigma^+, \downarrow\rangle + |\sigma^-, \uparrow\rangle \right). \tag{3.1}$$

The fidelity between the generated state $\rho$ and $|\Psi^+\rangle$ for a single atom is $\mathcal{F} = 86.6(5)\,\%$ and the generation-to-detection efficiency is $\eta_{overall} = 33.2(3)\,\%$ (see section 3.1.3). These results were obtained with a single-photon detuning $\Delta$ of $2\pi \times 200\,\text{MHz}$ with respect to the states $|F'{=}1, m_F{=}\pm 1\rangle$, as in [109]. The choice of this detuning $\Delta$ is relevant when working with multiple atoms, as it affects the fidelity of the generated state with the Bell state $|\Psi^+\rangle$ as well as the photon generation efficiency. This is because in the case of multiple atoms, previously addressed atoms are in the state $|F{=}1\rangle$ and a photon emitted in the cavity mode may be scattered off these atoms. Therefore, the detuning $\Delta$ must be chosen sufficiently large such that the unwanted scattering is suppressed, since the scattering rate scales as $g^2/\Delta$. However, if the detuning is too large, the fidelity decreases. This is because besides the transition $|F{=}2, m_F{=}0\rangle \to |F'{=}1, m_F{=}0\rangle$, the transition $|F{=}2, m_F{=}0\rangle \to |F'{=}3, m_F{=}0\rangle$ is dipole-allowed, too (the transitions $|F{=}2, m_F{=}0\rangle \to |F'{=}0, m_F{=}0\rangle$ and $|F{=}2, m_F{=}0\rangle \to |F'{=}2, m_F{=}0\rangle$ are dipole-forbidden). However, the excitation to $|F'{=}3, m_F{=}0\rangle$ is unwanted, because after a subsequent decay to $|F{=}2\rangle$, the atom may be excited again from a different state than $|F{=}2, m_F{=}0\rangle$, which would lead to a reduction of the fidelity. To suppress this excitation, the detuning $\Delta$ has to be small compared to the hyperfine splitting between $|F'{=}1\rangle$ and $|F'{=}3\rangle$. Therefore, the single-photon detuning has to be set as large as possible, but still be small compared to the hyperfine splitting between $|F'{=}1\rangle$ and $|F'{=}3\rangle$. This considerations led to the choice of $\Delta = 2\pi \times 200\,\text{MHz}$ with respect to the states $|F'{=}1, m_F{=}\pm 1\rangle$. The exact procedure for measuring the fidelity is described in section 3.1.5. Throughout the entire experimental sequence, the atom is trapped in the two dimensional optical lattice, since the coherence time of the atomic qubit is significantly longer in the lattice than in the optical tweezers. The optical lattice consists of the 1064 nm standing wave trap and the 770 nm standing wave trap. The influence of the blue-detuned 770 nm trap on $g$ as well as the factors influencing the efficiency of the photon generation process are described in section 3.2.2.

### 3.1.3 Efficiency to generate and detect a single photon

In the following sections, three different definitions for the entanglement generation efficiency are used: The generation-to-detection efficiency $\eta_{overall}$, the in-fiber detection efficiency $\eta_{fiber}$, and the intrinsic generation efficiency $P$. The intrinsic generation efficiency is the efficiency to produce a photon at the output port of the cavity. The in-fiber efficiency $\eta_{fiber}$ is the product of the intrinsic efficiency $P$, the optical pumping efficiency $(80(5)\,\%)$ of the atom in $|F{=}2, m_F{=}0\rangle$, and the fiber-coupling efficiency into the first fiber behind the cavity $(92(3)\,\%)$, see Fig. 3.4. The generation-to-detection efficiency is includes the overall transmission and detection efficiency of the superconducting nanowire single photon detectors, i.e. the total transmission, the detection efficiency and the optical pumping efficiency are
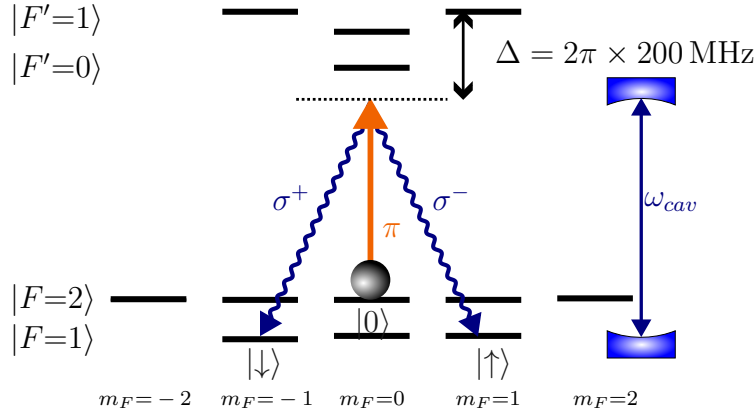
Figure 3.3: **Configuration of cavity and vSTIRAP scheme for photon generation**. The cavity is detuned by $\Delta$ from the transition $|F{=}1, m_F{=}0\rangle \rightarrow |F'{=}1, m_F{=}1\rangle$. The control light addresses the transition $|F{=}2, m_F{=}0\rangle \rightarrow |F'{=}1, m_F{=}1\rangle$ with the same detuning $\Delta$. Therefore, the transition is on two-photon resonance and both light fields together drive the atomic population from the state $|F{=}2, m_F{=}0\rangle$ to the states $|F{=}1, m_F{=}\pm 1\rangle$. The single-photon detuning $\Delta$ is set to $2\pi \times 200\,\text{MHz}$ to suppress unwanted scattering of the generated photons off atoms that were not addressed, as in [109].

included. Therefore, $\eta_{overall} = P\xi$, where $\xi$ is the product of the optical pumping efficiency and the total propagation efficiency of the setup, as well as the detector efficiencies. The intrinsic photon generation efficiency $P$ is given by [110, 111]

$$P = \frac{\kappa_{out}}{\kappa} \frac{2C}{2C + 1}, \tag{3.2}$$

where $\kappa_{out}$ is the field decay rate through the outcoupling mirror, $\kappa$ the total field decay rate of the cavity, and $C$ the cooperativity, defined as $C = g^2/(2\kappa\gamma)$. For the transition used in this protocol, we obtain $g = 2\pi \times 5\,\text{MHz}$. Therefore, the cooperativity is $C = 1.66$, which gives an intrinsic efficiency of $P = 70\,\%$ $((\kappa, \kappa_{out}) = 2\pi \times (2.5, 2.3)\,\text{MHz})$. To obtain the final generation-to-detection efficiency $\eta_{overall}$, all the optical losses and the detection efficiency have to be included. Fig. 3.4 shows the optical path behind the cavity and the detection setup with the most important optical components. After a photon has exited the cavity, it is coupled into an optical fiber that brings it to the detection setup. To optimize the fiber coupling, a pair of lenses is installed in front of each fiber. The detection setup consists of waveplates for setting the polarization correctly, an electro-optic modulator (EOM) for fast switching of the detection basis (see section 3.1.4), and a PBS. The output ports of the PBS lead via an optical fiber to highly efficient superconducting nanowire single photon detectors (SNSPD). Since the efficiency of the SNSPDs depends on the polarization, waveplates are installed in front of each fiber (not shown) to maximize the detection efficiency. The optical pumping efficiency, the optical losses of all the individual components and the detector efficiencies together are $\xi = 51(6)\,\%$, which gives a generation-to-detection efficiency of $\eta_{overall} = 36(4)\,\%$ for a single atom. In the experiment, we measure an efficiency of $\eta_{overall} = 33.2(3)\,\%$, which agrees well
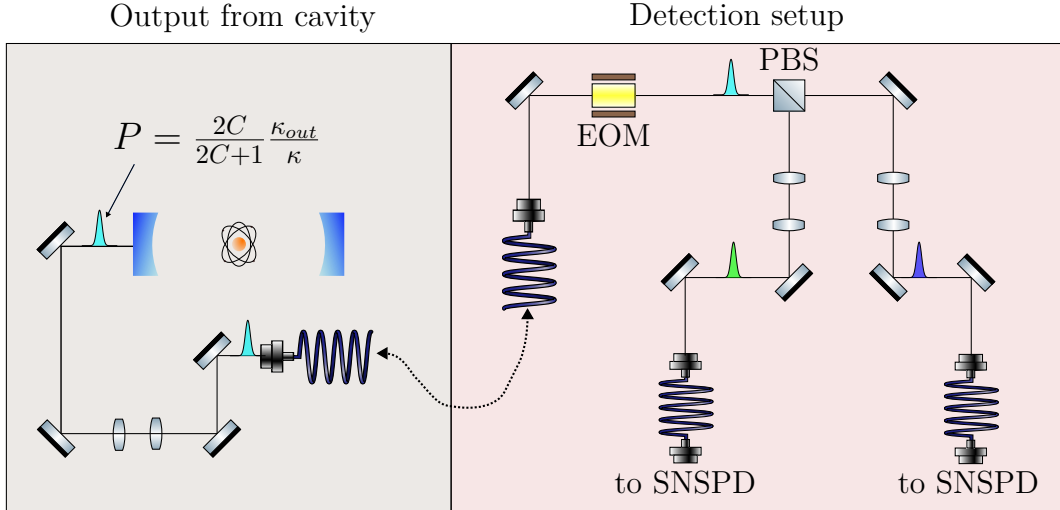
Figure 3.4: **Optical beam path from cavity to detectors.** After exiting the cavity, the photons are coupled into an optical fiber that leads to the polarization-resolving detection setup. The polarization basis of the detection setup is set with a combination of waveplates (not shown) and a polarizing beam splitter (PBS). The PBS deflects orthogonal polarizations (indicated by the different colors of the propagating pulses) into different output ports. The output ports are connected to the superconducting nanowire single photon detectors (SNSPDs). The electro-optical modulator (EOM) allows for fast switching between the $XX$ and $YY$ bases. The overall propagation and detection efficiency is $64(6)\,\%$.

with the values obtained from measuring the losses. From this, we calculate an in-fiber efficiency of $\eta_{fiber} = 48(5)\,\%$.

### 3.1.4 Raman pulses & State readout

To determine the fidelity (see section 3.1.5) of the generated state $\rho$ with the Bell state $|\Psi^+\rangle$, we measure the correlations between the polarization of the photonic qubit (signal photon) and the internal atomic state in three different bases, namely $XX = X_a \otimes X_p$, $YY = Y_a \otimes Y_p$ and $ZZ = Z_a \otimes Z_p$. The definitions of the different bases are in Table 3.1. The photonic qubit is measured with our polarization-resolving detection setup (see Fig. 3.4). However, reading out the atomic qubit is not as simple. To readout the atomic qubit, the qubit is mapped on the polarization of a second photon, called the readout photon. This polarization is then measured again with our detection setup. The final measured correlations are therefore correlations between the polarization of the signal photon and the polarization of the readout photon. For the mapping of the atomic qubit to the readout photon, multiple Raman rotations of the atomic qubit are required. In this section, these rotations are discussed. The basic principle of Raman transitions in our experiment is already explained in section 1.5.

The total scheme of the readout, including the final readout photon, is shown in Fig. 3.5. The atomic readout sequence starts after the detection of the signal pho-

| Atomic bases | Photonic bases |
|---|---|
| $Z_a = \{\ket{\uparrow}, \ket{\downarrow}\}$ | $Z_p = \{\ket{R} := \ket{\sigma^+}, \ket{L} := \ket{\sigma^-}\}$ |
| $Y_a = \{\ket{\uparrow_y} = \frac{1}{\sqrt{2}}(\ket{\uparrow} + i\ket{\downarrow}),$ $\ket{\downarrow_y} = \frac{1}{\sqrt{2}}(\ket{\uparrow} - i\ket{\downarrow})\}$ | $Y_p = \{\ket{A} = \frac{1}{\sqrt{2}}(\ket{R} + i\ket{L}),$ $\ket{D} = \frac{1}{\sqrt{2}}(\ket{R} - i\ket{L})\}$ |
| $X_a = \{\ket{\uparrow_x} = \frac{1}{\sqrt{2}}(\ket{\uparrow} + \ket{\downarrow}),$ $\ket{\downarrow_x} = \frac{1}{\sqrt{2}}(\ket{\uparrow} - \ket{\downarrow})\}$ | $X_p = \{\ket{H} = \frac{1}{\sqrt{2}}(\ket{R} + \ket{L}),$ $\ket{V} = \frac{1}{\sqrt{2}}(\ket{R} - \ket{L})\}$ |

Table 3.1: **Definition of the atomic and photonic bases.** The table displays the definitions used in equations (3.8) and (3.9).

ton. This detection projects the atomic qubit on an eigenstate of the corresponding measurement basis, e.g. in the $ZZ$ basis the atomic qubit is projected either on $\ket{\uparrow}$ or $\ket{\downarrow}$. These two basis states can be read out by transferring the population from the state $\ket{\uparrow}$ to $\ket{F=2, m_F=2}$ and the state $\ket{\downarrow}$ to $\ket{F=2, m_F=-2}$ with a Raman transfer and the generation of a photon afterwards with a vSTIRAP (parts F and G in Fig. 3.5). The polarization of the generated photon is $\ket{\sigma^-}$, if the internal atomic state is $\ket{\uparrow}$ and $\ket{\sigma^+}$ if, the internal atomic state is $\ket{\downarrow}$. This way, we can unambiguously assign the basis states of $Z_a$ to the polarization of the generated photon and read out the atomic state. For the measurement in $X_a$ ($Y_a$), the atom is projected after the detection of the signal photon either on $\ket{\uparrow_x}$ ($\ket{\uparrow_y}$) or on $\ket{\downarrow_x}$ ($\ket{\downarrow_y}$). These basis states are superposition states of the basis states of $Z_a$. In order to be able to use the same readout protocol as in the $Z_a$ basis, we must first perform a $\pi/2$ pulse to map the basis states of $X_a$ and $Y_a$ to the basis states of $Z_a$, i.e. to map the states $\ket{\uparrow_x}$ and $\ket{\uparrow_y}$ to $\ket{\uparrow}$ and the states $\ket{\downarrow_x}$ and $\ket{\downarrow_y}$ to $\ket{\downarrow}$. This mapping corresponds to a $\pi/2$ pulse (with different phases for the $XX$ and $YY$ basis) between the states $\ket{F=1, m_F=1}$ ($\ket{\uparrow}$) and $\ket{F=1, m_F=1}$ ($\ket{\downarrow}$), which have a difference in magnetic sublevels of $\Delta m_F = 2$. However, a Raman pulse with $\Delta m_F = 2$ is not possible with high fidelity for the parameters that we have chosen [112]. Therefore, we have to split this $\pi/2$ pulse into three individual pulses (parts C-E in Fig. 3.5):

(i) First, we perform a $\pi$ pulse from $\ket{\uparrow}$ to $\ket{F=2, m_F=0} := \ket{0}$. After this pulse, the qubit is no longer stored in the $Z_a = \{\ket{\downarrow} \setminus \ket{\uparrow}\}$ basis, but in the states $\ket{\downarrow}$ and $\ket{0}$. For this pulse, the two-photon frequency is $\omega_{\ket{\uparrow} \to \ket{0}} = 6.8\,\text{GHz} + \omega_L$ (for definition, see section 1.5).

(ii) Second, a $\pi/2$ pulse between $\ket{\downarrow}$ and $\ket{0}$ with two-photon frequency $\omega_{\ket{0} \to \ket{\downarrow}} = 6.8\,\text{GHz} - \omega_L$ and phase difference of $\Delta\Phi = 90°$ for the bases $XX$ or $YY$. This
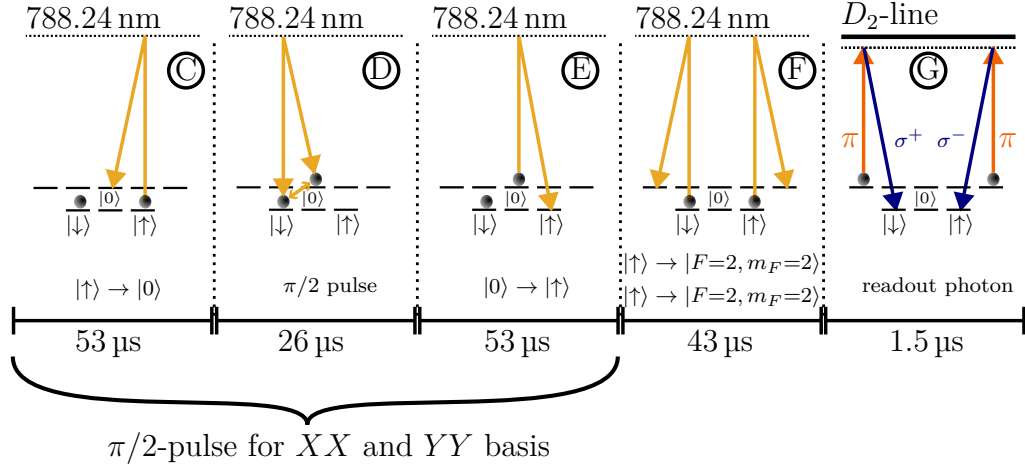
Figure 3.5: **Readout scheme for atomic qubit**. To read out the atomic qubit, the internal atomic state is mapped on the polarization of a second photon, called the readout photon. For this mapping, we perform multiple single qubit rotations, which depend on the measurement basis. In $ZZ$, we perform only one state transfer (part F) and then generate the readout photon. This way, the basis states $|\uparrow\rangle$ and $|\downarrow\rangle$ of the $ZZ$ basis are unambiguously assigned to the polarization of the readout photon. For the readout in the $XX$ and $YY$ basis, we first map the basis states of the respective basis (pulses C to E) to the basis states of the $ZZ$ and then continue with the same readout protocol as for the $ZZ$ basis (parts F and G).

results in the following map

$$\frac{1}{\sqrt{2}}\left(|\downarrow\rangle + |0\rangle\right) \;\rightarrow |0\rangle \tag{3.3}$$

$$\frac{1}{\sqrt{2}}\left(|\downarrow\rangle - |0\rangle\right) \;\rightarrow |\downarrow\rangle \tag{3.4}$$

$$\frac{1}{\sqrt{2}}\left(|\downarrow\rangle + i\,|0\rangle\right) \;\rightarrow |0\rangle \tag{3.5}$$

$$\frac{1}{\sqrt{2}}\left(|\downarrow\rangle - i\,|0\rangle\right) \;\rightarrow |\downarrow\rangle. \tag{3.6}$$

(iii) Last, a $\pi$ pulse between $|0\rangle$ and $|\uparrow\rangle$ to store the qubit in the basis states of the $Z_a$ basis again, i.e. in $|\downarrow\rangle$ and $|\uparrow\rangle$.

The phase $\Phi$ of the pulse (ii) for the readout in $X_a$ and $Y_a$ differs by 90° and therefore needs to be adjusted precisely. After pulse (i) of the three-part pulse, the qubit evolves at the frequency $\omega_{|0\rangle\rightarrow|\downarrow\rangle}$. However, the RF-frequency of the Raman laser oscillates at $\omega_{|\uparrow\rangle\rightarrow|0\rangle}$. Thus, the qubit in $|\downarrow\rangle \setminus |0\rangle$ accumulates a phase of $\Phi(T) = 2T\omega_L$ with respect to the Raman Laser, where $T$ is the time elapsed between the end of the atomic state transfer to $|0\rangle$ and the time at which the two-photon frequency is changed from $\omega_{|\uparrow\rangle\rightarrow|0\rangle}$ to $\omega_{|0\rangle\rightarrow|\downarrow\rangle}$. By scanning the time $T$, at which the phase is changed between the two different frequencies, one can find the correct time $T_0$ (and therefore the correct phase $\Phi_0 = \Phi(T_0)$) for the second rotation pulse (ii). This time corresponds to the time at which the desired correlations between the polarization of
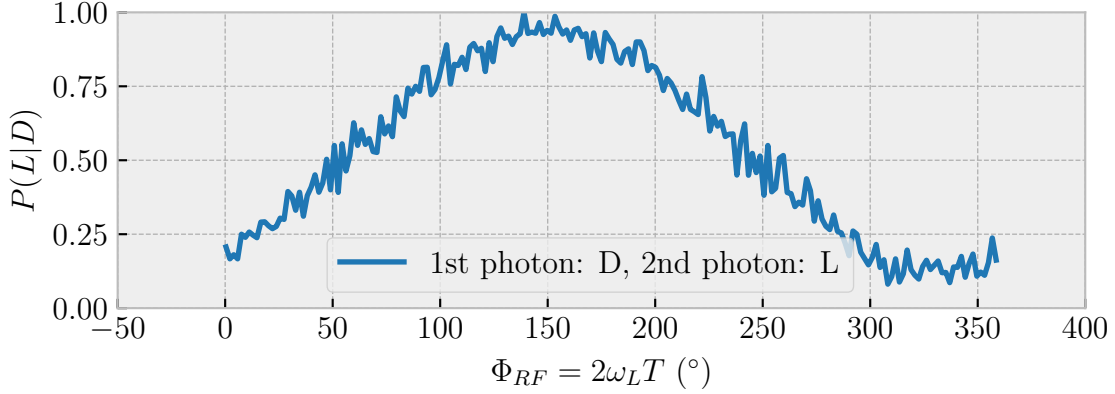
Figure 3.6: **Probability $P(L|D)$ to detect the readout photon in $|L\rangle$, conditioned on detecting the signal photon in $|D\rangle$ versus the phase $\Phi_{RF}$ of the $\pi/2$-pulse for the state readout in $XX$ and $YY$**. A $\pi/2$ pulse between $|\downarrow\rangle$ and $|\uparrow\rangle$ needs to be performed to map the $X_a$ and $Y_a$ to the $Z_a$ basis for the state readout. The correct phase $\Phi_{RF} = 2\omega_L T$ of this rotation is found by maximizing the correlations between the polarization of the signal and the polarization of the readout photon while scanning the switching time $T$ at which the two-photon frequency is switched from $\omega_{|\uparrow\rangle \to |0\rangle}$ to $\omega_{|0\rangle \to |\downarrow\rangle}$. In the shown example, the probability to detect a $|L\rangle$ polarized readout photon after a $|D\rangle$ polarized signal photon, i.e. $P(L|D)$, is maximized. As the phase $\Phi_{RF}$ differs by 90° for $XX$ and $YY$,the timing must be scanned for both bases.

the signal photon (measured in either $X_p$ or $Y_p$) and the polarization of the readout photon (measured in $Z_p$) are maximized. This is shown in Fig. 3.6. For both the $XX$ and $YY$ basis, the timing must be scanned. After this $\pi/2 - pulse$, the qubit is stored again in the $Z_a$ basis and can be read out with a state transfer and another vSTIRAP pulse, as in the $Z_a$ basis.

To read out the polarization of the generated photons, we use a polarization-resolving detection setup. This setup is shown in Fig. 3.4. It consists of an electro-optical modulator (EOM), a polarizing beam splitter (PBS) and multiple waveplates (not shown) for adjusting the polarization. The output ports of the PBS are connected to superconducting nanowire single photon detector (SNSPD). The PBS deflects orthogonal polarizations into two different optical paths and. This way, it defines the detection basis. By adding additional waveplates in front of the PBS, arbitrary detection bases can be set, i.e. the bases $XX$, $YY$, and $ZZ$. However, the waveplates do not allow fast switching of the detection basis. Therefore, we use the additional EOM to switch the polarization basis between the signal and the readout photon. The EOM imprints a phase on a specific polarization of a photonic qubit while it propagates through the crystal of the EOM. This imprinted phase is controlled externally with a TTL signal. This can be used, to switch between two different polarization detection bases. The detection basis needs to be switched between the detection and the readout photons. For the readout photon we only

need $Z_p = \{|R\rangle, |L\rangle\}$ as detection basis. For the signal photon we need either $Z_P$, $Y_p = \{|A\rangle, |D\rangle\}$ or $X_p = \{|H\rangle, |V\rangle\}$, depending on the measurement basis. The TTL signal can therefore be used to quickly ($< 1\,\mu s$) switch the detection basis between $X_p$ and $Z_p$ or $Y_p$ and $Z_p$ for the signal and readout photon. To switch between $X_p$ and $Y_p$, we adjust the settings of the waveplates by hand.

### 3.1.5 Fidelity

The fidelity $\mathcal{F}$ of the generated state $\rho$ with the Bell state $|\Psi^+\rangle$ is given by $\mathcal{F} = \text{Tr}(|\Psi^+\rangle \langle\Psi^+| \rho) = \langle\Psi^+| \rho |\Psi^+\rangle$. To determine this fidelity, we measure correlations between the polarization of the signal photon and the atomic state in three different bases, namely $XX, YY$ and $ZZ$. We define $XX = X_a \otimes X_p, YY = Y_a \otimes Y_p$ and $ZZ = Z_a \otimes Z_p$. The bases are defined in Table 3.1. In the $ZZ$ basis, the generated state can be expressed as

$$|\Psi^+\rangle = \frac{1}{\sqrt{2}} (|R,\uparrow\rangle + |L,\downarrow\rangle) \tag{3.7}$$

and in $XX$ and $YY$ as

$$|\Psi^+\rangle = \frac{1}{\sqrt{2}} (|H,\uparrow_x\rangle + |V,\downarrow_x\rangle) \tag{3.8}$$

$$|\Psi^+\rangle = \frac{1}{\sqrt{2}} (|D,\uparrow_y\rangle - |A,\downarrow_y\rangle) . \tag{3.9}$$

This means, for example, that in $XX$ correlations between the atomic states $|\uparrow_x\rangle$ and $|\downarrow_x\rangle$ and the polarization states $|H\rangle$ and $|V\rangle$ have to be measured. How to read out the individual states is explained in section 3.1.4. The correlations are then used to calculate the two-qubit Stokes parameters $S_{xx}, S_{yy}$ and $S_{zz}$, which are defined as [113]

$$S_{xx} = P_{\uparrow x, H} - P_{\uparrow x, V} - P_{\downarrow x, H} + P_{\downarrow x, V} \tag{3.10}$$

$$S_{yy} = P_{\uparrow y, A} - P_{\uparrow y, D} - P_{\downarrow y, A} + P_{\downarrow y, D} \tag{3.11}$$

$$S_{zz} = P_{\uparrow, R} - P_{\uparrow, L} - P_{\downarrow, R} + P_{\downarrow, L}, \tag{3.12}$$

where $P_{jj}$ stands for the probability to measure the state $|j,j\rangle$ and $P_{j,j} + P_{j,-j} + P_{-j,j} + P_{-j,-j} = 1$. From these two-qubit Stokes parameters, we obtain the fidelity by

$$\mathcal{F} = \frac{1}{4} (1 + S_{xx} + S_{yy} - S_{zz}) . \tag{3.13}$$

Hence, by measuring the correlations in the different bases, we are able to determine the fidelity $\mathcal{F}$ of the generated Bell State. For a single atome, we obtain a value of $\mathcal{F} = 86.6(5)\,\%$ for a single atom. Typical values for $S_{zz}$ are in the range of 0.95 to 0.97 and for $S_{xx}$ and $S_{yy}$ in the range of 0.7 to 0.75. The values in the $ZZ$ basis are significantly higher than the ones in $XX$ and $YY$. Several factors are responsible for this: the additional $\pi/2$ pulse between $|\uparrow\rangle$ and $|\downarrow\rangle$, the photon acceptance window $\tau$ and the coherence time. How these factors influence the fidelity is discussed in section 3.3.

## 3.2 Atom-photon entanglement generation with atomic arrays

Now that we have explained how to generate and measure atom-photon entanglement between the internal atomic state of a single atom and the polarization of a photon, we use the same protocol to generate APE for arrays of atoms. When working with atomic arrays, crosstalk can in principle become a huge problem. Therefore, we start by measuring the crosstalk between neighboring atoms and use this measurement to determine the optimal inter-atomic distance, see subsection 3.2.1. Once we have found the optimal distance, we load one- and two-dimensional arrays and investigate the performance of our qubit register in terms of our two metrics, efficiency and fidelity, while we increase the system size (subsection 3.2.2). Afterwards, we show how we use the quantum register to increase the efficiency of the APE generation using a multiplexing protocol (subsection 3.2.3).

### 3.2.1 Crosstalk

The distance between adjacent atoms is an important parameter when working with multiple atoms in an optical cavity. As all atoms must couple to the cavity field, all atoms of the array must be placed within the cavity mode. Therefore, if the distance between neighboring atoms is unnecessarily big, the maximum size of the atomic array in the cavity is unnecessarily reduced. On the other hand, if the distance between the neighboring atoms is too small, the fidelity of individual operations can potentially decrease due to crosstalk. For example, when generating atom-photon entanglement, the emission of a photon may be stimulated from a non-addressed atom, which might be partially illuminated by the addressing beam if the distance between neighboring atoms is too small. The polarization of this generated photon does not correlate with the internal atomic state of the actually addressed atom and this therefore leads to a reduction of the fidelity. Hence, it is important to find the correct distance between neighboring atoms that leads to the maximum number of atoms in the resonator mode while keeping the crosstalk as small as possible. To find this optimum distance, we placed two atoms at different interatomic distances $\Delta_x$ in the range of $3\,\mu m$ to $17.5\,\mu m$ along the $x$-axis (orthogonal to the cavity) in the resonator and measured the fidelity $\mathcal{F}$ for each atom for each distance. We then calculate the average fidelity $\overline{\mathcal{F}}$ for each interatomic distance. The results of this measurement are shown in Fig. 3.7. The blue dashed line indicates the average fidelity $\overline{\mathcal{F}}$ of both atoms, and the blue shaded area indicates the range of values within one standard deviation (0.4 %). We see that for the measured distances the fidelity $\overline{\mathcal{F}}$ is independent from the distance $\Delta_x$ of the neighboring atoms. However, for small distances between the atoms, the preparation efficiency of the atomic arrays decreases because of interference effects from neighboring optical tweezers. The interference of neighboring tweezers leads to modified, arbitrary potential landscapes, distorted spatial wave functions of the atoms, and an increased hopping rate between adjacent tweezers. This is detrimental to the preparation of ordered arrays. Similar interference effects were observed in [114]. We therefore chose a distance of $5.5\,\mu m$ between neighboring atoms. This distance is the minimum distance between
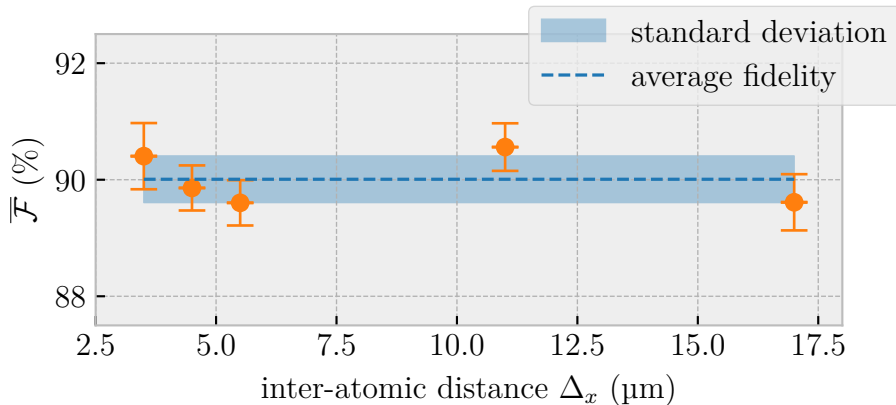
Figure 3.7: **Crosstalk between adjacent atoms**. To determine the crosstalk between neighboring atoms, we measure the average fidelity $\overline{\mathcal{F}}$ of two atoms for interatomic distances $\Delta_x$ in a range of $3\,\mu\mathrm{m}$ to $17.5\,\mu\mathrm{m}$. The average fidelity is constant and within the entire range and we observe no decrease of the fidelity due to crosstalk. Since the preparation efficiency decreases for interatomic distances below $5.5\,\mu\mathrm{m}$, we set the distance between neighboring atoms for the multi-atom experiments to $5.5\,\mu\mathrm{m}$.

neighboring atoms for which interference effects from adjacent optical tweezers can be neglected. With this distance of $\Delta_x = 5.5\,\mu\mathrm{m}$, we perform the following experiments.

## 3.2.2 Scalability of the atomic register

In this subsection, we discuss the scalability of our network register. Scalability describes to the ability to increase the size of a system. However, being able to increase the size of the system does not mean that the system is truly scalable, since, for example, the error rate in a system may increase as more qubits are added to the system. To correct for this potential increase in error rate, additional error correction qubits would be needed. If these additional error correction qubits also need error correction, the experimental overhead could become unmanageable, making the system unscalable. Therefore, scalability does not only describe the ability to increase the size of the system, but also the ability to increase the size of the system while maintaining a constant error rate. For our register, both the fidelity and the APE generation efficiency of the individual atoms could be affected by a higher number of qubits in the register due to, for example, decoherence, position-dependent differences when addressing the atoms or coupling to the resonator. Therefore, to show the scalability of our system, it is important to demonstrate that both quantities are independent from the number of qubits in the register.

To characterize the efficiency and fidelity of our system, we first need to extend the experimental sequence from a single atom to multiple atoms. Therefore, we replace the single vSTIRAP pulse of the previous sequence with $N$ subsequent vSTI-
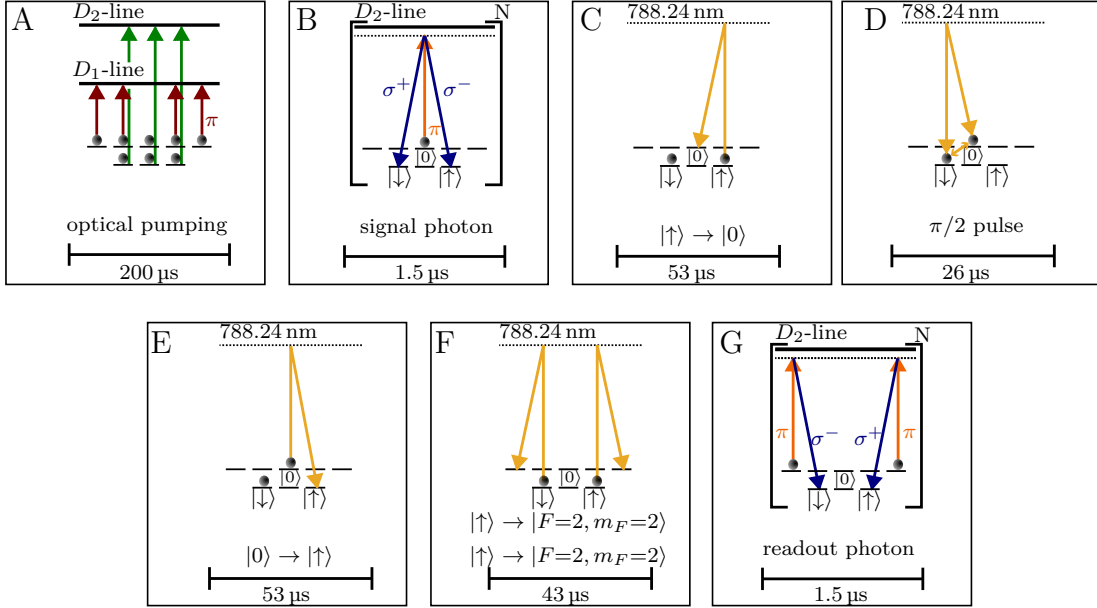
Figure 3.8: **Full experimental sequence for $N$ atoms**. The only difference between the sequence with multiple atoms and the sequence for a single atom (see Fig. 3.1) is the number of vSTIRAP pulses. For $N$ atoms, $N$ vSTIRAP pulses are required to generate the signal and the readout photon. This way, ideally $N$ photons are generated and each of the photons is entangled with the internal atomic state of one of the $N$ atoms. The individual pulses are separated in time and therefore the photons are in different temporal modes.

RAP pulses to individually address all $N$ atoms of the atomic array, see Fig. 3.8. The individual vSTIRAP pulses are separated in time by about $15\,\mu s$ , given by the switching time of the AOD. This way, we ideally generate $N$ photons, each entangled with the internal atomic state of the addressed atom, in $N$ different temporal modes.

To demonstrate that the efficiency and fidelity are both independent from the number of atoms in the register, we measure both quantities for one-dimensional atomic arrays with up to six atoms. This is shown in Fig. 3.9. These results have to be compared to the fidelity and the efficiency for a single atom. As described in section 3.1.3, the efficiency for generating and detecting a single photon is $\eta_{overall} = 33.2(3)\,\%$ and the fidelity is $86.6(5)\,\%$. We observe that the fidelity $\mathcal{F}$ of the generated entangled states in the atomic arrays remains almost at the same level as for the single atom for each individual atom. This can be seen in the almost constant average fidelity $\overline{\mathcal{F}}$ for all numbers of atoms. For example, the average fidelity for six atoms is $85.5(4)\,\%$. The average fidelity is shown in Fig. 3.10 A, including (in blue) the standard deviation of about $0.7\,\%$.

However, the efficiency does not remain constant for all the atoms. We see a decrease in efficiency for the outer atoms, which is, however, expected. As the efficiency is related to the cooperativity $C$, see equation (3.2), and since the coupling $g$ decreases when the atoms are located at outer positions in the array orthogonal to the cavity
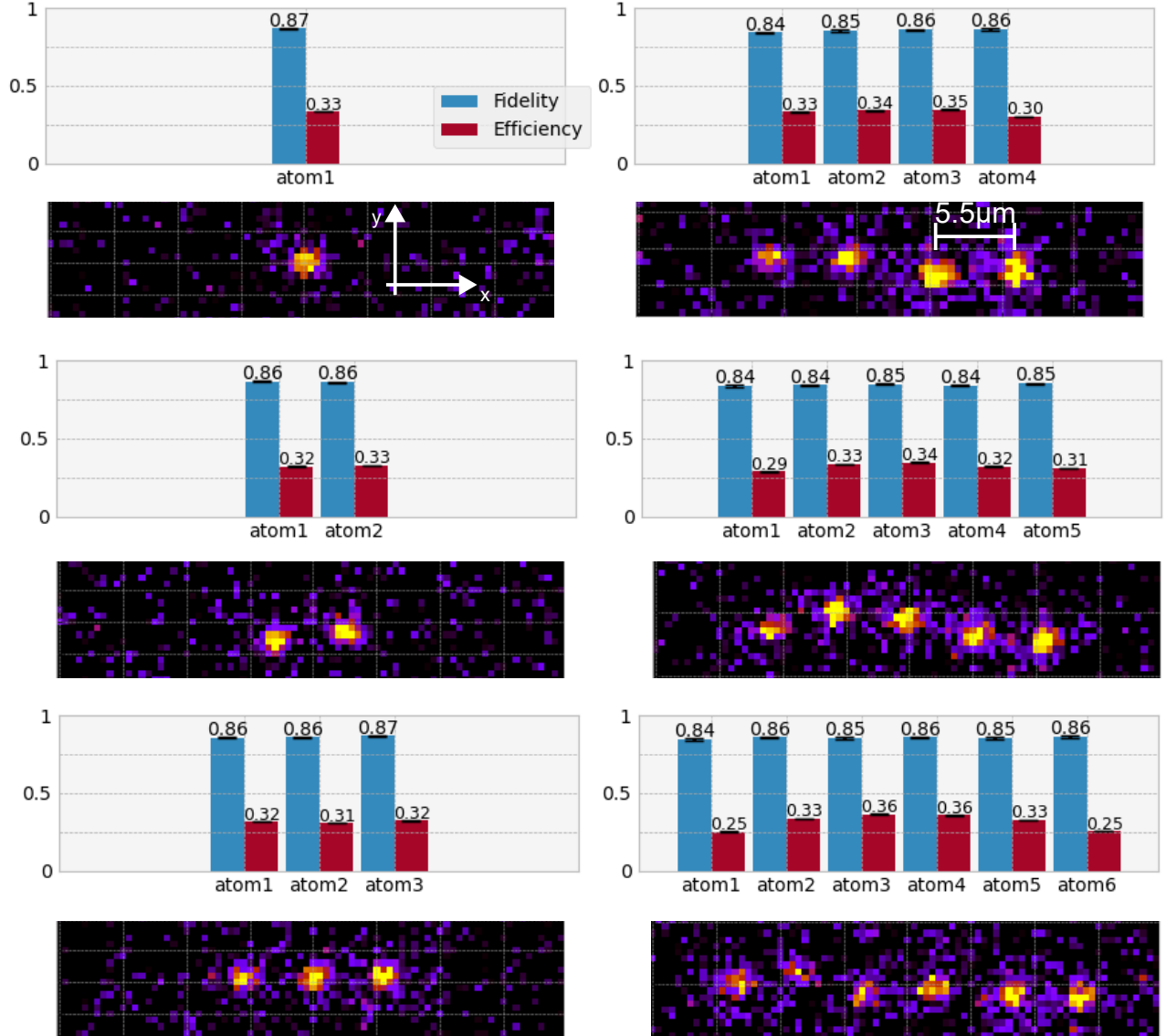
Figure 3.9: **Photon detection efficiencies $\eta_i$, fidelities $\mathcal{F}$ and atom pictures for one to six atoms in a one-dimensional array**. For each atom, we measure the fidelity $\mathcal{F}$ and the generation-to-detection efficiency $\eta_{overall}$. The fidelity is almost constant for each individual atom (see also Fig. 3.10). However, the efficiency decreases for the atoms that are further away from the center of the cavity. This decrease is expected because of the reduction in cooperativity when the coupling becomes smaller, as it is the case for the outer atoms.
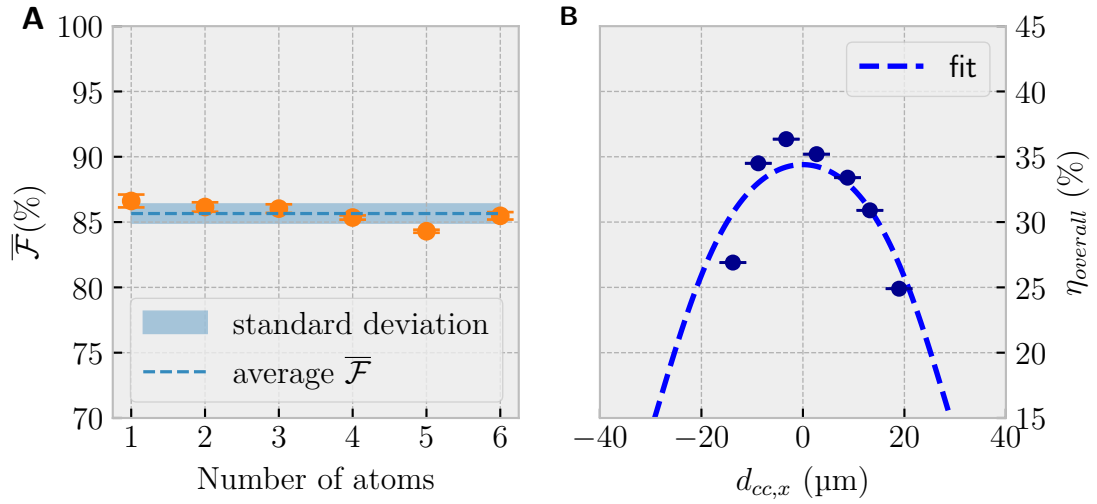
Figure 3.10:   **Average fidelity $\overline{\mathcal{F}}$ vs. the number of atoms and position-dependent entanglement generation efficiency $\eta_{overall}$ along the $x$-axis. A** The average Fidelity $\overline{\mathcal{F}}$ remains almost constant for up to six atoms with a standard deviation of less than $0.7\,\%$. **B** The entanglement generation and detection efficiency $\eta_{overall}$ depends, as described in equation (3.2), on the position of the atom in the cavity along the $x$-axis(orthogonal to the cavity). Here, we show the efficiency of a single atom for different distances to the cavity center $d_{xx,c}$. We use a fitting model that includes the finite cavity waist $w_0$, the cavity QED parameters $g, \kappa, \kappa_{out}, \gamma$, and uses only $\xi$ (the product of the total transmission and detection efficiency with the optical pumping efficiency) as a free fitting parameter. By fitting the measured data, we obtain $\xi = 48.6(13)\,\%$, consistent with the measured value of $51(6)\,\%$.

axis, the efficiency also decreases. This is depicted in Fig. 3.10 B, which shows how the overall entanglement generation and detection efficiency $\eta_{overall}$ depends on the distance $d_{cc,x}$ of a single atom from the cavity center along the $x$-axis. As expected, the maximum is in the center of the cavity and the efficiency decreases when the atom is positioned away from the center. To demonstrate that the efficiency behaves as expected, we fit the data with the model from equation (3.2), using $\xi$ as the only free parameter. We obtain $\xi = 48.6(13)\,\%$, consistent with the measured value of $51(6)\,\%$.

Due to the finite temperature of the atoms, the atoms hop between different lattice sites, especially along the cavity axis. This affects the APE generation efficiency, as the efficiency to generate atom-photon entanglement depends heavily on precise addressing. Therefore, we have to follow the hopping of the atoms. The rate of this hopping is below $1\,\mathrm{Hz}$. Therefore, for each picture (rate is $3\,\mathrm{Hz}$), we determine the atomic positions of all the atoms in the array and update the RF frequencies that we send to the AOD that we use for the addressing of the atoms. As we observe that the measured efficiencies for each atom are close to the theoretical maximum, the hopping is currently not limiting the scalability of our setup.

With these measurements, we show that we can position six atoms in a line along the $x$-axis in the resonator and neither fidelity nor efficiency behave in an unexpected way. However, the number of atoms along this axis is limited by the finite mode waist of the cavity of $w_0 = 30\,\mu\mathrm{m}$. Therefore, to show that our register can potentially accommodate a larger number of atoms, atoms must also be positioned along the $y$-axis, i.e. two-dimensional arrays must be prepared. Two two-dimensional arrays consisting of two and four atoms are shown in Fig. 3.11. In the same Fig., the entanglement generation efficiency and the fidelity for the individual atoms are depicted as well. As with the one dimensional array, no reduction in fidelity can be seen in the two-dimensional case. However, the efficiency of the atoms along the cavity axis is again position-dependent as $C \propto g^2$ and $g$ itself oscillates along the cavity axis as it is proportional to the amplitude of the electric field mode of the cavity. This mode is a standing wave and it is resonant with the atomic transition frequency $\lambda_{cav} = 780\,\mathrm{nm}$. However, as we use a blue intracavity trap at $770\,\mathrm{nm}$ for the spatial confinement of the atoms, the atoms are not necessarily trapped at a position of maximum $g$ along the entire cavity axis. The frequency of the blue trap is set such that at the center of the cavity an intensity minimum of the blue trap coincides with a maximum of photon generation efficiency, but this changes along the cavity axis. This is illustrated in Fig. 3.12, where we plot the intrinsic photon generation efficiency $P$ and the intensity $I_{770}$ of the $770\,\mathrm{nm}$ trap versus the position in the cavity in different areas along the cavity axis. At the center of the cavity, the maximum photon generation efficiency coincides with an antinode of the blue-detuned intracavity trap (plot A), which repeats again after $\sim 32\,\mu\mathrm{m}$ (plot D). Between these two positions, the atom, however, is not trapped at positions of maximum photon generation efficiency. For example, after $\sim 16\,\mu\mathrm{m}$ (plot C) the atom is trapped at a position of minimum coupling. when the atom is positioned at $5.5\,\mu\mathrm{m}$ (plot B) away from the cavity center, the intrinsic generation efficiency drops by

approximately 25 %, i.e. if at the center the detection efficiency $\eta$ is 33.2(3) %, the efficiency drops to 24.9(1) %. This efficiency can be increased, however, by using a wavelength of the intracavity trap closer to the resonance frequency of the cavity.

However, the number of atoms that we can position along the $y$-axis is limited in the current setup due to the beam waist of the 1064 nm standing wave trap. The beam waist is 13 µm. This limitation could be overcome by using several such standing wave traps in parallel, which would allow us to further increase the number of atoms that that can be stored. In section 3.4, we discuss in more detail what needs to be done to scale the register to larger system sizes, and what the ultimate limits are.
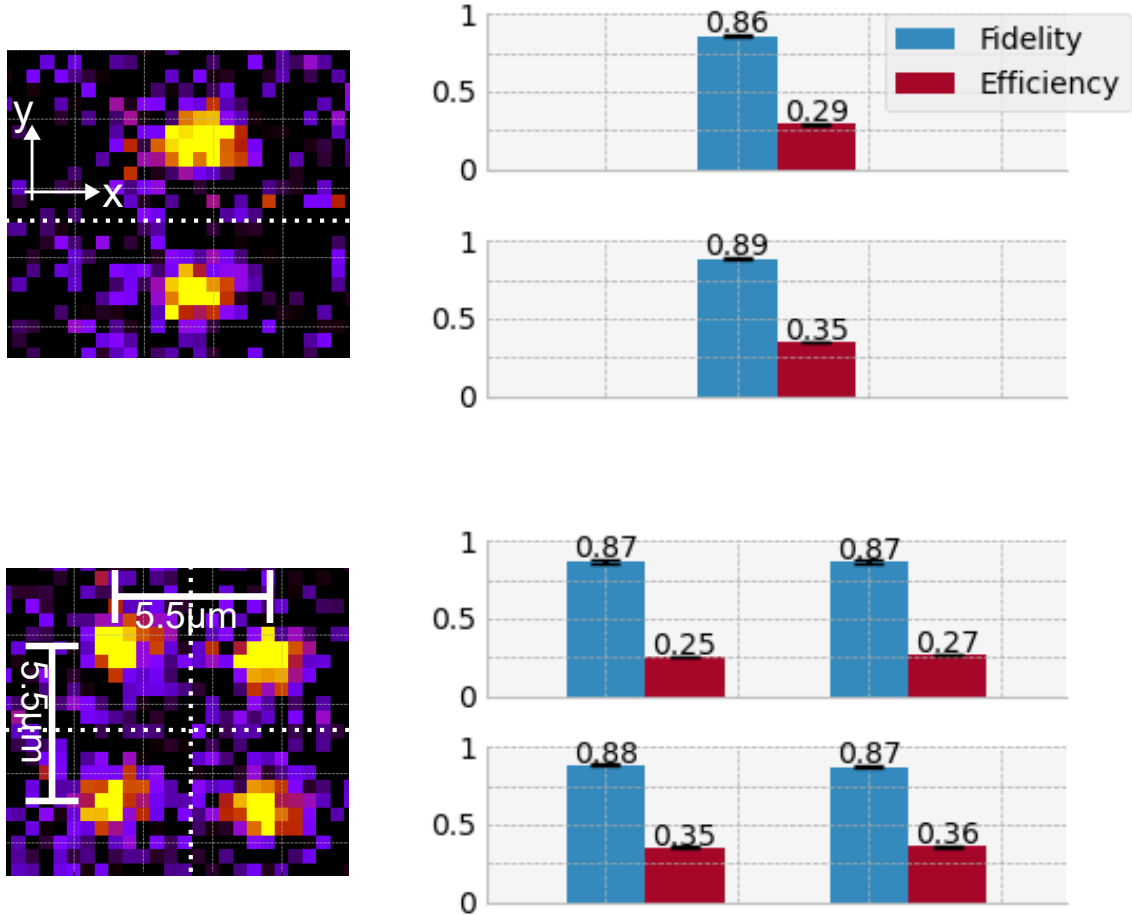
Figure 3.11: **Photon detection efficiencies $\eta_i$, fidelities $\mathcal{F}$ and atom pictures for the two-dimensional configurations.** Since the number of atoms along the $x$-axis (orthogonal to the cavity axis) is limited, increasing the register along the $y$-axis is the key step to achieve larger register sizes. The upper picture shows a $2x1$ array along the $y$-axis and the lower picture shows a $2x2$ array. Both pictures include the fidelity and the efficiency for each individual atom. The fidelity $\mathcal{F}$ remains constant for each individual atom along the $y$-axis. However, the efficiency decreases slightly for the atoms that are positioned at $5.5\,\mu\text{m}$ from the cavity center (upper atoms) because of the decrease in cooperativity resulting from our trap configuration, see Fig. 3.12.
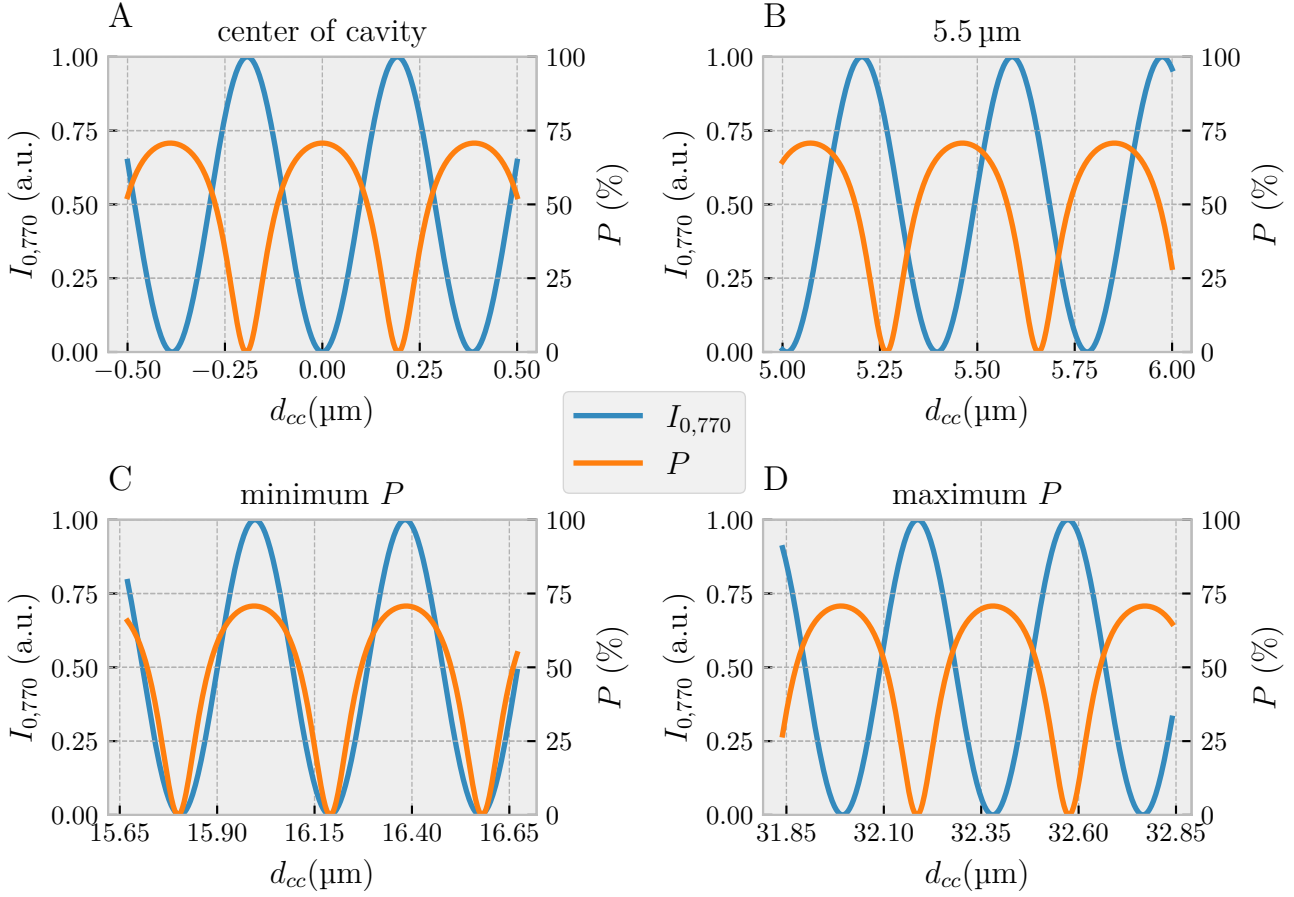
Figure 3.12: **Intrinsic photon generation efficiency $P$ and intensity of the intracavity trap $I_{770}$ vs. position along the cavity axis**. As the wavelengths of the intracavity trap and the cavity mode differ, the position of maximum photon generation efficiency $P$ and the antinodes of the intracavity trap do only coincide at specific positions. As the atoms are always trapped at the antinodes of the blue-detuned intracavity standing wave trap, the generation efficiency $P$ is position-dependent along the $y$-axis with a period of $\sim 32\,\mu m$. The frequency of the intracavity trap is set such that at the center of the cavity $P$ is maximum [77].

### 3.2.3 Multiplexed atom-photon entanglement generation

The deterministic distribution of entanglement between two distant network nodes is a necessary capability for quantum networks, but it has not yet been demonstrated until today. In this section, we describe how a quantum network register can be useful in bringing us closer to achieving this capability. In a typical protocol (see Fig. 3.13) for entanglement distribution two nodes A and B, entanglement is first created between a quantum memory and a photon at one node, e.g., node A. The entangled photon is then sent via an optical fiber to node B, where it is used to establish entanglement between the quantum memory at node B and the memory at node A. However, such an entanglement distribution process is inherently lossy, which is why a repeat-until-success strategy must be applied. In such a strategy, a successful attempt is indicated by a so-called herald. The result of the attempt is then sent to node A with a classical communication signal that propagates from node B to node A at most at the speed of light. Hence, a new entanglement attempt can only be made after the result of the previous attempt has been communicated between the nodes. As the transmission speed of the entangled photon and the measurement outcome is at most the speed of light, the travel time of the signals limits the repetition rate of the entanglement attempts. The limit for the repetition rate is given by $c/L$, where $L$ is the distance between the nodes.[1] As the limit upper limit for the rate is given by the speed of light, it is system-independent and the same for all possible implementations of a quantum memory. Already at distances in the range of $L \approx 100\,\mathrm{km}$, the upper limit for the entanglement distribution rate in heralded schemes is limited to $1\,\mathrm{kHz}$ [115]. However, using $n$ quantum memories simultaneously, allows to increase the rate by a factor of $n$, as a new entanglement attempt can already be started during the travel time of the photons in the network.

In addition to increasing the rate, multiplexing also increases the efficiency of generating entanglement. In our setup, the efficiency to generate and detect entanglement is $\eta_{overall} = 33.2(3)\,\%$ and the efficiency to generate and fiber-couple $\eta_{fiber} = 48(5)\,\%$ for a single atom. For $N$ emitters, the efficiency $\eta$ ($\eta$ here stands for both the in-fiber efficiency $\eta_{fiber}$ and the generation-to-detection efficiency $\eta_{overall}$) that at least one of the emitters emits a photon is given by $\eta = 1 - \prod_i^N (1 - \eta_i)$, where $\eta_i$ is the efficiency of the i-th emitter. The protocol in Fig. 3.8 represents a multiplexing protocol with up to six atoms. We can use it to experimentally verify the expected increase of the efficiency and the entanglement rate. Figure 3.14 shows the experimental results. It indicates that both the efficiency $\eta$ and the average number of photons $N$ increase with the number of emitters. It shows that the average photon number $\overline{n}$ scales almost linearly with the number of emitters and the maximum average photon number $\overline{n} = 1.88(1)$ is achieved for six atoms , which is an almost five-fold increase compared to a single atom. The maximum generation-to-detection efficiency is $\eta_{overall} = 88.6(1)\,\%$ and the maximum in-fiber efficiency is $\eta_{fiber} = 97.4(6)\,\%$. The

---

[1]For the protocol described here, the maximum repetition rate is actually $c/(2L)$, since both the entangled photon and the classical signal must be exchanged. However, in a configuration in which both parties entangle a photon with their quantum memory and send the entangled photon to an intermediate station, where an optical bell state measurement is performed to entangle both quantum memories, the mentioned rate of $c/L$ can be achieved.
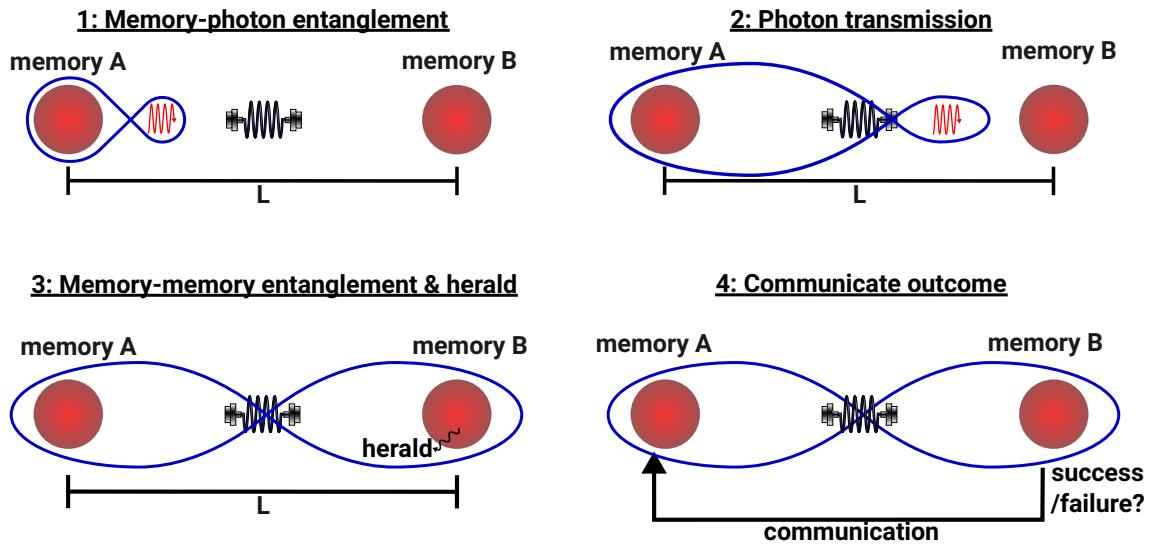
Figure 3.13:   **Typical scheme for heralded entanglement distribution between two parties A and B.** The protocol starts by entangling (entanglement is represented by the blue infinity sign) one quantum memory with a photon (red wavy arrow). This photon is transmitted through an optical fiber and used at node B to establish entanglement between the two quantum memories at the nodes A and B. The steps 1-3 are probabilistic and therefore a herald is needed to signal the failure or success of the attempt. For the deterministic distribution of entanglement, a repeat-until-success strategy has to be used. However, the communication time required to share the result of the attempt limits the rate at which entanglement attempts can be started.

in-fiber efficiency is calculated from the overall detection efficiency $\eta_{overall}$ by correcting for the overall detection and transmission efficiency of $70(7)\%$. This result demonstrates that multiplexing is a promising tool for the deterministic distribution of entanglement in quantum networks.
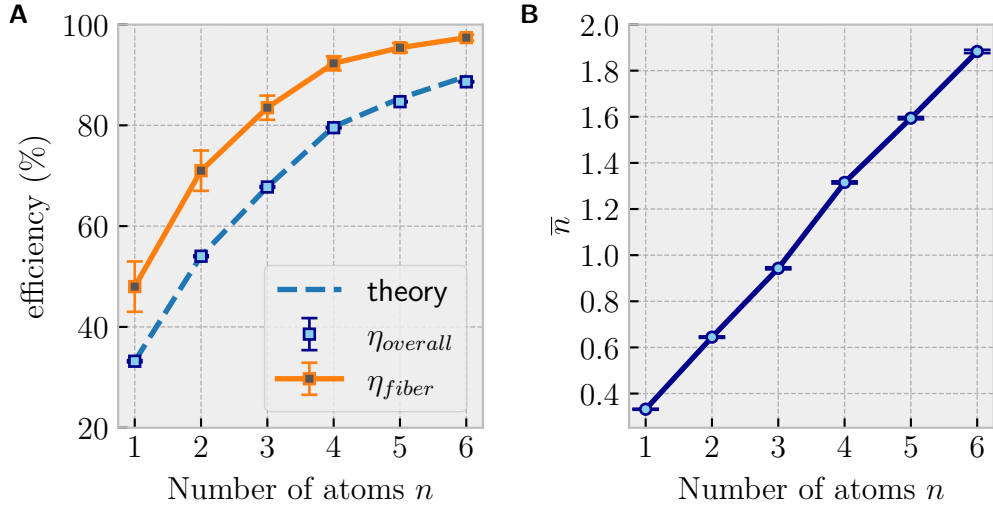
Figure 3.14: **Increase of the efficiencies $\eta_{overall}$ and $\eta_{fiber}$ and the average number of photons $\overline{n}$ through multiplexing**. Efficiencies $\eta_{overall}$ and $\eta_{fiber}$ **(A)** and average number of photons $\overline{n}$ **(B)** versus number of atoms. The theoretical efficiency of detecting at least one photon for $N$ emitters is calculated using the formula $\eta_{overall} = 1 - \prod_i^N (1 - \eta_{overall,i})$, where $\eta_{overall,i}$ is the overall efficiency of the i-th atom. We measure a maximum overall detection efficiency $\eta_{overall}$ (in-fiber efficiency $\eta_{fiber}$) of $88.6(1)\,\%$ $(97.4(6)\,\%)$ for six atoms, compared to $33.2(3)\,\%$ $(48(5)\,\%)$ for a single atom. The in-fiber efficiency is calculated from the overall efficiency, using a corrected in-fiber efficiency of $70(7)\,\%$ instead of the overall propagation and detection efficiency. The average number of photons $\overline{n}$ increases almost linearly to a maximum of $1.88(1)$. As a guide for the eye, we have added a blue curve in B that connects the individual data points. The plot is taken from [108] and has been modified.

## 3.3 Analysis of Experimental Imperfections

In the presented experiment, we measure a fidelity of $\mathcal{F} = 86.6(5)\,\%$ for a single atom. However, in the twin experiment, the pistol experiment, fidelities of $97.1(1)\,\%$ have been observed [116]. In principle, comparable values should be possible in our experiment. There are several reasons for the lower fidelity: the temporal shape of the photon, the coherence time, state preparation and readout, the $\pi/2$-pulse between $|\uparrow\rangle$ and $|\downarrow\rangle$, and the polarization settings ($\pi$-polarization) for the vSTIRAP-pulse with the addressing. In the next two subsections, we discuss the two main sources for the infidelity: the temporal shape of the photon and the coherence time. The polarization settings for the addressing beam, which may be a source for large infidelities, are discussed in section 3.3.3. For the atom preparation and state readout, we estimate an entanglement infidelity of $2.7(2)\,\%$. We attribute the remaining $2.5\,\%$ of infidelity to the $\pi/2$ pulse between $|\uparrow\rangle$ and $|\downarrow\rangle$.

### 3.3.1 Temporal shape of the photon

The temporal shape of the generated photon is extensively discussed in [93]. A typical temporal shape of a photon that we generate is shown in 3.15. After the detection of the photon at time $t_{det}$, the atomic qubit is projected onto an eigenstate of the respective measurement basis. In $XX$ and $YY$, this corresponds to a superposition state

$$|\Psi_{atom}\rangle = \frac{1}{\sqrt{2}} \left( |\uparrow\rangle + \exp(i\phi) |\downarrow\rangle \right). \tag{3.14}$$

The atomic state $|\Psi_{atom}\rangle$ then evolves freely in time interval $\tilde{T}$ up to the time $t_{\pi/2}$, at which the three-part $\pi/2$ pulse begins, i.e., $\tilde{T} = t_{\pi/2} - t_{det}$. As the states $|\uparrow\rangle$ and $|\downarrow\rangle$ are energetically separated by twice the Larmor frequency, the qubit evolves at this frequency $2 \times \omega_L = 2\pi \times 200\,\text{kHz}$. As the temporal distribution of the emission time of the photon $t_{det}$ therefore is non-zero, the temporal distribution for the time interval $\tilde{T}$ during which the atomic state evolves freely is non-zero as well. This leads to a phase uncertainty $\Delta\phi$ of the atomic state $|\Psi_{atom}\rangle$ at the beginning of the $\pi/2$ pulse, resulting in infidelities in the $\pi/2$ pulse and consequently in the generated atom-photon entangled state $\rho$. This infidelity can be reduced, however, by only accepting photons within a certain time window, which reduces the phase uncertainty at the beginning of the $\pi/2$ pulse. We therefore only accept photons within a time window of $\tau = 1.25\,\mu\text{s}$. Using this time window, we calculate a theoretical maximum for the fidelity of $\mathcal{F} = 96.2\,\%$. Theoretically, we could reduce the time window even further and therefore increase the maximum fidelity, but this would lower the photon generation efficiency. Another option is to increase the power of the vSTIRAP pulse, as it makes the photon shorter in time. However, we observe again an unknown heating effect that reduces substantially the storage time of the atoms when we increase the power.

### 3.3.2 Coherence time

In the $XX$ and $YY$ bases, the atomic qubit is stored in a coherent superposition of $|\uparrow\rangle$ and $|\downarrow\rangle$ until after the pulse (ii) of the three-part $\pi/2$-pulse (see section 3.1.4).
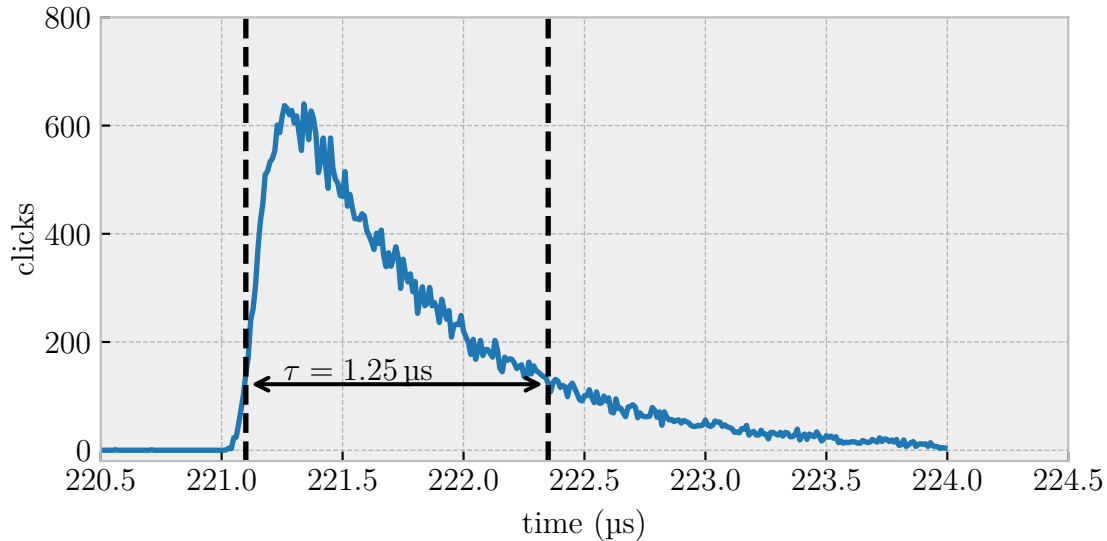
Figure 3.15: **Typical photon shape for a photon generated with the addressing system.** The non-zero temporal distribution of the photon gives an uncertainty in the phase of the atomic state after the free-evolution of the atomic state after the detection of the generated photon. This uncertainty translates into a reduction of the fidelity. By only accepting photons that were detected in a detection window, the phase uncertainty can be reduced and the fidelity reduction decreased. For the chosen time detection window of $1.25\,\mu s$, the theoretical maximum for the fidelity is $\mathcal{F} = 96.2\,\%$.

Thus, the coherence time affects the fidelity. The coherence time has a larger effect on the fidelity when qubits are added to the register, as the time duration of the experimental sequence becomes longer. To investigate the effect of the coherence time on the fidelity, we measure the coherence time in the $XX$ basis. For this measurement, we use the protocol described in section 3.1 and look at the amplitude of the oscillations that we obtain when scanning the switching time $T$ of the two-photon frequency from $\omega_{||\uparrow\rangle\rangle\to|0\rangle}$ to $\omega_{|0\rangle\to|\downarrow\rangle}$, see subsection 3.1.4. We record several such oscillation curves for different starting times $t_{start}$, i.e., the time at which we start scanning the switching time of the two-photon frequency. For the curves with later starting times, we observe a decay in the amplitude of the oscillations. From this exponential decay we extract a coherence time of $1050(50)\,\mu s$, see Fig. 3.16. Initially, the coherence time in our setup was shorter. To increase the coherence time, we implemented a feed-forward mechanism to correct for the intrinsic $50\,Hz$ magnetic field noise induced by the power line. The feed-forward mechanism extended the coherence time by a factor of 2 to 3. Since the first and the last atom are addressed at different times, the decoherence affects the individual atoms differently. For example, for the case of six atoms, the fidelity of the atom that we addressed decreases by $4.5\,\%$ and the fidelity of the atom that we addressed last by $1.5\,\%$. On average, the coherence time gives a $1.5\,\%$ to $3.5\,\%$ reduction of the fidelity, depending on the number of atoms.
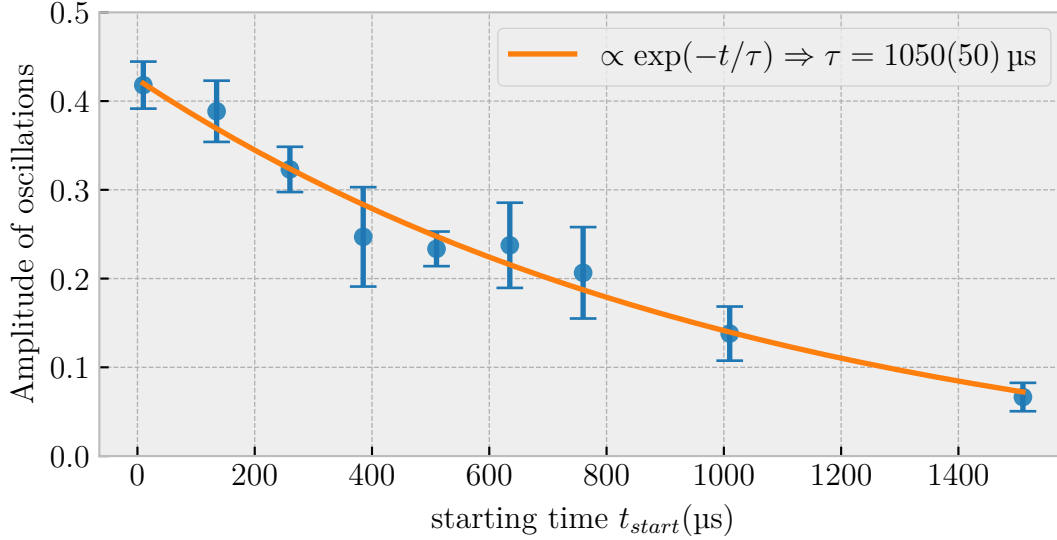
Figure 3.16: **Coherence time of the qubit in the states $|\uparrow\rangle$ and $|\downarrow\rangle$ measured in the $XX$ basis.** Each of the points in the plot corresponds to the amplitude of a phase scan, see Fig. 3.6, for a different starting time $t_{start}$ of the scan of the switching time $T$ of the two-photon frequency of the three-part $\pi/2$-pulse. We fit an exponential decay to the points and obtain a coherence time of $1050(50)\,\mu s$. With this coherence time, the infidelity from decoherence is on average $1.5\,\%$ to $3.5\,\%$, depending on the number of atoms.

### 3.3.3 Polarization of the addressing beam

As we observed strong polarization effects in coherent processes when we investigated single qubit rotations with the addressing system (see subsection 2.2.5), polarization is a potential candidate for big infidelities. For the vSTIRAP, we need pure $\pi$-polarization in the addressing beam. To set the polarization to $\pi$, we start by optically pumping the atom in $|F = 2, m_F = 2\rangle$ of the ground state (see section 2.2.4). Afterwards, we send light resonant with $|F{=}2\rangle \rightarrow |5^2P_{1/2}, F{=}1\rangle$ through the addressing onto the atoms. If this light is perfectly $\pi$-polarized, it excites population from all $m_F$ sublevels of the $|F{=}2\rangle$ ground state, except for the $m_F = 2$ sublevel. Therefore, the polarization of the light can be adjusted to $\pi$ by looking at the remaining population in $|F{=}2, m_F{=}2\rangle$. By minimizing this population, we find the best possible polarization setting, i.e., the purest $\pi$ polarization. We minimize the population by comparing the population in $|F{=}2, m_F{=}2\rangle$ before and after sending in the light that has to be set to $\pi$ polarization, using the state read-out described in subsection 1.7. Using this technique, we set the polarization of the global beam ($w_0 = 35\,\mu m$) along the 1064 axis and for the vSTIRAP of the addressing system. To compare the polarization settings of the addressing with the global beam, we look at the ratio $P_{max}$ to $P_{min}$. Here, $P_{max}$ stands for the polarization setting at which the maximum population remains in $|F{=}2, m_F{=}2\rangle$ and $P_{min}$ for the polarization setting at which the minimum population remains in $|F{=}2, m_F{=}2\rangle$. For the global beam, we obtain a ratio $P_{max}/P_{min} \approx 65$, but for the addressing system we only observe $P_{max}/P_{min} < 10$. This difference suggests that the fidelity of the generated state

should be lower with the addressing system. However, we measure almost the same fidelities for the global vSTIRAP and the addressing system. We therefore estimate the infidelities from the polarization settings to be smaller than 1 %.

## 3.4   Scalability to larger system sizes

So far, the maximum number of atoms that we used in our register is six in one dimension and four in two dimensions. However, the size of these arrays is much smaller than the size of the atomic arrays that have been generated in free-space experiments in recent years. This raises the question of how much our system can still be increased.

The maximum number of qubits in a system is usually given by practical limitations, such as the available laser power or the available space for the qubits. In our system, the maximum number of atoms in the register is given by the length of the cavity and the beam waist of the cavity mode. The length of the cavity is 486 µm and the waist is 30 µm ($1/e^2$ intensity radius). However, the field of view of the objective currently limits the area in which atoms can be trapped to a smaller region, approximately to a range of 200 µm along the cavity axis. This means that with an interatomic distance of 5.5 µm, there should be space for about 200 atoms in our register, see Fig. 3.17. However, more improvements have to be implemented so that we can work with $\mathcal{O}(100)$ atoms in our cavity and improve the performance of our register:

1. **Coherence time.** For the six atom case that we showed, the coherence time already affects the fidelity of the individual atoms. Therefore, the coherence time needs to be prolonged when increasing the system size. In the neighboring experiment, the pistol experiment, coherence times of 20 ms were already achieved by using dynamical decoupling [88]. With this coherence time, a fidelity of $\sim 96\,\%$ could be achieved for the atom that was addressed first in a register of 100 atoms.

2. **Hopping of the atoms**. At the moment, the hopping of the atoms is not yet a limitation as the APE generation efficiency is at the theoretical maximum. But in order to achieve this maximum efficiency, we need to follow the position of the atoms with our addressing system. We therefore evaluate each image (3 Hz) and afterwards adjust the RF frequencies of the AOD for each atom. However, the atom hopping rate increases as the number of atoms in the system increases. Tracking the atoms therefore becomes a challenge, because for large system sizes the hopping rate of the atoms would be higher than the imaging rate. The ratio of imaging rate versus hopping rate can be improved, however, by increasing the imaging rate, given that we achieve a better signal-to-noise ratio of our imaging system. In addition, the atoms can be cooled to the motional ground state by Raman sideband cooling, which has already been shown in our setup [117]. Cooling the atoms to the motional ground state reduces the hopping rate and reduces the need for a faster imaging system.

3. **Loading of the atoms.** In Fig. 2.17 in chapter 2, the loading rate already decreases for six or seven atoms. However, this decrease is due to the fact that the average number of loaded atoms is between 5 and 6 atoms per attempt. This number is comparable to the size of the atomic arrays that we use. This effect combined with our low probability of success when moving atoms ($\sim$ 90 %/atom, depending on the moving distance) leads to the decrease in the loading rate. However, both the average number of loaded atoms and the moving probability can still be improved in the future and the results of other groups show that big improvements should be possible here.

4. **Limited cavity mode waist.** The mode waist of the cavity is $30\,\mu m$ and therefore only about 6 to 7 atoms fit into the cavity mode along the $x$-axis (orthogonal to the cavity). However, this limitation can be overcome by shuffling atoms in a coherent way in and out of the cavity mode. In this scenario, larger arrays along the $x$-axis would be prepared from which only six to seven atoms would simultaneously couple to the cavity and the remaining atoms outside of the cavity mode would serve as an atomic reservoir. The atoms in the reservoir could be shuffled coherently into the cavity mode when needed, as demonstrated in [118]. Shuffling atoms is advantageous compared to a larger cavity waist, as increasing the cavity waist leads to a reduction of the cooperativity $C$ (for a constant finesse). Therefore, when increasing the cavity waist, the finesse would have to be increased to achieve a comparable cooperativity which is typically complicated without reducing the photon escape efficiency $\kappa_{out}/\kappa$ (see equation (3.2)), which would lead to a decrease in the intrinsic photon production efficiency $P$.

5. **Temporal shape of the photon.** Right now, the photon is rather long and on the order of $1.5\,\mu s$. This leads to a limitation for the fidelity and for the efficiency as the photon acceptance window is shorter than the temporal width of the photon. The infidelity results from the finite width of the temporal shape of the emitted photon which translates into an uncertainty of the phase of the atomic state in the bases $XX$ and $YY$. At the same time, this phase uncertainty can also be seen as a reduction in the indistinguishability of the generated photons in the superposition bases due to the two different frequencies (separated by twice the Larmor frequency $\omega_L$) of the polarization states $|R\rangle = \int_{\mathcal{R}} f(t) \exp(i2\omega_L t)\hat{a}_R^\dagger(t) |0\rangle \, dt$ and $|L\rangle = \int_{\mathcal{R}} f(t)\hat{a}_L^\dagger(t) |0\rangle \, dt$, with the vacuum state $|0\rangle$, the temporal mode function of the photon $f(t)$ and the creation operator $\hat{a}^\dagger$. In $|R\rangle$, there is an additional phase factor, i.e. $\exp(i2\omega_L t)$. Only for $\omega_L = 0$, the photons are perfectly indistinguishable in all bases. However, this phase can be compensated for by using an EOM. An EOM imprints a phase shift on one specific polarization, where the magnitude and sign of the phase shift depend on the applied voltage. If the voltage is ramped up linearly ($\propto 2\omega_L t$), the phase difference between the two polarizations can be compensated. This solution has already been implemented in the
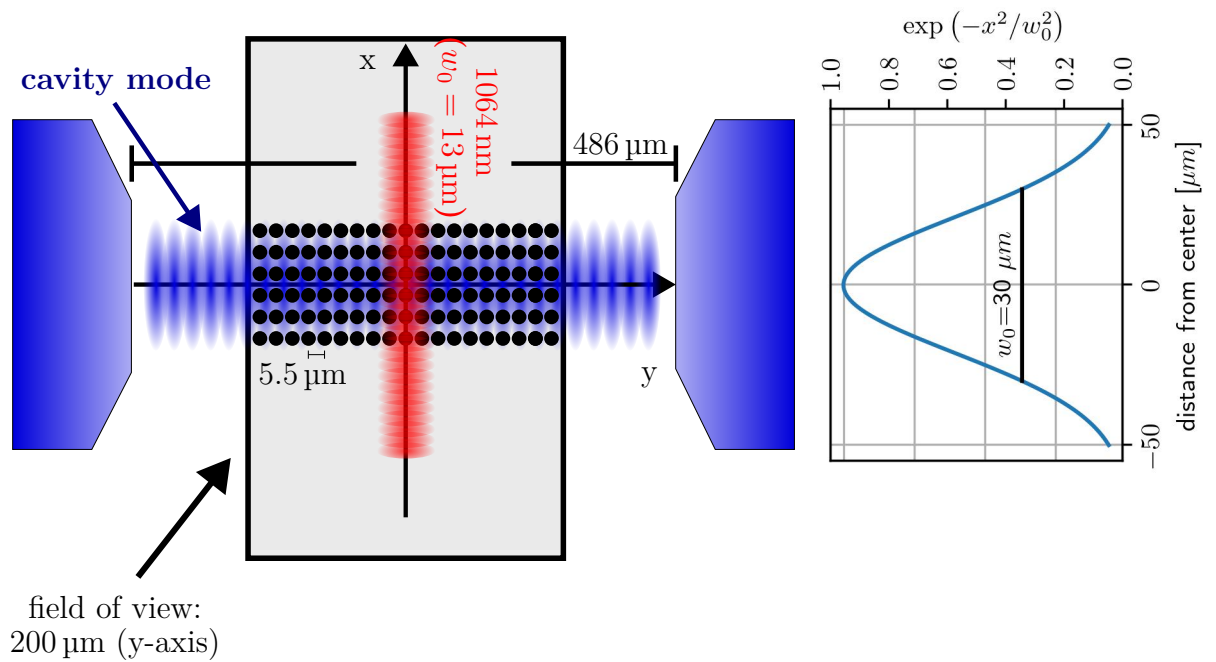
Figure 3.17: **Illustration of the theoretically largest possible area in which atoms can be positioned**. The number of atoms in the cavity is limited by the field of view (200 μm) of the objective along the $y$-axis and the waist ($w_0 = 30$ μm) of the cavity mode along the $x$-axis. This area provides space for approximately more than 200 atoms. However, in the current state of the setup the waist of the 1064 nm of 13 μm is limiting the number of atoms. This limit can be overcome by increasing the waist or installing multiple standing wave traps along the $x$-axis.

neighboring laboratory.

# Summary and Outlook

In this doctoral thesis, we have extended the existing QGATE experiment with a so-called single atom addressing and positioning system. This new system allows for the generation of optical tweezers and the precise positioning and addressing of individual atoms, which we use to generate of atomic arrays at the center of our cavity. In addition, we use our system to manipulate the state of individual atoms within the arrays using a single atom addressing beam. We use these two new experimental capabilities to implement a quantum network register that consists of up to six atoms and generate atom-photon entanglement with a multiplexing scheme. This results in the almost deterministic generation of atom-photon entanglement. The single atom addressing and positioning system and the implementation of the network register are described in detail in the individual chapters of this thesis:

In chapter 2, we first describe the setup of the new single-atom addressing and positioning system and how we use it to generate atomic arrays. With the new setup, we generate optical tweezers and implement a new protocol for loading atoms: We start by loading atoms stochastically into the static tweezers array and then rearrange the atoms into the desired array configuration with a second, movable optical tweezer. This loading protocol increases the loading efficiency by up to four orders of magnitude and allows us to arrange the atoms in one- and two-dimensional array configurations. At the moment, arrays of up to seven atoms can be prepared. The maximum number of atoms is mainly limited by the initial number of atoms that are loaded in the static tweezers array and the success probability of moving the atoms. Both these limitations can be improved in future experiments.

Afterwards, in chapter 3, we demonstrate the generation of atom-photon entanglement. To do this, we use a single-atom addressing beam to generate a photon in a vSTIRAP process. The polarization of the generated photon is entangled with the internal atomic state of the addressed atom. The photon and the atom are in the entangled Bell state $|\Psi^+\rangle$. For a single atom, the entanglement generation-to-detection efficiency is $33.2(3)\,\%$ and the fidelity of the entangled state with the Bell state $|\Psi^+\rangle$ is $86.6(5)\,\%$. We show that the fidelity is almost constant when arrays of up to to six atoms are loaded in an array orthogonal to the cavity axis. However, the entanglement generation efficiency drops for atoms which are located further away from the cavity center, since the cooperativity decreases for these atoms. This limits the number of atoms that can be positioned orthogonal to the cavity axis. Toovercome this limitation, it is necessary to demonstrate that we are able to prepare arrays of atoms in two-dimensional configurations. In these configurations, atoms

are positioned along the cavity axis as well and we show that both the fidelity and the efficiency behave as expected in the two-dimensional case, too. Afterwards, we demonstrate that the register can be used to increase the generation-to-detection efficiency of photon generation for six atoms to up to $88.6(1)\,\%$ (in fiber to $97.4(6)\,\%$) using a multiplexing protocol. In conclusion, we show that the fidelity is independent from the number of atoms and the specific array configuration and that the entanglement generation efficiency can be drastically improved by multiplexing. As we show that we are able to prepare two-dimensional arrays, we show the key step towards being able to position atoms in the entire cavity area. This capability allows the preparation of larger atomic arrays. The necessary steps to increase the size of the register are described in section 3.4.

The combination of atomic arrays with the ability to address individual atoms opens up many experimental possibilities in the future. One example is the generation of multiplexed, heralded atom-atom entanglement. For this purpose, crossed fiber cavities [119, 120], photon reflection schemes [85] or Bell state measurements [121–124] could be used. Another option is the implementation of a multi-atom CNOT gate. The multi-atom CNOT gate is an extension of the already implemented CNOT gate between two atoms [75]. The capability to address single atoms also allows to light shift the energy levels of specific atoms, which would allow to control the detuning of the light shifted atoms with respect to the cavity. Control over this detuning can be used to implement a CNOT gate between specific pairs of atoms in an atomic array [77]. Another option is to implement the photon generation scheme that I described in this thesis on the $D_1$ line. This way, the CNOT gate and the photon generation can be combined, which would allow for many more experimental protocols.

As demonstrated in this thesis, with only six atoms atom-photon entanglement generation efficiencies of $97\,\%$ in fiber can be achieved. However, this generation efficiency could be increased to even higher values as the cavity has room for approximately 200 atoms. Additional atoms could be trapped outside the cavity mode and serve as an atomic reservoir. By shuffling atoms in and out of the cavity mode, this number can even be further increased. If such large registers are successfully implementatied, the deterministic entanglement generation and distribution between different network nodes could be realized. As the essential experimental capabilities for quantum repeater nodes have already been demonstrated with our platform [88], multiplexed quantum repeater nodes are within reach. Such repeater nodes would reduce the requirements on the coherence time of the quantum memories at the nodes [125]. Besides the deterministic generation of atom-photon entanglement, having a large register at each node also allows for the possibility to generate multiple entangled atom pairs between different network nodes. This would enable entanglement distillation or entanglement purification. In entanglement distillation or purification, the unavoidable effects of decoherence in entanglement distribution are mitigated by distilling an entangled pair of higher entanglement fidelity from several pairs of entangled atoms [126–128]. The results presented in this thesis together with the examples given in this outlook suggest that the work presented in this thesis is laying the foundation for potentially large quantum network registers,

that combine the deterministic generation of atom-photon entanglement, all-to-all connectivity between register qubits, and the quantum memory capabilities that are required to implement multiplexed quantum repeater networks.

# Bibliography

[1] Yuri Manin. *Computable and Uncomputable*. Russian. Sovetskoye Radio, Moscow, 1980.

[2] Richard P. Feynman, Simulating physics with computers. *International Journal of Theoretical Physics* **21**, 467–488 (1982).

[3] David Deutsch and Richard Jozsa, Rapid Solution of Problems by Quantum Computation. *Proceedings of the Royal Society of London Series A* **439**, 553–558 (1992).

[4] P.W. Shor, Algorithms for quantum computation: discrete logarithms and factoring . *Proceedings 35th Annual Symposium on Foundations of Computer Science* (1994), pp. 124–134.

[5] Lov K. Grover, A fast quantum mechanical algorithm for database search . *Proceedings of the twenty-eighth annual ACM symposium on Theory of computing - STOC '96* (1996), pp. 212–219.

[6] Isaac L. Chuang, Neil Gershenfeld, and Mark Kubinec, Experimental Implementation of Fast Quantum Searching. *Phys. Rev. Lett.* **80**, 3408–3411 (1998).

[7] Stephan Gulde et al., Implementation of the Deutsch–Jozsa algorithm on an ion-trap quantum computer. *Nature* **421**, 48–50 (2003).

[8] C. Monroe et al., Demonstration of a Fundamental Quantum Logic Gate. *Phys. Rev. Lett.* **75**, 4714–4717 (1995).

[9] Ferdinand Schmidt-Kaler et al., Realization of the Cirac–Zoller controlled-NOT quantum gate. *Nature* **422**, 408–411 (2003).

[10] J. L. O'Brien et al., Demonstration of an all-optical quantum controlled-NOT gate. *Nature* **426**, 264–267 (2003).

[11] Adriano Barenco et al., Elementary gates for quantum computation. *Phys. Rev. A* **52**, 3457–3467 (1995).

[12] Michael A. Nielsen and Isaac L. Chuang. *Quantum Computation and Quantum Information*. Cambridge University Press, 2000.

[13] Charles H. Bennett et al., Purification of Noisy Entanglement and Faithful Teleportation via Noisy Channels. *Phys. Rev. Lett.* **76**, 722–725 (1996).

[14] P.W. Shor, Fault-tolerant quantum computation . *Proceedings of 37th Conference on Foundations of Computer Science* (1996), pp. 56–65.

[15]    Andrew Steane, Multiple-particle interference and quantum error correction. *Proceedings of the Royal Society of London. Series A: Mathematical, Physical and Engineering Sciences* **452**, 2551–2577 (1997).

[16]    W. Dür et al., Quantum repeaters based on entanglement purification. *Phys. Rev. A* **59**, 169–181 (1999).

[17]    Simon J. Devitt, William J. Munro, and Kae Nemoto, Quantum error correction for beginners. *Reports on Progress in Physics* **76**, 076001 (2013).

[18]    Joschka Roffe, Quantum Error Correction: An Introductory Guide. *Contemporary Physics* **60**, 226–245 (2019).

[19]    Austin G. Fowler et al., Surface codes: Towards practical large-scale quantum computation. *Phys. Rev. A* **86**, 032324 (2012).

[20]    Earl T. Campbell, Barbara M. Terhal, and Christophe Vuillot, Roads towards fault-tolerant universal quantum computation. *Nature* **549**, 172–179 (2017).

[21]    Laird Egan et al., Fault-tolerant control of an error-corrected qubit. *Nature* **598**, 281–286 (2021).

[22]    C. Ryan-Anderson et al., Realization of Real-Time Fault-Tolerant Quantum Error Correction. *Phys. Rev. X* **11**, 041058 (2021).

[23]    M. H. Abobeih et al., Fault-tolerant operation of a logical qubit in a diamond quantum processor. *Nature* **606**, 884–889 (2022).

[24]    Sebastian Krinner et al., Realizing repeated quantum error correction in a distance-three surface code. *Nature* **605**, 669–674 (2022).

[25]    Youwei Zhao et al., Realization of an Error-Correcting Surface Code with Superconducting Qubits. *Phys. Rev. Lett.* **129**, 030501 (2022).

[26]    Neereja Sundaresan et al., Demonstrating multi-round subsystem quantum error correction using matching and maximum likelihood decoders. *Nature Communications* **14**, 2852 (2023).

[27]    Rajeev Acharya et al., Suppressing quantum errors by scaling a surface code logical qubit. *Nature* **614**, 676–681 (2023).

[28]    Dolev Bluvstein et al., Logical quantum processor based on reconfigurable atom arrays. *Nature* **626**, 58–65 (2024).

[29]    Harry Buhrman and Hein Röhrig, Distributed Quantum Computing. In: *Mathematical Foundations of Computer Science 2003.* Gerhard Goos et al., eds., vol. 2747, Springer Berlin Heidelberg, (2003). pp. 1–20.

[30]    Liang Jiang et al., Distributed quantum computation based on small quantum registers. *Phys. Rev. A* **76**, 062323 (2007).

[31]    C. Monroe et al., Large-scale modular quantum-computer architecture with atomic memory and photonic interconnects. *Phys. Rev. A* **89**, 022317 (2014).

[32]    H. J. Kimble, The quantum internet. *Nature* **453**, 1023–1030 (2008).

[33]    Stephanie Wehner, David Elkouss, and Ronald Hanson, Quantum internet: A vision for the road ahead. *Science* **362**, eaam9288 (2018).

[34] Peter Kómár et al., A quantum network of clocks. *Nature Physics* **10**, 582–587 (2014).

[35] B. C. Nichol et al., An elementary quantum network of entangled optical atomic clocks. *Nature* **609**, 689–694 (2022).

[36] S. Pirandola et al., Advances in Quantum Cryptography. *Advances in Optics and Photonics* **12**, 1012 (2020).

[37] Daniel Gottesman, Thomas Jennewein, and Sarah Croke, Longer-Baseline Telescopes Using Quantum Repeaters. *Phys. Rev. Lett.* **109**, 070503 (2012).

[38] Stephan Ritter et al., An elementary quantum network of single atoms in optical cavities. *Nature* **484**, 195–200 (2012).

[39] M. Pompili et al., Realization of a multinode quantum network of remote solid-state qubits. *Science* **372**, 259–264 (2021).

[40] V. Krutyanskiy et al., Entanglement of Trapped-Ion Qubits Separated by 230 Meters. *Phys. Rev. Lett.* **130**, 050803 (2023).

[41] C. M. Knaut et al., Entanglement of nanophotonic quantum memory nodes in a telecom network. *Nature* **629**, 573–578 (2024).

[42] Jian-Long Liu et al., Creation of memory–memory entanglement in a metropolitan quantum network. *Nature* **629**, 579–585 (2024).

[43] Arian J. Stolk et al., Metropolitan-scale heralded entanglement of solid-state qubits. arXiv:2404.03723 [quant-ph] (2024).

[44] P. Maunz et al., Heralded Quantum Gate between Remote Quantum Memories. *Phys. Rev. Lett.* **102**, 250502 (2009).

[45] Severin Daiss et al., A quantum-logic gate between distant quantum-network modules. *Science* **371**, 614–617 (2021).

[46] V. Krutyanskiy et al., Multimode ion-photon entanglement over 101 kilometers of optical fiber. arXiv:2308.08891 [quant-ph] (2023).

[47] Yiru Zhou et al., Long-Lived Quantum Memory Enabling Atom-Photon Entanglement over 101 km of Telecom Fiber. *PRX Quantum* **5**, 020307 (2024).

[48] B. Hensen et al., Loophole-free Bell inequality violation using electron spins separated by 1.3 kilometres. *Nature* **526**, 682–686 (2015).

[49] Tim van Leent et al., Entangling single atoms over 33 km telecom fibre. *Nature* **607**, 69–73 (2022).

[50] Arian J. Stolk et al., Metropolitan-scale heralded entanglement of solid-state qubits. arXiv:2404.03723 [quant-ph] (2024).

[51] A. Stute et al., Tunable ion–photon entanglement in an optical cavity. *Nature* **485**, 482–485 (2012).

[52] Pascal Kobel, Moritz Breyer, and Michael Köhl, Deterministic spin-photon entanglement from a trapped ion in a fiber Fabry–Perot cavity. *npj Quantum Information* **7**, 1–7 (2021).

[53]  Philip Thomas et al., Efficient generation of entangled multiphoton graph states from a single atom. *Nature* **608**, 677–681 (2022).

[54]  Chao-Wei Yang et al., Deterministic measurement of a Rydberg superatom qubit via cavity-enhanced single-photon emission. *Optica* **9**, 853–858 (2022).

[55]  Adrien Dousse et al., Ultrabright source of entangled photon pairs. *Nature* **466**, 217–220 (2010).

[56]  I. Schwartz et al., Deterministic generation of a cluster state of entangled photons. *Science* **354**, 434–437 (2016).

[57]  Andrei Ruskuc et al., Scalable Multipartite Entanglement of Remote Rare-earth Ion Qubits. arXiv:2402.16224 [quant-ph] (2024).

[58]  C. T. Nguyen et al., Quantum Network Nodes Based on Diamond Qubits with an Efficient Nanophotonic Interface. *Phys. Rev. Lett.* **123**, 183602 (2019).

[59]  A. Ashkin, Acceleration and Trapping of Particles by Radiation Pressure. *Phys. Rev. Lett.* **24**, 156–159 (1970).

[60]  A. Ashkin et al., Observation of a single-beam gradient force optical trap for dielectric particles. *Optics Letters* **11**, 288–290 (1986).

[61]  A. Ashkin and J. M. Dziedzic, Optical Trapping and Manipulation of Viruses and Bacteria. *Science* **235**, 1517–1520 (1987).

[62]  Nicolas Schlosser et al., Sub-poissonian loading of single atoms in a microscopic dipole trap - Nature. *Nature* **411**, 1024–1027 (2001).

[63]  Hyosub Kim et al., In situ single-atom array synthesis using dynamic holographic optical tweezers. *Nature Communications* **7**, 13317 (2016).

[64]  Daniel Barredo et al., An atom-by-atom assembler of defect-free arbitrary two-dimensional atomic arrays. *Science* **354**, 1021–1023 (2016).

[65]  Manuel Endres et al., Atom-by-atom assembly of defect-free one-dimensional cold atom arrays. *Science* **354**, 1024–1027 (2016).

[66]  Pascal Scholl et al., Quantum simulation of 2D antiferromagnets with hundreds of Rydberg atoms. *Nature* **595**, 233–238 (2021).

[67]  Sepehr Ebadi et al., Quantum phases of matter on a 256-atom programmable quantum simulator. *Nature* **595**, 227–232 (2021).

[68]  Hannah J. Manetsch et al., A tweezer array with 6100 highly coherent atomic qubits. arXiv:2403.12021 [quant-ph] (2024).

[69]  Tamara Dordević et al., Entanglement transport and a nanophotonic interface for atoms in optical tweezers. *Science* **373**, 1511–1514 (2021).

[70]  Yanxin Liu et al., Realization of Strong Coupling between Deterministic Single-Atom Arrays and a High-Finesse Miniature Optical Cavity. *Phys. Rev. Lett.* **130**, 173601 (2023).

[71]  Zhenjie Yan et al., Superradiant and Subradiant Cavity Scattering by Atom Arrays. *Phys. Rev. Lett.* **131**, 253603 (2023).

[72]  David P. DiVincenzo, The Physical Implementation of Quantum Computation. *Fortschritte der Physik* **48**, 771–783 (2000).

[73]  Nicolas Sangouard et al., Quantum repeaters based on atomic ensembles and linear optics. *Rev. Mod. Phys.* **83**, 33–80 (2011).

[74]  Severin Daiß, Single-Photon Distillation and Nonlocal Quantum-Logic Gate. PhD Thesis. (2022).

[75]  Stephan T. Welte, Photon-Mediated Quantum Information Processing with Neutral Atoms in an Optical Cavity. PhD Thesis. (2019).

[76]  Bastian Hacker, Two-Photon Gate and Creation of Optical Cat States using One Atom in a Cavity. PhD Thesis. (2019).

[77]  Andreas Reiserer. *A Controlled Phase Gate Between a Single Atom and an Optical Photon.* Springer Theses. Cham: Springer International Publishing, 2016.

[78]  R. J. Thompson, G. Rempe, and H. J. Kimble, Observation of normal-mode splitting for an atom in an optical cavity. *Phys. Rev. Lett.* **68**, 1132–1135 (1992).

[79]  Stephan Welte et al., Supplementary Material for "Cavity Carving of Atomic Bell States". *Phys. Rev. Lett.* **118**, 210503 (2017).

[80]  Bernhard Weber, Distribution of quantum information between an atom and two photons. PhD thesis. (2008).

[81]  Markus Hijlkema, Single photons from a single atom trapped in a high-finesse optical cavity. PhD thesis. (2007).

[82]  Daniel A. Steck, Rubidium 87 D Line Data. (2001).

[83]  Andreas Neuzner et al., Breakdown of atomic hyperfine coupling in a deep optical-dipole trap. *Phys. Rev. A* **92**, 053842 (2015).

[84]  Andreas Reiserer, Stephan Ritter, and Gerhard Rempe, Nondestructive Detection of an Optical Photon. *Science* **342**, 1349–1351 (2013).

[85]  Andreas Reiserer et al., A quantum gate between a flying optical photon and a single trapped atom. *Nature* **508**, 237–240 (2014).

[86]  Bastian Hacker et al., A photon–photon quantum gate based on a single atom in an optical resonator. *Nature* **536**, 193–196 (2016).

[87]  Stefan Langenfeld et al., A network-ready random-access qubits memory. *npj Quantum Information* **6**, 86 (2020).

[88]  S. Langenfeld et al., Quantum Repeater Node Demonstrating Unconditionally Secure Key Distribution. *Phys. Rev. Lett.* **126**, 230506 (2021).

[89]  Franz von Silva-Tarouca, Selective Control of Individual Atomic Qubits Coupled to an Optical Resonator. MA thesis. (2024).

[90]  M. Uphoff, State manipulation of single atoms in an optical cavity. Diploma Thesis. (2010).

[91]   E. Brion, L. H. Pedersen, and K. Mølmer, Adiabatic elimination in a lambda system. *Journal of Physics A: Mathematical and Theoretical* **40**, 1033 (2007).

[92]   Tatjana Wilk et al., Single-Atom Single-Photon Quantum Interface. *Science* **317**, 488–490 (2007).

[93]   O. Morin et al., Deterministic Shaping and Reshaping of Single-Photon Temporal Wave Functions. *Phys. Rev. Lett.* **123**, 133602 (2019).

[94]   J. Bochmann et al., Lossless State Detection of Single Neutral Atoms. *Phys. Rev. Lett.* **104**, 203601 (2010).

[95]   Andreas Reiserer and Gerhard Rempe, Cavity-based quantum networks with single atoms and optical photons. *Reviews of Modern Physics* **87**, 1379–1418 (2015).

[96]   P. Debye and F. W. Sears, On the Scattering of Light by Supersonic Waves. *Proceedings of the National Academy of Sciences* **18**, 409–414 (1932).

[97]   André Kochanke, A High Resolution Optical System for Imaging and Addressing of Single Atoms. MA thesis. (2012).

[98]   M. Schroeder, Synthesis of low-peak-factor signals and binary sequences with low autocorrelation (Corresp.) *IEEE Transactions on Information Theory* **16**, 85–89 (1970).

[99]   Y. R. P. Sortais et al., Diffraction-limited optics for single-atom manipulation. *Phys. Rev. A* **75**, 013406 (2007).

[100]   D.F. Walls and Gerard J. Milburn, eds. *Quantum Optics*. Berlin, Heidelberg: Springer, 2008.

[101]   Ana Predojević and Morgan W. Mitchell, eds. *Engineering the Atom-Photon Interaction: Controlling Fundamental Processes with Photons, Atoms and Solids*. Nano-Optics and Nanophotonics. Cham: Springer International Publishing, 2015.

[102]   J. D. Thompson et al., Coherence and Raman Sideband Cooling of a Single Atom in an Optical Tweezer. *Phys. Rev. Lett.* **110**, 133001 (2013).

[103]   Wenjamin Rosenfeld, Experiments with an Entangled System of a Single Atom and a Single Photon. PhD thesis. (2008).

[104]   Matthew A. Norcia et al., Seconds-scale coherence on an optical clock transition in a tweezer array. *Science* **366**, 93–97 (2019).

[105]   Ivaylo S. Madjarov et al., An Atomic-Array Optical Clock with Single-Atom Readout. *Phys. Rev. X* **9**, 041052 (2019).

[106]   Simon J. Evered et al., High-fidelity parallel entangling gates on a neutral-atom quantum computer. *Nature* **622**, 268–272 (2023).

[107]   Stefan Nußmann, Kühlen und Positionieren eines Atoms in einem optischen Resonator. PhD Thesis. (2006).

[108]   Lukas Hartung et al., A quantum-network register assembled with optical tweezers in an optical cavity. *Science* **385**, 179–183 (2024).

[109]    Stefan Langenfeld, Quantum Communication with a Two-Atoms Network Node. PhD thesis. (2022).

[110]    Luigi Giannelli et al., Optimal storage of a single photon by a single intra-cavity atom. *New Journal of Physics* **20**, 105009 (2018).

[111]    E. M. Purcell, H. C. Torrey, and R. V. Pound, Resonance Absorption by Nuclear Magnetic Moments in a Solid. *Phys. Rev.* **69**, 37–38 (1946).

[112]    M. Körber et al., Decoherence-protected memory for a single-photon qubit. *Nature Photonics* **12**, 18–21 (2018).

[113]    Joseph B. Altepeter, Daniel F.V. James, and Paul G. Kwiat, 4 Qubit Quantum State Tomography. In: *Quantum State Estimation*. Matteo Paris and Jaroslav Řeháček, eds., Springer, (2004). pp. 113–145.

[114]    A. M. Kaufman et al., Two-particle quantum interference in tunnel-coupled optical tweezers. *Science* **345**, 306–309 (2014).

[115]    V. Krutyanskiy et al., Multimode Ion-Photon Entanglement over 101 Kilometers. *PRX Quantum* **5**, 020308 (2024).

[116]    Philip Thomas,   personal communication (2024).

[117]    Andreas Reiserer et al., Ground-State Cooling of a Single Atom at the Center of an Optical Cavity. *Phys. Rev. Lett.* **110**, 223003 (2013).

[118]    Dolev Bluvstein et al., A quantum processor based on coherent transport of entangled atom arrays. *Nature* **604**, 451–456 (2022).

[119]    Dominik Niemietz, Nondestructive detection of photonic qubits with single atoms in crossed fiber cavities. PhD thesis. (2021).

[120]    Manuel K. L. Brekenfeld, Ein photonischer Quantenspeicher mit einem Atom in gekreuzten optischen Faserresonatoren. PhD thesis. (2023).

[121]    D. L. Moehring et al., Entanglement of single-atom quantum bits at a distance. *Nature* **449**, 68–71 (2007).

[122]    Julian Hofmann et al., Heralded Entanglement Between Widely Separated Atoms. *Science* **337**, 72–75 (2012).

[123]    H. Bernien et al., Heralded entanglement between solid-state qubits separated by three metres. *Nature* **497**, 86–90 (2013).

[124]    Aymeric Delteil et al., Generation of heralded entanglement between distant hole spins. *Nature Physics* **12**, 218–223 (2016).

[125]    O. A. Collins et al., Multiplexed Memory-Insensitive Quantum Repeaters. *Phys. Rev. Lett.* **98**, 060502 (2007).

[126]    Charles H. Bennett et al., Purification of Noisy Entanglement and Faithful Teleportation via Noisy Channels. *Phys. Rev. Lett.* **76**, 722–725 (1996).

[127]    David Deutsch et al., Quantum Privacy Amplification and the Security of Quantum Cryptography over Noisy Channels. *Phys. Rev. Lett.* **77**, 2818–2821 (1996).

[128]    N. Kalb et al., Entanglement distillation between solid-state quantum network nodes. *Science* **356**, 928–932 (2017).

# Danksagung

Zuletzt möchte ich mich bei einigen Menschen bedanken:

Zuerst möchte ich mich bei meinem Doktorvater Gerhard Rempe für die Möglichkeit bedanken, am Qgate arbeiten zu dürfen. Du hast uns als Team während all der Jahre großes Vertrauen entegegengebracht und uns viel Freiheit bei der Auswahl der Experimente, der Planung und der Durchführung gegeben. Wann immer nötig, hast du uns mit deinem Physikwissen weitergeholfen und die richtigen Fragen gestellt und die richtigen Vorschläge eingebracht. Dafür möchte ich dir danken.

Many thanks to our PostDoc Emanuele. We worked together in the QGate team for more than four years. We started together as Qgate newbies and discovered the experiment together, however, discovering in that case means that you discovered new things and explained them afterwards to me. Throughout this lengthy and sometimes tiring project, your dedication, endurance and perseverance have been truly remarkable. Your big scientific knowledge and your huge contribution to my thesis don't go unnoticed. Here's a mega thank you for all the support! I wish you all the best for your future scientific endeavors and I am sure you will find the scientific position that you deserve (that's meant in a positive way ;) )!

Ein großes Dankeschön an Matthias, meinen QGate Nachfolger. Du warst die mir manchmal fehlende ruhige und präzise Komponente im Labor, wenn du nicht gerade Freude daran hattest, Mayas LabSnacks zu verstecken. Ohne deinen Einsatz, deine Programmierarbeit und deine Unterstützung würde ich jetzt noch im Labor feststecken. Vielen Dank dafür.

Außerdem möchten ich mich bei meinen Vorgängern Bastian, Stephan und Severin bedanken. Ihr habt mich in meiner Anfangszeit (oder auch ein bisschen länger) am MPQ begleitet und habt mich in die Wirren des Lebens am MPQ und im Labor eingeführt und gleichzeitig die Spaßkomponente nicht vernachlässigt. Danke für eure Unterstützung, die Einführung ins Experiment und die diversen Freizeitunternehmungen. Danke dafür!

Ein großes Dankeschön an Maya, unsere Labornachbarin, die sich selbst zum LaborDJ ernannt hat. Obwohl sie uns mit ihren Playlists teilweise nur mäßig beeindruckte, brachte sie immer den nötigen Schwung in unser Laborleben und hat uns aus dem ein oder anderen Stimmungstief herausgeholt, wenn unser Experiment mal wieder nicht so wollte wie wir.

Dann möchte ich mich bei all den QIPlern und Molekülen, ehemaligen und aktuellen, bedanken: Hendrik, Stephan Dürr, Thomas Stolz, Steffen, Martin I., Martin Z., Max, Manuel, Thomas G., Florian, Boom, Dominik, Manuel, Joe, Gianvito, Tobias, Pau, Chris, Bo, Nico, Matthias K., Stefan L., Olivier, Leonardo und zuletzt Thomas Philip. Wann immer man eine Frage, Gesprächsbedarf oder

Probleme im Elektronikraum hatte, gab es immer einen, der einem weiterhelfen konnte.

Zum Glück mussten wir uns in unserer Gruppe dank unserer Techniker – Johannes, Tom, Florian, Tobias und Markus – nicht allein um die vielen mechanischen und elektronischen Probleme kümmern. Eure Unterstützung und Hilfe bekommt nicht immer die Anerkennung, die sie verdient, denn ohne euch würde oft gar nichts funktionieren. Vielen Dank für die stets kompetente, aber mindestens genauso sympathische Unterstützung während meiner Zeit hier.

Und natürlich möchte ich mich bei meiner Familie und vor allem bei meinen Eltern bedanken. Ihr habt mich bei all meinen Unternehmungen immer unterstützt und mir vieles ermöglicht. Das ist nicht selbstverständlich und dafür bin ich euch dankbar!